MAGNETIC SUSCEPTIBILITY APPROACH FOR QUANTITATIVE CEREBRAL OXYGEN METABOLISM MAPPING

A Dissertation

Presented to the Faculty of the Graduate School

of Cornell University

in Partial Fulfillment of the Requirements for the Degree of

Doctor of Philosophy

by

Jingwei Zhang

May 2017

MAGNETIC SUSCEPTIBILITY APPROACH FOR QUANTITATIVE CEREBRAL OXYGEN METABOLISM MAPPING

Jingwei Zhang, Ph.D.

Cornell University 2017

Magnetic resonance imaging (MRI) is a noninvasive technique that allows imaging three dimensional volume through the body, providing superior soft tissue contrast compared to CT without ionizing radiation. MRI can be used to detect field inhomogeneity induced by blood iron molecules such as deoxyhemoglobin, methemoglobin, and hemosiderin, providing opportunities to identify and quantify these molecules and oxygen consumption, especially in brain. This dissertation reports: 1) a clinical study on intracranial hematoma evolution using quantitative susceptibility mapping (QSM); 2) a new magnetic susceptibility based signal model and technique to quantitatively map cerebral metabolic rate of oxygen ($CMRO_2$) and oxygen extraction fraction (OEF) using QSM; 3) a new algorithm to improve SNR of QSM-based $CMRO_2$ using prior knowledge; 4) a new algorithm called minimal local variance (MLV) to improve clinical practicality of QSM-based $CMRO_2$ by removing the requirement of blood flow challenge. The potential impacts, limitations and future directions of each studies are also discussed.

BIOGRAPHICAL SKETCH

Jingwei Zhang was born in Shenzhen City, Guangdong Province, People's Republic of China, in 1988. He received the Bachelor of Engineering degree in Biomedical Engineering from the City College of New York, the City University of New York in 2011. He joined the graduate program in Biomedical Engineering at Cornell University in the Fall of 2011, and received the Master of Science degree in Biomedical Engineering in 2014.

Dedicated To My Family and Friends

For Their Support, Respect, Love, and Encouragement

ACKNOWLEDGEMENTS

First, I would like to thank the Department of Biomedical Engineering, Cornell University, and the Department of Radiology, Weill Cornell Medical College for giving me the opportunity and other necessary means to join the graduate program and work on my PhD thesis.

I am especially thankful to my advisor, Prof. Yi Wang, for his guidance and support in my PhD thesis and career development. His expertise in the field of MRI has greatly influenced my work. His enthusiasm towards MRI and persistence in finding the truth have enlightened me on multiple occasions. He also helped me establish collaborations with clinical researchers, especially with my minor science advisor Dr. Ajay Gupta, which are crucial to my PhD thesis.

I would also like to thank my two minor advisors, Prof. Peter Charles Doerschuk from Cornell University, and Dr. Ajay Gupta from Weill Cornell Medical College for their support. Prof. Doerschuk provided valuable advice on course work and on my PhD thesis. Dr. Gupta provided clinical prospective for my work and was a co-author in manuscripts from my PhD thesis.

I am very grateful to Prof. Thanh D. Nguyen and Prof. Pascal Spincemaille from Weill Cornell Medical College for their constant advice during brain storming and discussion sections. Both were co-authors in manuscripts from my PhD thesis.

I am also grateful, in no particular order, to my colleagues and friends who have been friendly and provided insights and opinions in many enlightening discussions: Martin R. Prince (M.D., Ph.D), Alexey Dimov, Bo Xu, Carlo Salustri, Dong Zhou, Kofi Deh, Mitch A. Cooper, Sarah Eskreis-Winkler, Tian Liu, Yan Wen, Zhe Liu, Junghun Cho, Xi Yang, and many others.

Finally I would like to thank my parents and sister: Bingguang Zhang, Xiuhua Ye, and Jiaxin Zhang, who have given me tremendous supports for and beyond my PhD study.

Table of Contents

List of Tables

List of Figures

Chapter 1

Introduction

1.1 SUMMARY OF CONTRIBUTIONS

Magnetic resonance imaging (MRI) is a noninvasive technique that allows imaging three dimensional volume through the body. Unlike computed tomography (CT) and x-ray imaging, MRI provides superior soft tissue contrast without ionizing radiation by using physical principles similar to that of nuclear magnetic resonance (NMR) spectroscopy with the addition of magnetic field gradients. MRI physics will be discussed in greater details in chapter 2.

In this thesis, quantitative susceptibility mapping (QSM) has been used to study intracerebral hemorrhage (ICH) and brain oxygenation. Briefly, QSM generates a three-dimensional map by solving magnetic field to susceptibility source inverse problem, where voxel intensity is linearly proportional to tissue magnetic susceptibility. QSM physical principle will be discussed in greater details in the chapter 2.

Chapter 2 also presents the underlining principles of arterial spin labeling (ASL), another MRI imaging technique used in conjunction with QSM to study brain oxygenation in this thesis. The definition and physiological meanings of cerebral metabolic rate of oxygen ($CMRO_2$) and oxygen extraction fraction (OEF) are also discussed.

Chapter 3 presents a clinical study which investigate the magnetic susceptibility of hematomas at various stages using QSM. ICH is a life threatening medical condition, which require accurate staging and monitoring of the developments of hematomas. The blood degradation process in ICH has been characterized qualitatively but not quantitatively on

MRI using standard T1 weighted (T1w), T2 weighted (T2w), and T2* weighted gradient echo (T2*w) imaging (1-3). The study demonstrates the potential of QSM to provide more accurate hematoma staging and to quantify blood degradation products.

Stroke is yet another life threatening medical conditions, which require prompt and accurate diagnosis and treatments. The quantitative mapping of cerebral metabolic rate of oxygen ($CMRO_2$) and oxygen extraction fraction (OEF) has long been sought after in both research and clinical settings as important indicators for neural viability and activity in stroke (4-6). As oxygen is released to brain tissue, the weakly diamagnetic oxyhemoglobin (oHb) turns into to the strongly paramagnetic deoxyhemoglobin (dHb) and induces magnetic field inhomogeneity detectable by MRI (7,8). Several MRI techniques have been proposed to map dH: 1) Quantitative imaging of extraction of oxygen and tissue consumption (QUIXOTIC), which uses a velocity-selective spin labeling to selectively map venous blood T2 and oxygenation (9). 2) Calibrated fMRI, which models the magnitude $R2^*$ decay of the blood oxygen level dependent (BOLD) signal as a complex function of dH concentration ([dH]), typically estimating [dH] from signal measurements at two vascular challenges such as hyperoxia and hypercapnia to obtain $CMRO_2$ (10-12). 3) quantitative BOLD, which uses a specific venous geometry of randomly oriented tubes to model [dH] dependence of signal generated in asymmetric spin echo (13,14) or 3D multi-echo gradient echo data (15). Some of the limitation of these approaches includes: 1) sensitive to scanning parameters; 2) limited clinical practicality with multiple blood flow challenges.

In chapter 4, a new signal model based on magnetic susceptibility of blood and non-blood tissue is proposed to overcome some of the limitations mentioned above. An imaging technique and an algorithm based on the new signal model were invented to quantitatively map CMRO2 and OEF on 13 healthy subjects (n=13, 13 males, mean age 35 ± 9.5 years) using 3T MRI scanners (HDxt, GE Healthcare, Waukesha, WI, USA), and an 8-channel receive head coil. The study demonstrates that QSM can be used in conjunction with cerebral perfusion measurements before and after a vasoconstricting caffeine challenge to map CMRO2 and OEF.

In chapter 5, a new algorithm is proposed to denoise QSM based CMRO2 and OEF maps by incorporating prior knowledge (Bayesian approach) during image reconstruction. The prior knowledge include a right-handed preconditioner, a CMRO2 global constraint derived from straight sinus, and a physiological lower and upper bounds of 0 to 100 % on OEF maps. Caffeine administration is also replaced by hyperventilation as the vaso-restrictive challenge in order to reduce the protocol time. The study shows hyperventilation is a feasible, reproducible and efficient vasoconstrictive challenge for QSM based quantitative CMRO2 mapping in healthy subjects with good reproducibility and offers 4-fold protocol time reduction compared to using caffeine as a challenge. Constrained optimization within physical range of OEF provides substantial reduction of noise errors in CMRO2 and OEF maps. The applicability of this protocol for a general patient population remains to be investigated.

In chapter 6, a new algorithm named minimal local variance (MLV) is proposed to remove the requirement of vaso challenges in the QSM-based CMRO2 technique to further improve its clinical practicality. The lack of susceptibility and perfusion measurements of the challenged brain state leads to ill-posedness of the optimization problem, more specifically two unknowns with one equation per voxel. MLV overcomes the ill-posedness by assuming constant CMRO2 and non-blood tissue susceptibility within each tissue type (gray and white matter) across small regions of the brain. This assumption groups multiple equations to invert two unknowns within each tissue type and small regions. The study demonstrated the feasibility of a noninvasive CMRO2 mapping without vascular challenge based on QSM and CBF using MLV. In vivo imaging in heathy subjects demonstrates that the CMRO2 and OEF maps obtained with the proposed MLV method agree well with those obtained using a blood flow challenge based method.

Chapter 7 presents the future work for ICH study using QSM and QSM based CMRO2 technique.

1.2 ABSTRACT AND PUBLICATIONS

Following is a list of publications and abstracts resulted from this thesis.

Journal Publications

1) Zhang J, Liu T, Gupta A, Spincemaille P, Nguyen TD, Wang Y. Quantitative mapping of cerebral metabolic rate of oxygen (CMRO2) using quantitative susceptibility mapping (QSM). Magnetic resonance in medicine 2015;74(4):945-952.

2) Zhang J, Zhou D, Nguyen TD, Spincemaille P, Gupta A, Wang Y. Cerebral metabolic rate of oxygen (CMRO) mapping with hyperventilation challenge using quantitative susceptibility mapping (QSM). Magnetic resonance in medicine : official journal of the Society of Magnetic Resonance in Medicine / Society of Magnetic Resonance in Medicine 2016;10.1002/mrm.26253.

3) Chang S, Zhang J, Liu T, Tsiouris AJ, Shou J, Nguyen T, Leifer D, Wang Y, Kovanlikaya I. Quantitative Susceptibility Mapping of Intracerebral Hemorrhages at Various Stages. Journal of magnetic resonance imaging : JMRI 2016;44(2):420-425.

4) Zhou D, Cho J, Zhang J, Spincemaille P, Wang Y. Susceptibility underestimation in a high-susceptibility phantom: Dependence on imaging resolution, magnitude

contrast, and other parameters. Magnetic resonance in medicine : official journal of the Society of Magnetic Resonance in Medicine / Society of Magnetic Resonance in Medicine 2016. DOI: 10.1002/mrm.26475

5) Eskreis-Winkler S, Zhang Y, Zhang J, Liu Z, Dimov A, Gupta A, Wang Y. The clinical utility of QSM: disease diagnosis, medical management, and surgical planning. NMR in biomedicine 2016. doi: 10.1002/nbm.3668.

6) Zhang J, Cho J, Zhou D, Nguyen T, Spincemaille P, Gupta A, Wang Y, Quantitative Susceptibility Mapping (QSM)-Based Cerebral Metabolic Rate of Oxygen (CMRO2) Mapping with Minimum Local Variance (MLV), MRM 2017. DOI: 10.1002/mrm.26657

Abstracts

1) Jingwei Zhang, Mengchao Pei, Tian Liu1, Ajay Gupta1, Cynthia Wisnieff1, Pina C. Sanelli, Pascal Spincemaille, Yi Wang, Abstract 3334, Quantitative Susceptibility Mapping (QSM) for High Resolution Quantitative Cerebral Metabolic Rate of Oxygen (CMRO2), ISMRM 2013

2) Jingwei Zhang, Tian Liu, Ajay Gupta, Pina C. Sanelli, Cynthia Wisnieff, Pascal Spincemaille, and Yi Wang, Abstract 20, Traditional Poster, Cerebral Metabolic Rate of Oxygen (CMRO2) Quantitative Mapping Using Quantitative Susceptibility

Mapping (QSM), 2nd International Workshop on MRI Phase Contrast & Quantitative Susceptibility Mapping (QSM) 2013

3) Jingwei Zhang, Tian Liu, Ajay Gupta, Pina C. Sanelli, Cynthia Wisnieff, Pascal Spincemaille, and Yi Wang, Abstract, traditional poster, Cerebral Metabolic Rate of Oxygen ($CMRO_2$) Mapping Using Quantitative Susceptibility Mapping (QSM), 25th International Workshop on Magnetic Resonance Angiography, 2013

4) Jingwei Zhang, Thanh D. Nguyen, Tian Liu, Shixin Chang, Ilhami Kovanlikaya, and Yi Wang, Abstract 4759, electronic poster, Hematoma Evolution Measured by Quantitative MRI, ISMRM2014

5) Ilhami Kovanlikaya, Apostolos John Tsiouris, Tian Liu, Jingwei Zhang, Yi Wang, and Shixin Chang, Abstract 3273, electronic poster, Quantitative susceptibility mapping of intracranial hemorrhages at different stages, ISMRM 2014

6) Jingwei Zhang, Thanh D. Nguyen, Xavier J. Candela, Kory P. Witmer, Keefe B. Manning, and Yi Wang, Abstract 0112, oral presentation, Quantitative Relaxation Time and Susceptibility Mapping of Thrombus, ISMRM 2014

7) Jingwei Zhang, Tian Liu, Ajay Gupta, Pascal Spincemaille, Thanh Nguyen, Yi Wang Quantitative Mapping of Cerebral Metabolic Rate of Oxygen (CMRO2):

Comparison between Quantitative Susceptibility Mapping (QSM) and R2* Methods, Abstract, Traditional Poster, QSM Workshop 2014, Duke University

8) Jingwei Zhang, Cynthia Wisnieff, Becky Schur, Ronglu Zheng, David Pitt, Yi Wang Measurement of Brain Iron and Calcium using MR QSM and CT: validation using Inductively Coupled Plasma Optical Emission Spectrometry (ICP-OES), Abstract, Traditional Poster, QSM Workshop 2014, Duke University

9) Dong Zhou, Tian Liu, Jingwei Zhang, and Yi Wang Accuracy of the QSM reconstruction: dependence on imaging resolution and B0 strength, Abstract, Traditional Poster, QSM Workshop 2014, Duke University

10) Jingwei Zhang, Tian Liu, Ajay Gupta, Pascal Spincemaille, Thanh Nguyen, Yi Wang, Oral Presentation, Quantitative Mapping of Cerebral Metabolic Rate of Oxygen (CMRO2) Using Quantitative Susceptibility Mapping (QSM) and Quantitative Cerebral Perfusion, RSNA 2014, RSNA Paper No: SSQ14-01, RSNA ID: 14011086,

11) Alexey Dimov, Thanh Nguyen, Zhe Liu, Kofi Deh, Jingwei Zhang, Martin Prince, Yi Wang, Abstract 1703, Traditional Poster, Estimation of Blood Oxygenation Using Quantitative Susceptibility Mapping, ISMRM 2015

12) Jingwei Zhang, Cynthia Wisnieff, Becky Schur, Lu Zhengrong, David Pitt, Yi Wang, Abstract 1707, Traditional Poster, Measurement of Brain Iron and Calcium Using MR QSM and CT: Validation Using Inductively Coupled Plasma Optical Emission Spectrometry (ICP-OES), ISMRM2015

13) Jingwei Zhang, Thanh D. Nguyen, Pascal Spincemaille, Tian Liu, Dong Zhou, Ajay Gupta, Yi Wang, Abstract 3940, electronic poster, High Resolution Cerebral Metabolic Rate of Oxygen (CMRO2) Using Quantitative Susceptibility Mapping (QSM) and an Oxygen Extraction Fraction (OEF) Constraint, ISMRM2015

14) Jingwei Zhang, Dong Zhou, Sarah Eskreis-Winkler, Thanh Nguyen, Pascal Spincemaille, Ajay Gupta, and Yi Wang, Abstract 603, oral presentation, Quantitative Susceptibility Mapping (QSM) based Cerebral Metabolic Rate of Oxygen (CMRO2) Mapping: Eliminating Blood Flow Challenge with Minimal Local Variance (MLV), ISMRM 2016

15) Jingwei Zhang, Dong Zhou, Thanh Nguyen, Pascal Spincemaille, Ajay Gupta, and Yi Wang, Abstract 1719, electronic poster, Quantitative Susceptibility Mapping (QSM) based Cerebral Metabolic Rate of Oxygen (CMRO2) Mapping: Improve Robustness with Preconditioning and Physiological Constraints, ISMRM 2016

Awards

1) Distinction, Jingwei Zhang, Tian Liu, Ajay Gupta, Pina C. Sanelli, Cynthia Wisnieff, Pascal Spincemaille, and Yi Wang, Abstract, traditional poster, Cerebral Metabolic Rate of Oxygen ($CMRO_2$) Mapping Using Quantitative Susceptibility Mapping (QSM), 25th International Workshop on Magnetic Resonance Angiography, 2013

2) Magna Cum Laude, Jingwei Zhang, Thanh D. Nguyen, Xavier J. Candela, Kory P. Witmer, Keefe B. Manning, and Yi Wang, Abstract 0112, oral presentation, Quantitative Relaxation Time and Susceptibility Mapping of Thrombus, ISMRM 2014

3) Summa Cum Laude, Jingwei Zhang, Dong Zhou, Sarah Eskreis-Winkler, Thanh Nguyen, Pascal Spincemaille, Ajay Gupta, and Yi Wang, Abstract 603, oral presentation, Quantitative Susceptibility Mapping (QSM) based Cerebral Metabolic Rate of Oxygen (CMRO2) Mapping: Eliminating Blood Flow Challenge with Minimal Local Variance (MLV), ISMRM 2016

REFERENCES

1. Atlas S, Thulborn K. Magnetic resonance imaging of the brain and spine. 3rd ed. Philadelphia: Lippincott Williams & Wilkins. Intracranial hemorrhage 2002:773-832.

2. Kidwell CS, Wintermark M. Imaging of intracranial haemorrhage. Lancet neurology 2008;7(3):256-267.

3. de Rochefort L, Liu T, Kressler B, Liu J, Spincemaille P, Lebon V, Wu J, Wang Y. Quantitative susceptibility map reconstruction from MR phase data using bayesian regularization: validation and application to brain imaging. Magnetic resonance in medicine : official journal of the Society of Magnetic Resonance in Medicine / Society of Magnetic Resonance in Medicine 2010;63(1):194-206.

4. Derdeyn CP, Videen TO, Yundt KD, Fritsch SM, Carpenter DA, Grubb RL, Powers WJ. Variability of cerebral blood volume and oxygen extraction: stages of cerebral haemodynamic impairment revisited. Brain : a journal of neurology 2002;125(Pt 3):595-607.

5. Gupta A, Chazen JL, Hartman M, Delgado D, Anumula N, Shao H, Mazumdar M, Segal AZ, Kamel H, Leifer D, Sanelli PC. Cerebrovascular reserve and stroke risk in patients with carotid stenosis or occlusion: a systematic review and meta-analysis. Stroke; a journal of cerebral circulation 2012;43(11):2884-2891.

6. Gupta A, Baradaran H, Schweitzer AD, Kamel H, Pandya A, Delgado D, Wright D, Hurtado-Rua S, Wang Y, Sanelli PC. Oxygen extraction fraction and stroke risk in patients with carotid stenosis or occlusion: a systematic review and meta-analysis. AJNR American journal of neuroradiology 2014;35(2):250-255.

7. Pauling L, Coryell CD. The Magnetic Properties and Structure of Hemoglobin, Oxyhemoglobin and Carbonmonoxyhemoglobin. Proceedings of the National Academy of Sciences of the United States of America 1936;22(4):210-216.

8. Ogawa S, Lee TM, Kay AR, Tank DW. Brain magnetic resonance imaging with contrast dependent on blood oxygenation. Proceedings of the National Academy of Sciences of the United States of America 1990;87(24):9868-9872.

9. Bolar DS, Rosen BR, Sorensen AG, Adalsteinsson E. QUantitative Imaging of eXtraction of oxygen and TIssue consumption (QUIXOTIC) using venular-targeted velocity-selective spin labeling. Magnetic resonance in medicine : official journal of the Society of Magnetic Resonance in Medicine / Society of Magnetic Resonance in Medicine 2011;66(6):1550-1562.

10. Bulte DP, Kelly M, Germuska M, Xie J, Chappell MA, Okell TW, Bright MG, Jezzard P. Quantitative measurement of cerebral physiology using respiratory-calibrated MRI. NeuroImage 2012;60(1):582-591.

11. Gauthier CJ, Hoge RD. Magnetic resonance imaging of resting OEF and CMRO(2) using a generalized calibration model for hypercapnia and hyperoxia. NeuroImage 2012;60(2):1212-1225.

12. Wise RG, Harris AD, Stone AJ, Murphy K. Measurement of OEF and absolute CMRO2: MRI-based methods using interleaved and combined hypercapnia and hyperoxia. NeuroImage 2013;83:135-147.

13. An H, Lin W. Impact of intravascular signal on quantitative measures of cerebral oxygen extraction and blood volume under normo- and hypercapnic conditions using an asymmetric spin echo approach. Magnetic resonance in medicine : official journal of the Society of Magnetic Resonance in Medicine / Society of Magnetic Resonance in Medicine 2003;50(4):708-716.

14. An H, Ford AL, Chen Y, Zhu H, Ponisio R, Kumar G, Shanechi AM, Khoury N, Vo KD, Williams J, Derdeyn CP, Diringer MN, Panagos P, Powers WJ, Lee JM, Lin W. Defining the ischemic penumbra using magnetic resonance oxygen metabolic index. Stroke; a journal of cerebral circulation 2015;46(4):982-988.

15. Ulrich X, Yablonskiy DA. Separation of cellular and BOLD contributions to T2* signal relaxation. Magnetic resonance in medicine 2015:doi: 10.1002/mrm.25610.

Chapter 2

Background

2.1 MRI PHYSICS

2.1.1 Signal Generation

A nucleus with an uneven atomic number possesses an intrinsic angular momentum. Combined with its net positive charge a net magnetic moment is formed. In MRI, such nucleus is referred to as a spin. This spin precession phenomenon can be described by Eq [2.1].

$$\frac{d\mu}{dt} = \gamma\mu \times B_0 \qquad [2.1]$$

Here B0 is an external magnetic field. μ is the magnetic moment precesses along B0 direction (z). $\gamma = 42.58MHz/T$ is gyromagnetic ratio for proton.

Under normal conditions, there is no net magnetic moment in a bulk sample since the spins are randomly orientated. When the sample such as water is placed in an external magnetic field B0, the spins of ^{1}H nucleus tend to align with B0 in a parallel or an anti-parallel fashion. Since the parallel state has lower energy, a larger number of spins adopt this state and create a net magnetic moment.

To generate MRI signal, a process called RF excitation is used. In this process, a radio frequency field (RF) B1, often at gyromagnetic frequency for efficiency, is applied for a short period time to tip the spin away from B0 direction for a certain degree (flip angle), forming a magnetization component in the transverse plane (x,y). After RF excitation, spins try to re-align with B0 due to energy exchange of spins and their surroundings. The longitudinal bulk magnetization M_z recovers to M0 in time T_1, or spin-

lattice relaxation time. Transverse magnetization M_{xy} decays in time T_2, or spin-spin relaxation time. The bulk magnetization after RF excitation can be described using Bloch equation [2.2]:

$$\frac{dM}{dt} = (\gamma M \times B) - \frac{(M_z - M_z^0)\hat{z}}{T_1} - \frac{M_x\hat{x} + M_y\hat{y}}{T_2} \quad [2.2]$$

Signals generated by this transverse magnetization can be detected by MRI. The different T1 and T2 of various tissue types generate contrasts on T1w and T2w images.

2.1.2 Signal Encoding

To spatially encode spins, a magnetic field gradient G is used. At each location x, the spin experiences a slightly different magnetic field, B0 and ΔB(x). The precession frequency ω can be written as

$$\omega(x) = \gamma\big(B_0 + \Delta B(x)\big). \quad [2.3]$$

The gradient used in MRI is often linear in space and its magnitude varies in time t. Hence,

$$xG(t) = \Delta B(x,t), \quad [2.4]$$

Here G(t) is the vector of gradient in T/m at time t. The signal S(t) can then be expressed as

$$S(t) = \int_{-\infty}^{\infty} C(x)\rho(x)e^{-i\gamma\int_0^t G(\tau)d\tau x}dx. \quad [2.5]$$

Here x is the spatial coordinate. C(x) is the sensitivity of the coil. ρ(x) is proton density including the relaxation effect. Equation 2.5 can be rewritten in k-space coordinate with

$$k(t) = \gamma \int_0^t G(\tau) d\tau \quad [2.6]$$

Substituting Eq. 2.6 into Eq. 2.5, we have

$$S(k) = \int_{-\infty}^{\infty} C(x)\rho(x)e^{-ikx}dx. \quad [2.7]$$

From Eq. 2.7, the signal acquired by MRI S(k) is the spatial Fourier transform of the object being imaged.

2.1.3 Signal Acquisition

During imaging, M_{xy} varies over time which generates magnetic flux and electric current in receiver coils. Two of the most common acquisition sequences are spin echo and gradient echo. In the case of spin echo, a 90° RF pulse followed by another 180° refocusing RF pulse are used. The 90° pulse transfer z magnetization (M_z) completely to transverse plane (M_{xy}). The refocusing RF reverse effects induced by field inhomogeneities. With sufficient magnetization recovery time this combination allows the largest possible signal and the minimal field inhomogeneities effects, which is ideal for imaging quality. Spin echo sequence can produce T1w, T2w and proton density (PD) weighted images depending on time of echo (TE) and time of repetition (TR). However, in general spin echo sequences require longer acquisition time.

Unlike spin echo, gradient echo uses a single excitation pulse with a flip angle α followed by a gradient pulse to create the echo. This pulse sequence can also produce T1w, T2w, and PD-weighted images with much shorter acquisition time due to its shorter TRs. However, they are affected by magnetic field inhomogeneity and imaging parameters such as flip angle, TE and TR. This shortens the apparent spin-spin relaxation time. The combined decay rate, T2 and field inhomogeneity, is known as T2*.

$$\frac{1}{T2^*} = \frac{1}{T2} + \frac{1}{T2'} \; or \; R2^* = R2 + R2' \qquad [2.8]$$

After data acquisition any residual transverse magnetization can form a Hahn or partial echo, which can be refocused by subsequent RF pulses and corrupt the images. One way to counter this issue is to apply a large gradient between data acquisition and the next RF pulse to completely dephase or to spoil the residual transverse magnetization. This type of sequence is called spoiled gradient echo (SPGR), which is the primary type used in this dissertation for GRE magnitude images, R2* maps, and quantitative susceptibility maps (QSM).

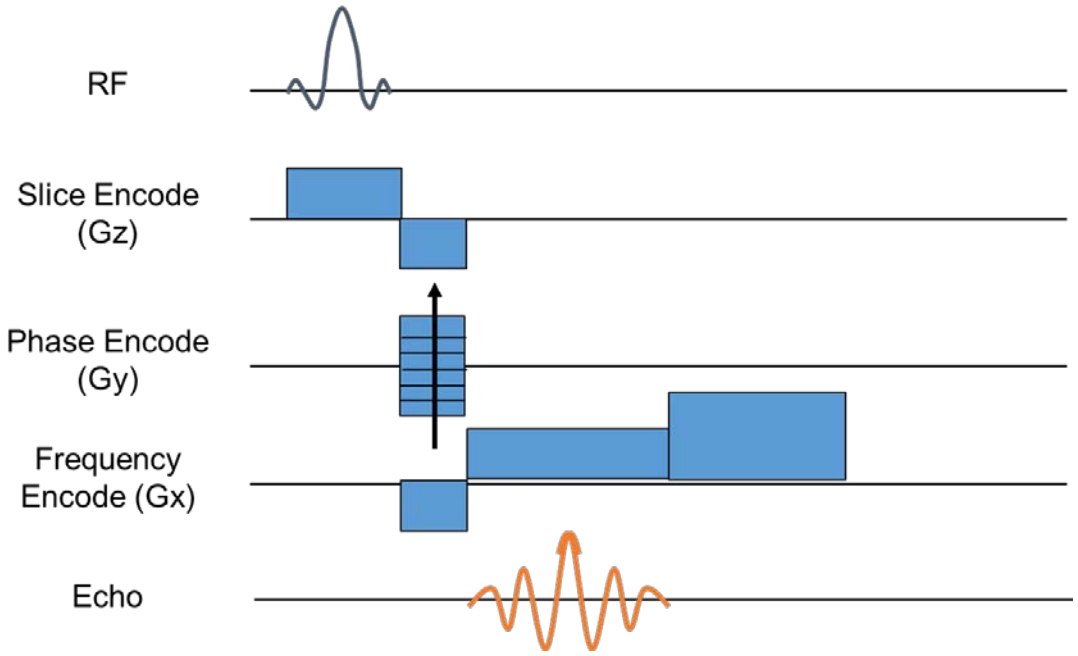

Figure 2.1. Pulse diagram of SPGR. A large gradient is played out between data acquisition and the next RF pulse to completely dephase or to spoil the residual transverse magnetization.

2.1.4 Sampling Trajectory

There are several k-space sampling strategies. Cartesian sampling is one of the most common strategies where k-space is sampled line by line. This is achieved by playing out gradients along x, y and z axis to offset to appropriate k-space coordinate after applying a RF and a slice selection gradient. Then a readout gradient is applied on the x-axis, moving the trajectory in the x-axis direction and sampling one k-space line. After readout y and z axis gradients are rewound. A spoiler gradient is played on x-axis to spoil any residual

magnetization to prevent Hahn echo. This is the primary sampling strategy for SPGR sequence in this dissertation.

2.1.5 Image Reconstruction

The signal acquired by MRI is the spatial Fourier transform of the object being imaged. However, in real world it is impossible to sample the continuum of k-space. If the data is sampled on a Cartesian grid that satisfies Nyquist theorem, an inverse discrete Fourier transform (DFT) can be performed to reconstruct images.

$$\hat{\rho}(x,y,z) = \frac{1}{\sqrt{N_x N_y N_z}} \sum_{l=0}^{N_x-1} \sum_{m=0}^{N_y-1} \sum_{n=0}^{N_z-1} S(l,m,n) e^{i2\pi xl/N_x} e^{i2\pi ym/N_y} e^{i2\pi zn/N_z} \quad [2.8]$$

where $\hat{\rho}(x,y,z)$ is the magnetization distribution of the imaging object in real space. x, y, z is the coordinates in real space. l, m, n is the coordinates in k-space. Nx, Ny and Nz are the number of k-space sampling points in three axis. In practice, inverse fast Fourier transform (FFT) is used to reduce the reconstruction time.

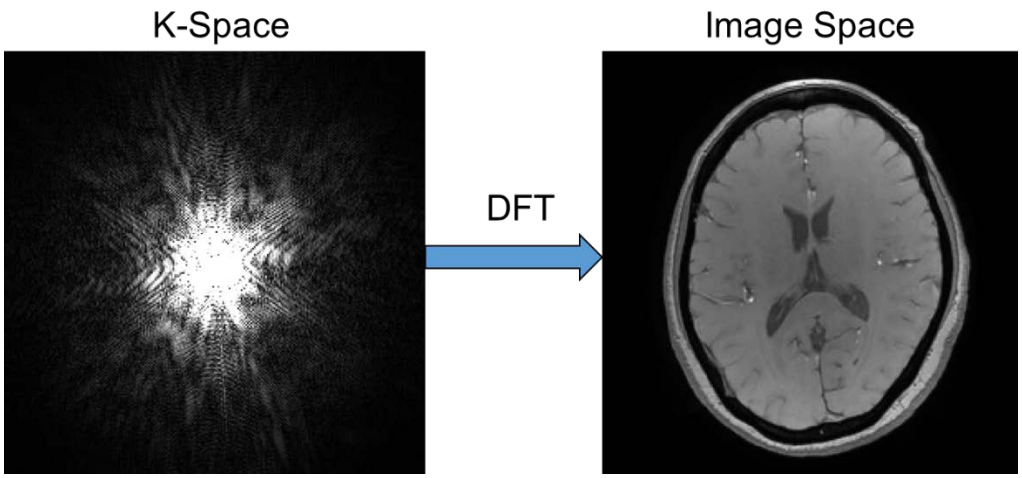

Figure 2.2. Images are obtained after performing DFT on K-space data.

2.1.6 Parallel Imaging

In modern MRI scanners, most receiver coils consist of array of coil elements. Each coil element has its own coverage and sensitivity. This design allows accelerated data acquisition through parallel imaging. There are two main categories: k-space based and image-space based. A typical k-space based method is called GeneRalized Autocalibrating Partially Parallel Acquisitions (GRAPPA) which takes advantage of the smoothness of coil sensitivity and reformats k-space points as a weighted average of the surrounding points and/or the points from other coils.

In this thesis, an image-space based accelerating technique called Array Spatial Sensitivity Encoding Technique (ASSET, GE health care) is used (1). ASSET is based on the SENSitivity Encoding (SENSE) method (2). Assuming the accelerating factor is R, each voxel in the aliased coil image is the sum of R voxels in the fully sampled coil image

weighted by the coil sensitivity. With measurements from multiple coils, a linear system can be constructed.

$$\begin{bmatrix} \widehat{\rho_1} \\ \widehat{\rho_2} \\ \vdots \\ \widehat{\rho_{Nc}} \end{bmatrix} = \begin{bmatrix} C_{1,1} & C_{1,2} & \dots & C_{1,R} \\ C_{2,1} & C_{2,2} & \cdots & C_{2,R} \\ \vdots & \vdots & \ddots & \vdots \\ C_{Nc,1} & C_{Nc,2} & \cdots & C_{Nc,R} \end{bmatrix} \begin{bmatrix} \rho_1 \\ \rho_2 \\ \vdots \\ \rho_R \end{bmatrix} \quad [2.9]$$

Here $C_{m,n}$ is the sensitivity of coil m at location n. Nc is the number of coil elements. $\hat{\rho}$ is a voxel of aliased coil images from different coils. ρ are the voxels from different locations of the fully sampled image. When the linear system is over determined, or Nc > R, fully sampled images can be calculated by solving Eq. 2.9.

2.2 QUANTITATIVE SUSCEPTIBILITY MAPPING

Magnetic susceptibility is a physical quantity that measure the degree of magnetization of a material in response to an applied magnetic field. Many biomolecules such as hemoglobin and bone contain iron and calcium ions and have different magnetic susceptibility. QSM quantitatively maps tissue magnetic susceptibilities, opening a new venue to quantify these biomolecules.

The unit for volume susceptibility is ml/ml, or unitless. The unit for molar susceptibility is m^3/mol (SI), or cm^3/mol (CGS). The conversion of volume susceptibility between SI and CGS is

$$x_v^{SI} = 4\pi x_v^{CGS} \quad [2.10]$$

In this dissertation, SI units are used unless otherwise notice. All magnetic susceptibility is relative to water / cerebrospinal fluid (CSF) unless otherwise notice.

2.2.1 Foundations of QSM

The longitudinal magnetic field induced by the imaging object can be expressed as (3)

$$\delta_b(r) = d(r) \otimes x(r) \quad [2.11]$$

Where r is the spatial coordinate. $\delta_b(r)$ is the magnetic field induced by the imaging object scaled by B0, also known as the local field. This is obtained after removing background field generated by large susceptibility sources such as air, bone, and fat outside the volume of interest from the total field. In this dissertation, projection onto dipole fields (PDF) is the primary algorithm for background field removal (4). $x(r)$ is the spatial susceptibility distribution of the imaging object. $\otimes$ is the convolution operator. $d(r)$ is the dipole kernel.

$$d(r) = \frac{3cos^2\theta - 1}{4\pi r^3} \quad [2.12]$$

Θ is the angle between $r - r'$ and B0. Eq. 2.11 can be expanded as (5)

$$\delta_b(r) = \int_{r' \neq r} x(r') \frac{3cos^2(\theta_{r-r'}) - 1}{4\pi |r' - r|^3} d^3r' \quad [2.13]$$

$x(r)$ can be computed by de-convolution of the dipole kernel $d(r)$. For efficiency the convolution is executed as a multiplication in k-space. However, the dipole kernel is zero

at the cone surface $3cos^2\theta = 1, \theta = \pm 54.7^o$ in both image and k spaces. This leads to ill-posedness in the inversion. There are several approaches to encounter the ill-posedness (6): 1) Calculation Of Susceptibility through Multiple Orientation Sampling (COSMOS) where the ill-posedness is solved by oversampling from multiple orientations; 2) Thresholded k-space division (TKD) where underdetermined k-space data of the dipole kernel are set to a predetermined non-zero value; 2) Morphological-enabled dipole inversion (MEDI) where structural prior generated from GRE magnitude images are incorporated in the de-convolution. In this dissertation, MEDI is the primary algorithm for QSM reconstruction.

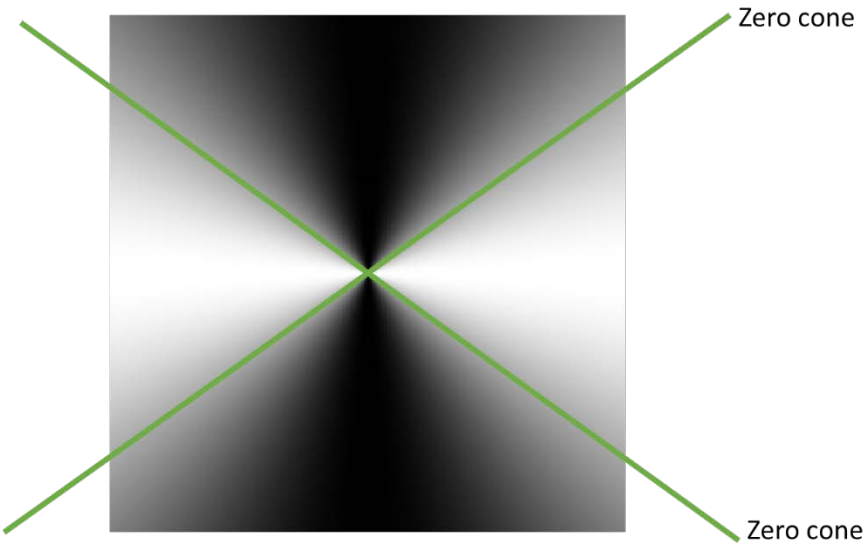

Figure 2.3. Zero cone surface at $\theta = \pm 54.7^o$ of dipole kernel in K space.

2.2.2 Morphology-Enabled Dipole Inversion (MEDI)

From COSMOS results we observed that the structural edges in the susceptibility maps closely match the edges of GRE magnitude images generated from the same data.

MEDI takes advantage of this observation and employs a weighted L1 minimization to penalize susceptibility voxels that are not parts of edges on GRE magnitude images. The cost function is (7):

$$x = \underset{x}{\operatorname{argmin}} \|M\nabla x\|_1 + \lambda \|W(\delta - F_D x)\|_2^2 \qquad [2.14]$$

Here ∇ is a 3D gradient operator that generate edge maps on susceptibility map x in x,y, and z directions. M is a binary edge maps generated from GRE magnitude images where the voxel value is zero when its gradient is significant (5 times larger than noise), and is one otherwise. Λ is reconstruction parameter. W is a weighting matrix based on SNR. F_D is

$$F_D = F^{-1}DF \qquad [2.15]$$

Where D is the dipole kernel expressed in the Fourier domain.

Susceptibility map x is obtained by solving Eq. 2.15 using a conjugated gradient method with λ determined by L-curve. Typical λ for a 3T MRI scanner is ranged from 500 to 1500.

2.3 ARTERIAL SPIN LABELING (ASL) AND CEREBRAL BLOOD FLOW MAPPING

Blood flow is critical in oxygen and nutrients delivery to tissues, especially in brain. Usually quantified in the unit of ml per 100g of tissue per min, cerebral blood flow (CBF) can be measured using a tracer in blood (8). This tracer can 1) emit radioactive signal and detected by positron emission tomography (PET); 2) increase signal attenuation and detected by computed tomography; 3) increase magnetization and detected by MRI.

Arterial spin labeling is a non-invasive MRI technique for quantitatively mapping CBF without contrast agent, which is the primary technique used in this dissertation.

2.3.1 Foundations of ASL

During ASL scanning, a pair of control and tagged images were acquired. In the tagged images, water protons in arterial blood downstream, usually in the neck region, are magnetically labelled using 180 degree RF inversion pulses. After some delay time, the labelled blood reached capillaries where it exchanges with tissue water and reduces total tissue magnetization. By subtracting tag from control images any static tissue signal is removed. The remaining signal is proportional to CBF.

There are several ASL variants (8): 1) continuous ASL (CASL) utilizes a continuous RF pulse (2~4 sec) in combination with a slice-selective gradient to tag arterial blood in a narrow plane just below imaging plane. This in theory allows high SNR. However, CASL

has several drawbacks such as magnetization transfer effects, high specific absorption rate (SAR), and requirement of additional hardware. 2) pulse ASL (PASL) utilizes short RF pulses to tag a blood volume (tag region). PASL has advantages of ease of implementations and reduced MT effects. However, it is sensitive to transit delay, time needed for tag blood to flow from tag region to imaging plane. The SNR also suffered compared to CASL. 3) pseudo-Continuous ASL (pCASL) is hybrid between CASL and PASL. This technique utilizes a chain of discrete RF pulses in combination with a gradient wave to mimic CASL's continuous RF pulses for tagging. This technique has advantages of reduce MT effects, no need for additional hardware, and relative high SNR. The main disadvantages are susceptible to field inhomogeneity, eddy currents and post label delay time. In this dissertation, 3DASL, variation of pCASL from GE healthcare is the primary technique for CBF maps.

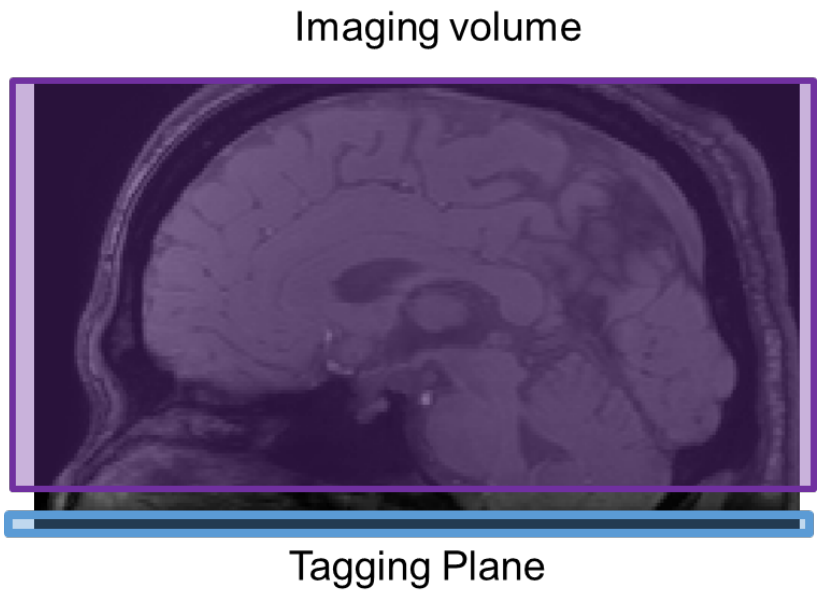

Figure 2.4. PCASL tagging plane and imaging volume.

2.3.2 pCASL Post Processing

CBF images were calculated using a single-compartment model after subtraction of labeled from control images (9,10).

$$CBF = \lambda(1 - e^{-T_{SAT}/T1_{GM}}) \times \frac{e^{w/T1_B}}{2T1_B(1-e^{-\tau/T1_B})\varepsilon NEX} \frac{\Delta S}{S_0} \quad [2.16]$$

Here $\lambda = 0.9$ is partition coefficient. $T_{SAT} = 2$ sec is saturation recovery time for proton density weighted (PDw) images. $T1_{GM} = 1.2$ sec is the correction for saturation recovery on PDw images. $w = 1.5$ sec is the post label delay. $T1_B = 1.6$ sec is T1 of blood at 3.0 T. $\tau = 1.5$ sec is labeling time. $\varepsilon = 0.6$ is labeling efficiency. NEX is the number of excitation for perfusion weighted images, or raw difference images. ΔS is the raw difference images. S_0 is the PDw images.

This a single-compartment model and equation have been commercialized in GE FuncTool post processing software and it is used for CBF maps computation in this dissertation.

REFERENCES

1. King KF. ASSET – Parallel Imaging on the GE Scanner GE Healthcare, Milwaukee, WI, http://www.mr.ethz.ch/parallelmri04/abstracts/pub/King.pdf, Retrieved date Dec 29th 2016.

2. Pruessmann KP, Weiger M, Scheidegger MB, Boesiger P. SENSE: sensitivity encoding for fast MRI. Magnetic resonance in medicine : official journal of the Society of Magnetic Resonance in Medicine / Society of Magnetic Resonance in Medicine 1999;42(5):952-962.

3. Wang Y. Quantitative Susceptibility Mapping: Magnetic Resonance Imaging of Tissue Magnetism. www.createspace.com/4346993June 2013.

4. Liu T, Khalidov I, de Rochefort L, Spincemaille P, Liu J, Tsiouris AJ, Wang Y. A novel background field removal method for MRI using projection onto dipole fields (PDF). NMR in biomedicine 2011;24(9):1129-1136.

5. Liu J, Liu T, de Rochefort L, Ledoux J, Khalidov I, Chen W, Tsiouris AJ, Wisnieff C, Spincemaille P, Prince MR, Wang Y. Morphology enabled dipole inversion for quantitative susceptibility mapping using structural consistency between the magnitude image and the susceptibility map. NeuroImage 2012;59(3):2560-2568.

6. Deistung A, Schweser F, Reichenbach JR. Overview of quantitative susceptibility mapping. NMR in biomedicine 2016.

7. Liu T, Liu J, de Rochefort L, Spincemaille P, Khalidov I, Ledoux JR, Wang Y. Morphology enabled dipole inversion (MEDI) from a single-angle acquisition: comparison with COSMOS in human brain imaging. Magnetic resonance in medicine : official journal of the Society of Magnetic Resonance in Medicine / Society of Magnetic Resonance in Medicine 2011;66(3):777-783.

8. Petcharunpaisan S, Ramalho J, Castillo M. Arterial spin labeling in neuroimaging. World journal of radiology 2010;2(10):384-398.

9. Binnewijzend MA, Kuijer JP, Benedictus MR, van der Flier WM, Wink AM, Wattjes MP, van Berckel BN, Scheltens P, Barkhof F. Cerebral blood flow measured with 3D pseudocontinuous arterial spin-labeling MR imaging in Alzheimer disease and mild cognitive impairment: a marker for disease severity. Radiology 2013;267(1):221-230.

10. Buxton RB, Frank LR, Wong EC, Siewert B, Warach S, Edelman RR. A general kinetic model for quantitative perfusion imaging with arterial spin labeling. Magnetic resonance in medicine : official journal of the Society of Magnetic Resonance in Medicine / Society of Magnetic Resonance in Medicine 1998;40(3):383-396.

Chapter 3

Investigation of Blood Degradation in Hemorrhagic Patients Using QSM

3.1 ABSTRACT

Purpose:

To investigate the magnetic susceptibility of intracerebral hemorrhages (ICH) at various stages by applying quantitative susceptibility mapping (QSM).

Materials and Methods:

Blood susceptibility was measured serially using QSM after venous blood withdrawal from healthy subjects. Forty-two patients who provided written consent were recruited in this institutional review board approved study. Gradient echo MRI data of the 42 patients (17 females; 64±12 yrs) with ICH were processed with QSM. The susceptibilities of various blood products within hematomas were measured on QSM.

Results:

Blood susceptibility continually increased and reached a plateau 96 hours after venous blood withdrawal. Hematomas at all stages were consistently hyperintense on QSM. Susceptibility was 0.57 ± 0.48, 1.30 ± 0.33, 1.14 ± 0.46, 0.40 ± 0.13, and 0.71 ± 0.31 parts per million (ppm) for hyperacute, acute, early subacute, late subacute and chronic stages of hematomas respectively. The susceptibility decrease from early subacute (1.14ppm) to late subacute (0.4ppm) was significant ($p<0.01$).

Conclusion:

QSM reveals positive susceptibility in hyperacute hematomas, indicating that even at their hyperacute stage, deoxyhemoglobin may exist throughout the hematoma volume, not just at its rim as seen on conventional T2* imaging. QSM also reveals reduction of susceptibility from early subacute to late subacute ICH, suggesting that methemoglobin concentration decreases at the late subacute stage.

Keywords: Magnetic Susceptibility, QSM, Intracerebral Hemorrhage, CT

3.2 INTRODUCTION: MRI IN HEMORRHAGIC PATIENTS

The blood degradation process in intracerebral hemorrhage (ICH) has been characterized qualitatively but not quantitatively on MRI using standard T1 weighted (T1w), T2 weighted (T2w), and T2* weighted gradient echo (T2*w) imaging (1-3). It is generally assumed that blood degradation products in intracerebral hematomas are composed primarily of oxyhemoglobin (oxyHb) in the hyperacute stage (<24h), deoxyhemoglobin (deoxyHb) in the acute stage (1~3 days), intracellular methemoglobin (metHb) in the early subacute stage (3~7 days), extracellular metHb in the late subacute stage (7~14 days), and hemosiderin in the chronic stage (>14 days). During blood degradation, the molar magnetic susceptibility monotonically increases, from slightly negative relative to CSF in oxyHb to highly positive in deoxyHb, metHb, and hemosiderin.

Quantitative Susceptibility Mapping (QSM) has recently been applied to quantify cerebral microbleed burden (4), hematoma volume (5), blood leakage in cerebral cavernous malformation (6,7) , and to differentiate hemorrhages from calcifications (8,9). Because QSM directly quantifies the magnetic susceptibility of tissue, it provides an opportunity to quantitatively characterize hematomas by using MRI, especially at the hyperacute/acute phase where treatment is critically needed. Here, we apply QSM to investigate the magnetic susceptibility of hematomas at various stages.

3.3 EXPERIMENTS AND ANALYSIS

The susceptibility of hematomas was investigated using QSM of blood drawn from healthy subjects and using QSM performed in ICH patients at various stages. All magnetic susceptibility reported in this study were measured in SI units relative the cerebral spinal fluid (CSF) in subjects and relative to water in phantoms.

3.3.1 Blood Experiment

The blood experiment was approved by our institutional review board to study the change in blood susceptibility over time following venous blood withdrawal from healthy subjects. A phantom was constructed with 5mL transfer pipets (Thermo Scientific, Waltham, MA) embedded in a plastic container with 1% agar solution to support the blood tube. The same procedure was repeated on five healthy volunteers. For each subject, 5 ml venous blood was drawn and immediately injected into the tube. The plastic container was kept in a 37°C water bath when not being scanned. The first scan started immediately after blood withdrawal. The blood phantom was scanned every hour during the first 8 hours, then at 16 hours, 24 hours, and every day thereafter up to 7 days.

3.3.2 Patient Experiment

This study was approved by our institutional review board and written consent was obtained from patients or their families. From September 2010 to December 2012, patients suspected of hemorrhagic strokes were prescribed either MRI or CT and were recruited for this study. After their conditions stabilized, a follow-up CT or MRI scan that was complementary to the initial scan was performed. If the initial scan was an MRI scan and the hematoma was chronic, the follow-up CT scan was sometimes omitted. 42 patients (25 males and 17 females; 41~89 years old, mean ± standard deviation, 64±12) with hematomas at various stages were scanned consecutively during this time period and included in this study. The interval between CT and MR imaging ranged from less than an hour to 8 days, but only seven of them were longer than 25 hours, resulting in a mean interval of 37 hours and a median of 2 hours. At the time of the initial scan, the symptom duration was less than 24 hours for 4 patients, 1~3 days for 10 patients, 3~7 days for 5 patients, 7~14 days for 11 patients, and more than 14 days for 12 patients. After screening the images, one patient in the >14 days category was excluded due to corrupted image quality in QSM.

3.3.3 Imaging Protocol and Data Reconstruction

3.3.3.1 Blood Experiment

3D multi-echo spoiled gradient echo (SPGR) were acquired on a 3.0 Tesla MR system (Signa HDx, GE, United States) using an 8-channel brain coil. The imaging parameters were: flip angle = 25º, first TE=2.1 ms, echo spacing=2.8 ms, 11 echos, TR=33.4 ms, voxel size=1x1x1 mm^3, scan time = 4 mins; QSM images were calculated from gradient echo complex images using the morphology enabled dipole inversion method (3,10,11).

3.3.3.2 Patient Experiment

MRI was performed on a 3.0 Tesla MR system (Magnetom Verio, Siemens, Erlangen, Germany) using a 12-channel head coil with the following pulse sequences: (a) T1-weighted (T1w) spin echo (TR = 431ms, TE = 13ms) (b) T2-weighted fluid-attenuated inversion recovery (T2w-FLAIR, TR = 6.4s, TE = 110ms, TI = 2s) or T2-weighted images (T2w, TR = 9s, TE =100ms), and (c) 3D T2*-weighted spoiled multiecho gradient echo (T2*w). Imaging parameters for the multi-echo GRE sequence were as follows: flip angle, 15°; repetition time, 58 msec; number of echoes, 8; first echo time, 5.7 msec; echo time spacing, 6.7 msec; pixel bandwidth, 500Hz; field of view, 24 cm; matrix, 384 × 288; section thickness, 2 mm; parallel imaging acceleration factor, 2; and total acquisition time, about 6 minutes. T2*w magnitude images were reconstructed by taking the square root of

sum of squares of all the echoes. The QSM was reconstructed from the multiecho GRE data using the morphology enabled dipole inversion method (10-12).

CT was performed using a 64-detector CT scanner (Lightspeed VCT; GE Healthcare, Milwaukee, WI) with the following parameters: 260 mAs, 120 kV, 5mm slice thickness, 1.375:1 pitch, and 512 × 512 matrix.

3.3.4 Image Analysis

3.3.4.1 Blood Experiment

Regions of interest (ROIs) covering the entire clot were manually drawn and used to measure the mean and standard deviation of susceptibilities at different time points.

3.3.4.2 Patient Experiment

Two neuroradiologists with at least 10 year-experience classified the ages of the hematomas as hyperacute, acute, early subacute, late subacute, and chronic stages, and corresponding blood products, based on characteristic signal intensity patterns on T1w, T2w-FLAIR, T2*w MRI and CT (2,13). A hematoma might have multiple ROIs (Fig. 3.1). Susceptibility values were measured from QSM on ROIs of the same blood product. Cerebrospinal fluid (CSF) susceptibility values in the lateral ventricles without evidence of hemorrhages were used as the susceptibility reference. For each type of blood product, the mean and standard deviation of the blood products' susceptibility values were recorded.

3.3.5 Statistical Analysis

QSM ROI measurements were grouped based on their hematomas stages and the corresponding blood products in statistical analysis. One-way analysis of variance (ANOVA) was performed to assess if the susceptibility differences among the five stages were significant. One-sample t-tests with a significance level of 5% were performed to

assess if measured susceptibility values in each stage were significantly above zero (relative to CSF). Two-sample unpaired t-tests with intracluster correlation adjustments for multiple ROIs within the same patient (14) and a significance level of 5% were performed to assess if the susceptibility changes between two consecutive stages were statistically significant: hyperacute vs acute, acute vs early subacute, early subacute vs late subacute, and late subacute vs chronic.

3.4 RESULTS

3.4.1 Blood Experiment

Blood coagulated about 9 min after drawing. Hematoma retraction started immediately after coagulation and stabilized within 1-2 hours. Figure 3.3 shows the time course of blood clot susceptibilities (n = 5). Susceptibility monotonically increased from 456±91 ppb (parts per billion) at the start to a plateau of 1509±60 ppb beginning at 96 hours.

3.4.2 Patients Experiment

There were 47 hematomas identified in this study: 4 hyperacute, 5 acute, 15 early subacute, 16 late subacute, and 7 chronic. Susceptibility measurements on a total of 78 ROIs were: 0.57 ± 0.48 parts per million (ppm) from 11 ROIs denoting oxyHb mixed with deoxyHb from 11 patients, 1.30 ± 0.33 ppm from 27 ROIs denoting deoxyHb from 26 patients, 1.14 ± 0.46 ppm from 13 ROIs denoting intracellular metHb from 13 patients, 0.40 ± 0.13 ppm from 15 ROIs denoting extracellular metHb from 15 patients, and 0.71 ± 0.31 ppm from 12 ROIs denoting hemosiderin from 10 patients (Fig. 3.4). All values were significantly greater than zero ($p<0.01$). The susceptibility differences among the five stages were significant ($p<0.01$, ANOVA). Figure 3.5 depicts a typical case of a hyperacute hematoma having positive susceptibility throughout its volume on QSM and hypointensity at its rim on T2w-FLAIR and T2*w. Figure 3.6 illustrates a typical case of an acute

hematoma having a core that is hyperintense on QSM but hypointense on T2w-FLAIR and T2*w, and isointense on T1w. Figure 3.7 shows typical early and late subacute hematomas, demonstrating a reduction of susceptibility in the late subacute stage.

The susceptibility value at the hyperacute stage (0.57 ppm) was significantly greater than zero ($p<0.01$), suggesting an oxy-deoxyHb mixture. Compared to hyperacute, a significant increase of 0.73ppm ($p<0.05$, df = 14, 32 patients with 5 patients have ROIs in both stages) in hematoma susceptibility was found in the acute stage. A statistically insignificant ($p=0.12$, df = 18, 32 patients with 7 patients have ROIs in both stages) decrease in susceptibility of -0.17ppm was found in early subacute (intracellular metHb) stage when compared to that in the acute stage (deoxyHb). There was an unexpected significant decrease of -0.74 ppm ($p<0.01$, df = 14, 25 patients with 3 patients have ROIs in both stages) in susceptibility from early subacute (intracellular metHB) to late subacute stage (extracellular metHb; Figs. 3.4 & 3.7). There was a significant increase of 0.31 ppm ($p<0.01$, df = 14, 23 patients with 2 patients have ROIs in both stages) in susceptibility from late subacute (extracellular metHB) to chronic stage (hemosiderin).

3.5 DISCUSSION

Data from this QSM study of intracerebral hematomas of various stages suggest the following two findings. 1) The susceptibility of hematomas are consistently positive relative to CSF even during the hyperacute stage, challenging the traditional model that hyperacute hematomas contain mostly oxygenated arterial blood which has slightly negative susceptibility (15,16). 2) The susceptibilities of hematomas decrease substantially from the acute to subacute stage, thus furthering the MRI literature (1,13) about the late subacute stage with new insight for a quantitative model to explain the hemoglobin degradation process.

In the phantom experiment, the blood susceptibility experienced its most rapid increase (0.070 ± 0.014 ppm/hour) during the first 8 hours. In the patient data, the quantitative measurement of susceptibility at the acute stage showed a striking agreement with the literature (15) and with our theoretical prediction. Assuming deoxyHb is the dominating species in acute hematomas, the measured average susceptibility of 1.30 ppm agreed with the expected value of 1.37 ppm calculated using $\mathrm{Hct} \times \Delta\chi_{\mathrm{do}}$, where the hematocrit value is $\mathrm{Hct} = 0.4$ and fully deoxygenated hemoglobin susceptibility is $\Delta\chi_{\mathrm{do}} = 3.43\mathrm{ppm}$ (15). The observed highly positive susceptibility values in hyperacute hematomas also suggest the presence of deoxyHb, potentially metHb in addition to oxygenated blood. Previously, deoxyHb was regarded as only appearing at the periphery of hyperacute hematoma, indicated by a hypointense rim on T2*w images but without histological confirmation (1,4,13,17,18). We saw neither a hyperintense rim nor a

hypointense center on QSM images of hyperacute hematomas. QSM utilizes the phase information from all voxels surrounding the susceptibility source that act as "field observers" and not only those occupied by the source. In numerical simulations, it has been shown that MEDI is capable of accurately reconstructing the susceptibility of a source even when the magnitude signal is artificially removed (10). It has also been shown that in patients with calcifications (9) and microbleeds (4), a reconstruction of the susceptibility in those lesions is still possible with the correct sign, which is negative and positive using CSF as the reference, respectively. Our finding suggests that the degradation of oxyHb to deoxyHb in ICH may be faster than expected and may not strictly follow a periphery-central path. Indeed, the hypointense rim on T2*w images may be caused by the local field inhomogeneity at the interface between the hematoma with highly positive susceptibility and brain tissue with slightly negative susceptibility. This rapid appearance of deoxyHb in a hyperacute hemorrhage may be explained by the ability of hemoglobin to immediately release oxygen into the extravascular space during conditions of low oxygen concentration.

An immediate clinical application of this finding is to identify rebleeding in ICH, which may appear as isointense on T1w and hyperintense on T2w images, a scenario which is visually similar to conditions of edema. The positive susceptibility values in fresh blood allow clear differentiation between rebleeding and edema, which has zero susceptibility.

The susceptibility decrease from acute to late subacute ICH is unexpected. Theoretically, susceptibility should increase from the acute to subacute stage, because iron in deoxyHb changed from Fe^{2+} (four unpaired electrons, 121ppm·L/mol) to Fe^{3+} in metHb

(five unpaired electrons, 177ppm·L/mol; (19-21). In the blood phantom experiment, we observed a monotonically non-decreasing trend. The measured susceptibility reduction from acute to late subacute hematomas reflects a lower concentration of metHb. This finding may indicate the clearance of metHb by macrophages and the dilution of metHb by interstitial fluid in the hematoma due to high water content of the lysed red blood cells and inflammation (influx of macrophages) at the late subacute stage (13). Erythrocytes, Hb after hemolysis and damaged cell debris are removed quickly by microglia/macrophages from the hematoma in immune response to minimize cytotoxic effects (22). As suggested by our findings, ICH in the late subacute stage has substantially reduced metHb and reduced cellular contents, which are consistent with the observed hyperintensities on both T1w and T2w images. The residual metHb is highly mobile and can still cause enhancement of 1/T1 and 1/T2, markedly shortening T1 but only marginally shortening T2 (which is typically much shorter than T1 in contrast enhanced MRI). The hematoma fluid dilution of metHb if substantial may be detected by longitudinal monitoring of the hematoma volume change during acute and late subacute stages. Assuming that the volume is stabilized in the late subacute stage, our finding suggests active metHb clearance.

The significant increase in susceptibility (0.31ppm) was found in chronic stage ICH relative to that in the late subacute stage. This susceptibility increase might be caused by the degradation of blood products such as small magnetic domain formation in hemosiderin, as well as edema resolution, particularly if the hematoma volume on T2w decreases because this would lead to an increase in iron concentration. The removal of metHb by

microglia/macrophages seems to have stopped after the late subacute stage, allowing for the resolution of the remaining metHb into final stable hemosiderin.

Despite the lower inner structure contrast of ICH and longer scan time (6 minutes) when compared to T1 and T2 weighted images, QSM provided quantitative susceptibility measurements of ICH, which have the potential to be converted into concentrations of different blood products using molar susceptibilities of blood iron products (dHb, metHb, etc.). This feature allows for better understanding of ICH pathophysiology and may be a promising monitoring tool in drug trials and in the clinical setting. In addition, since QSM images are calculated from magnitude and phase data that was acquired using a gradient echo (GRE) sequence (from which both T2* weighted and susceptibility weighted images (SWI) can be generated), QSM does not require the addition of a specialized sequence to the standard ICH MRI protocol.

In this study, a major limitation consists of uneven sampling density over various stages of ICH, especially for the hyperacute stage, and the lack of longitudinally serial imaging. Compared to MR, CT is currently preferred for imaging ICH in the hyperacute stage because of shorter scan time and better availability. After CT scans, patients are often not stable enough for immediate MRI follow ups within 24hr before hyperacute hematomas progress to acute stage. Both of these factors led to small sample size in the hyperacute stage. A second limitation of this study is its cross-sectional design. This design was chosen because it was relatively difficult to get consent for longitudinal MRI follow up after acute

ICH. A third limitation is the lack of histological validation. This issue can be addressed through follow up studies of hematoma susceptibility in animal models.

3.6 CONCLUSION

QSM reveals positive susceptibility relative to CSF in hyperacute hematomas, indicating the existence of deoxyhemoglobin even in the hyperacute stage. QSM also reveals a significant reduction of susceptibility from acute to late subacute ICH, suggesting a decrease in methemoglobin concentration in the late subacute stage.

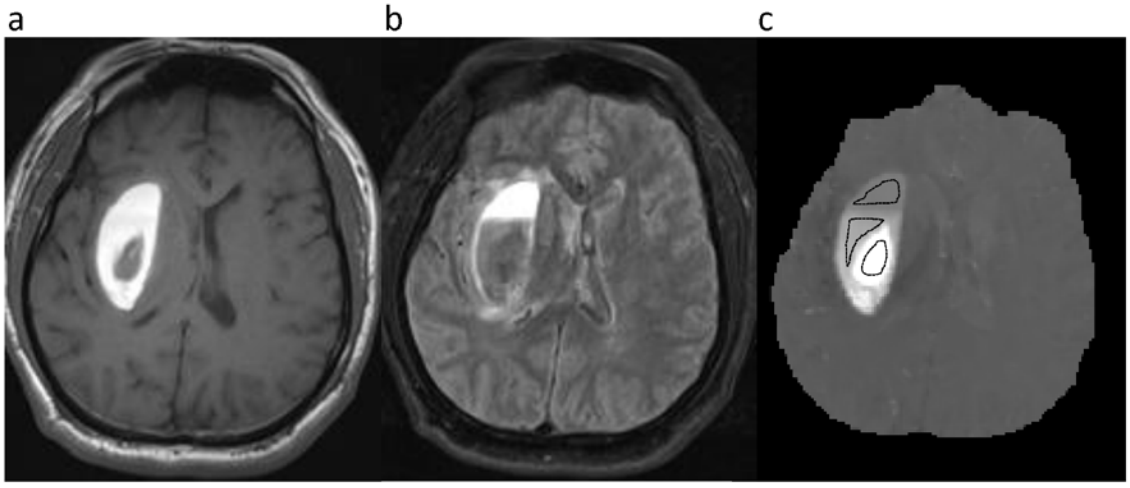

Figure 3.1. Illustration of the quantitative susceptibility measurement of various blood products. The hyperintense rim on both T1w (a) and T2w (b) images suggested extracellular met-hemoglobin at the periphery of the hematoma. The iso-intense core on the T1w image and the corresponding hypointensity on T2w suggested the presence of deoxy-hemoglobin in the center. The upper half of the hematoma showed hyperintensity in both T1w and T2w images, suggesting extracelluar methemoglobin. The rest of the hematoma showed hyperintensity on T1w and hypointensity on T2w images, suggesting intracellular methemoglobin. Accordingly, susceptibility values measured in these regions are shown as ROIs on QSM (c).

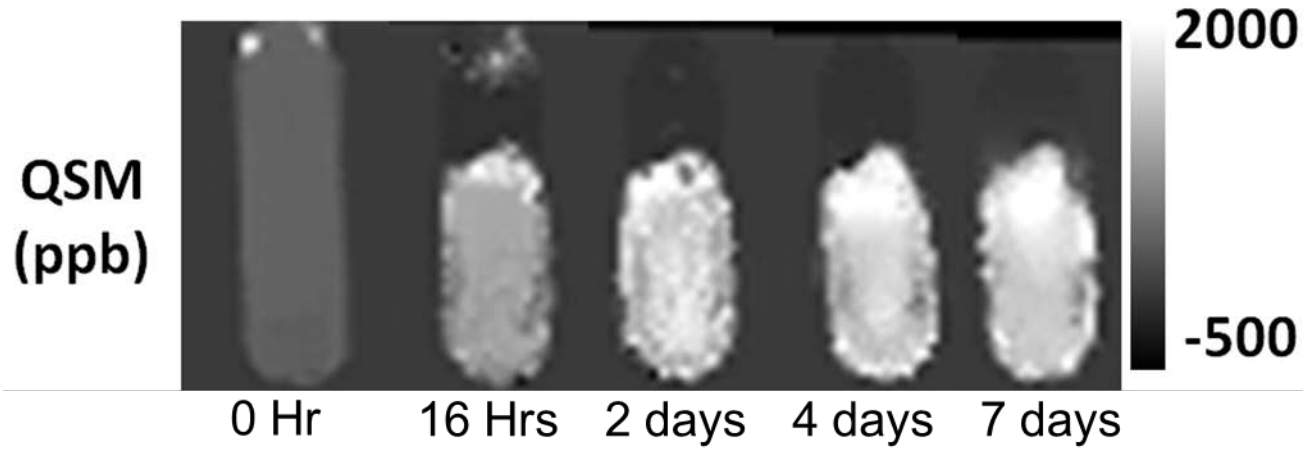

Figure 3.2. QSM of blood phantom over time.

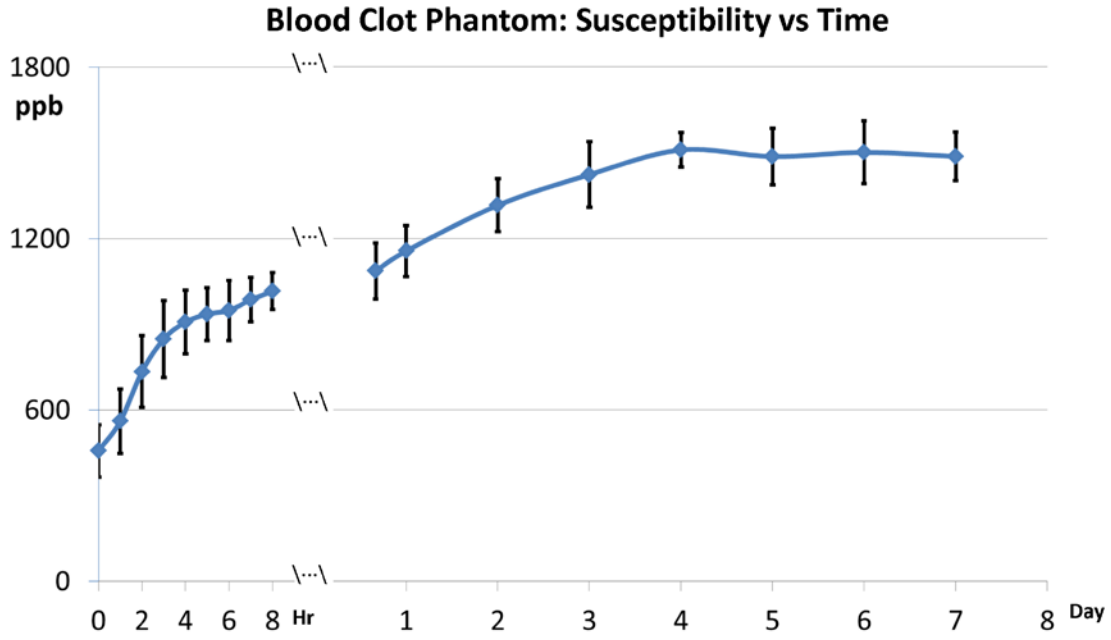

Figure 3.3. Susceptibility values of blood clot phantom and corresponding time points, demonstrating an increase in susceptibility in the first 4 days, followed by a plateau.

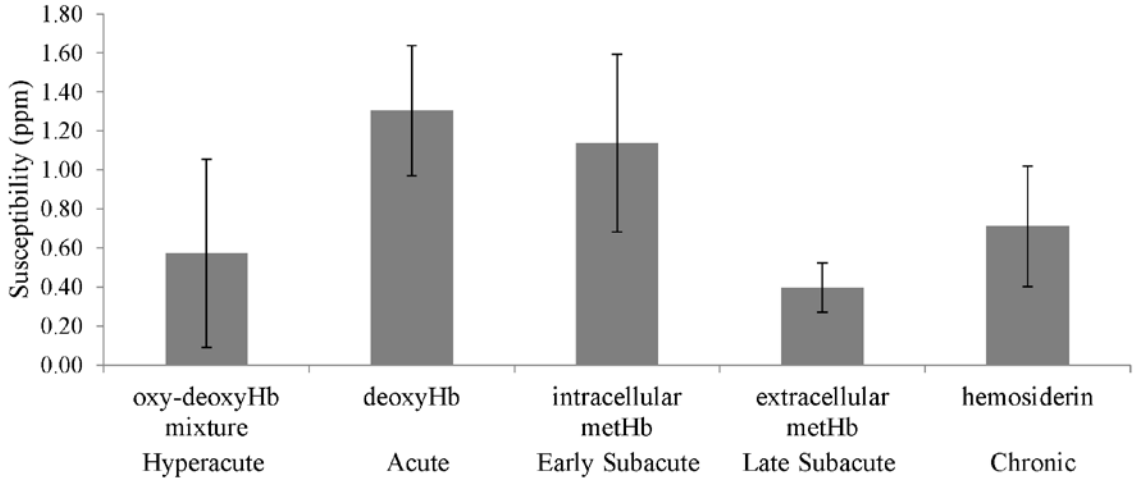

Figure 3.4. Susceptibility values of intracerebral hematomas at various stages and corresponding blood products, demonstrating positive susceptibility at the hyperacute stage, followed by a significant increase at the acute stage from hyperacute, a significant decrease in the late subacute stage from early subacute, and an eventual significant increase at the chronic stage.

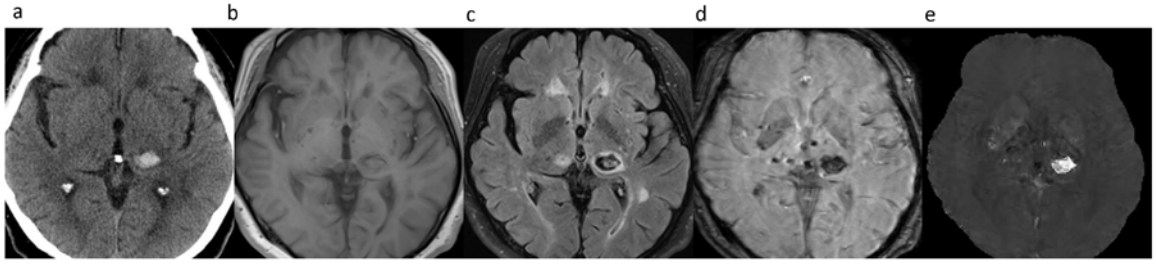

Figure 3.5. Hyperacute ICH in a 61 year old male with MRI obtained 6 hours after symptom onset and a follow up CT performed 20 minutes later. a) CT, b)T1w, c)T2w-FLAIR, d)T2*w and e)QSM. T2w Flair (c) and T2*w (d) reveal a hypointense rim and an

isointense to hypointense core typical for hyperacute ICH. QSM (e) shows a relatively isointense rim, especially in the medial part of the lesion, which suggests that the hypointense rim seen on T2w Flair and T2*w images may be susceptibility artifacts at the core of the hematoma. The core on QSM is hyperintense suggesting a mixture of oxy and deoxy Hb. This hyperacute ICH shows a high susceptibility value of 1.32ppm.

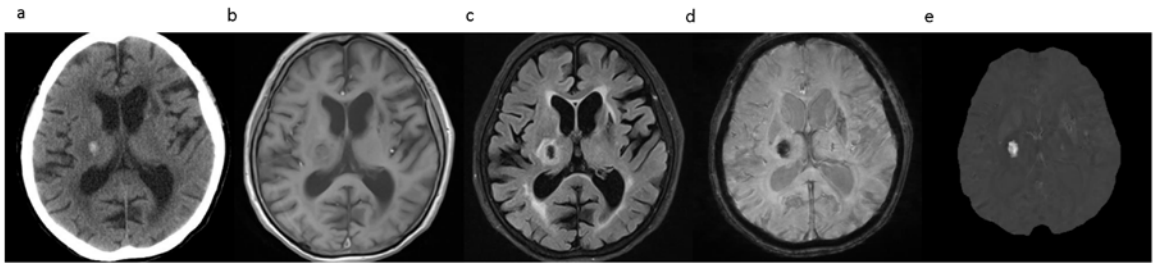

Figure 3.6. An acute ICH is shown on a)CT, b)T1w, c)T2w-FLAIR, d)T2*w and e)QSM images. CT (a) shows a hyperdense lesion in the right thalamus, T1w (b) shows an isointense core, T2w-FLAIR (c) and T2*w (d) both show a hypointense core, and QSM shows a hyperintense core.

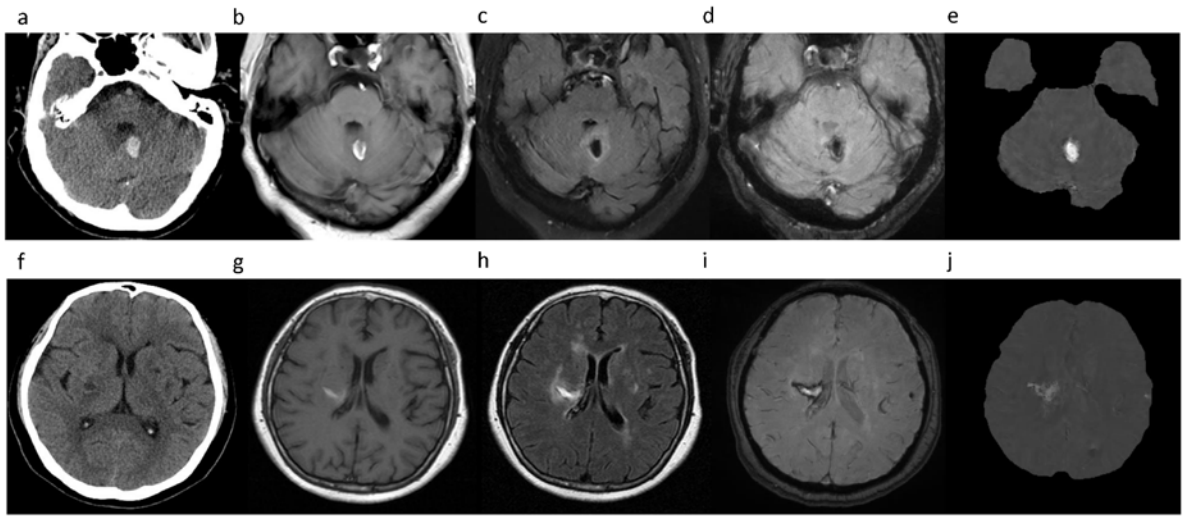

Figure 3.7. An early subacute ICH is shown on a)CT, b)T1w, c)T2w-FLAIR, d)T2*w and e)QSM images, demonstrating a hyperintense periphery with an isointense core on T1w (b) but with the appearance of hypointensity on both on T2w-FLAIR (c), T2*w (d) and hyperintense on QSM (e). A late subacute ICH is shown on f) CT, g)T1w, h)T2w-FLAIR, i)T2*w and j)QSM, demonstrating a hyperintense core on all MRI images (g-j). This late subacute ICH has a low susceptibility value of 0.44ppm.

REFERENCES

1. Atlas S, Thulborn K. Magnetic resonance imaging of the brain and spine. 3rd ed. Philadelphia: Lippincott Williams & Wilkins. Intracranial hemorrhage 2002:773-832.

2. Kidwell CS, Wintermark M. Imaging of intracranial haemorrhage. Lancet neurology 2008;7(3):256-267.

3. de Rochefort L, Liu T, Kressler B, et al. Quantitative susceptibility map reconstruction from MR phase data using bayesian regularization: validation and application to brain imaging. Magnetic resonance in medicine : official journal of the Society of Magnetic Resonance in Medicine / Society of Magnetic Resonance in Medicine 2010;63(1):194-206.

4. Liu T, Surapaneni K, Lou M, Cheng L, Spincemaille P, Wang Y. Cerebral microbleeds: burden assessment by using quantitative susceptibility mapping. Radiology 2012;262(1):269-278.

5. Wang S, Lou M, Liu T, Cui D, Chen X, Wang Y. Hematoma volume measurement in gradient echo MRI using quantitative susceptibility mapping. Stroke 2013;44(8):2315-2317.

6. Mikati AG, Tan H, Shenkar R, et al. Dynamic permeability and quantitative susceptibility: related imaging biomarkers in cerebral cavernous malformations. Stroke 2014;45(2):598-601.

7. Tan H, Liu T, Wu Y, et al. Evaluation of Iron Content in Human Cerebral Cavernous Malformation Using Quantitative Susceptibility Mapping. Invest Radiol 2014.

8. Deistung A, Schweser F, Wiestler B, et al. Quantitative susceptibility mapping differentiates between blood depositions and calcifications in patients with glioblastoma. PLoS One 2013;8(3):e57924.

9. Chen W, Zhu W, Kovanlikaya I, et al. Intracranial calcifications and hemorrhages: characterization with quantitative susceptibility mapping. Radiology 2014;270(2):496-505.

10. Liu J, Liu T, de Rochefort L, et al. Morphology enabled dipole inversion for quantitative susceptibility mapping using structural consistency between the magnitude image and the susceptibility map. NeuroImage 2012;59(3):2560-2568.

11. Liu T, Wisnieff C, Lou M, Chen W, Spincemaille P, Wang Y. Nonlinear formulation of the magnetic field to source relationship for robust quantitative susceptibility mapping. Magnetic resonance in medicine : official journal of the Society of Magnetic Resonance in Medicine / Society of Magnetic Resonance in Medicine 2013;69(2):467-476.

12. Liu T, Liu J, de Rochefort L, et al. Morphology enabled dipole inversion (MEDI) from a single-angle acquisition: comparison with COSMOS in human brain imaging. Magn Reson Med 2011;66(3):777-783.

13. Bradley WG, Jr. MR appearance of hemorrhage in the brain. Radiology 1993;189(1):15-26.

14. Gonen M, Panageas KS, Larson SM. Statistical issues in analysis of diagnostic imaging experiments with multiple observations per patient. Radiology 2001;221(3):763-767.

15. Jain V, Abdulmalik O, Propert KJ, Wehrli FW. Investigating the magnetic susceptibility properties of fresh human blood for noninvasive oxygen saturation quantification. Magn Reson Med 2012;68(3):863-867.

16. Zhang J, Liu T, Gupta A, Spincemaille P, Nguyen TD, Wang Y. Quantitative mapping of cerebral metabolic rate of oxygen (CMRO) using quantitative susceptibility mapping (QSM). Magnetic resonance in medicine : official journal of the Society of Magnetic Resonance in Medicine / Society of Magnetic Resonance in Medicine 2014.

17. Fobben ES, Grossman RI, Atlas SW, et al. MR characteristics of subdural hematomas and hygromas at 1.5 T. AJR Am J Roentgenol 1989;153(3):589-595.

18. Gomori JM, Grossman RI, Goldberg HI, Zimmerman RA, Bilaniuk LT. Intracranial hematomas: imaging by high-field MR. Radiology 1985;157(1):87-93.

19. Bradley WG, Jr., Schmidt PG. Effect of methemoglobin formation on the MR appearance of subarachnoid hemorrhage. Radiology 1985;156(1):99-103.

20. Gomori JM, Grossman RI. Mechanisms responsible for the MR appearance and evolution of intracranial hemorrhage. Radiographics : a review publication of the Radiological Society of North America, Inc 1988;8(3):427-440.

21. Wang Y. Magnetic Susceptibility of Biomaterials. Quantitative Susceptibility Mapping: Magnetic Resonance Imaging of Tissue Magnetism. Createspace Independent Pub; 2013. p. p.22-24.

22. Aronowski J, Zhao X. Molecular pathophysiology of cerebral hemorrhage: secondary brain injury. Stroke; a journal of cerebral circulation 2011;42(6):1781-1786.

Chapter 4

Quantitative $CMRO_2$ and OEF Mapping with QSM and ASL

4.1 ABSTRACT

Purpose

To quantitatively map cerebral metabolic rate of oxygen ($CMRO_2$) and oxygen extraction fraction (OEF) in human brains using quantitative susceptibility mapping (QSM) and arterial spin labeling measured cerebral blood flow (CBF) before and after caffeine vasoconstriction.

Methods

Using the multiecho 3D gradient echo sequence and an oral bolus of 200 mg caffeine, whole brain $CMRO_2$ and OEF were mapped at 3mm isotropic resolution on 13 healthy subjects. The QSM based $CMRO_2$ was compared with an R_2^* based $CMRO_2$ to analyze the regional consistency within cortical gray matter (CGM) with the scaling in the R_2^* method set to provide same total $CMRO_2$ as the QSM method for each subject.

Results

Compared to pre-caffeine, susceptibility increased (5.1±1.1ppb, $p<0.01$) and CBF decreased (-23.6±6.7ml/100g/min, $p<0.01$) at 25min post-caffeine in CGM. This corresponded to a $CMRO_2$ of 153.0±26.4μmol/100g/min with an OEF of 33.9±9.6% and 54.5±13.2% ($p<0.01$) pre- and post- caffeine respectively at CGM, and a $CMRO_2$ of 58.0±26.6μmol/100g/min at white matter. $CMRO_2$ from both QSM and R_2^* based methods showed good regional consistency ($p>0.05$), but quantitation of R_2^* based $CMRO_2$ required an additional scaling factor.

Conclusion

QSM can be used with perfusion measurements pre- and post- caffeine vascoconstriction to map $CMRO_2$ and OEF.

4.2 INTRODUCTION: CLINICAL CHALLENGES AND PRIOR WORK

The cerebral metabolic rate of oxygen ($CMRO_2$) and the oxygen extraction fraction (OEF) are important markers for assessing neuronal viability in ischemic stroke when hypoperfusion leads to a compensatory OEF increase to maintain oxygen metabolism before the onset of brain tissue infarction (1-3). Positron emission tomography (PET) using ^{15}O has been used to map $CMRO_2$, but its feasibility as a clinical tool is severely limited by the short half-life (123 sec) of ^{15}O (4) and sparse availability compared to other imaging modalities like MRI.

When oxygen is released from arterial blood to brain tissue, the weakly diamagnetic oxyhemoglobin (oHb) turns into to the strongly paramagnetic deoxyhemoglobin (dHb) in the draining veins (5). MRI is very sensitive to this change in magnetic susceptibility. Changes in R_2 (estimated from spin echo data) and R_2^* (estimated from gradient echo (GRE) data) by the magnetic field of dHb have been used to estimate dHb concentration ([dHb]) (6-11). As R_2^* is more sensitive than R_2 (12), R_2^* is more commonly used (13-15). However, R_2^* images are contaminated by blooming artifacts and are highly dependent on imaging parameters including field strength, echo time, voxel size, and object orientation (6,16), making it difficult to quantitatively map [dHb].

Because [dHb] is linearly related to blood magnetic susceptibility that is independent of imaging parameters (17,18), quantitative susceptibility mapping (QSM) derived from the magnitude and phase of the GRE signal (19-35) has the potential for quantitative [dHb] measurements. QSM may provide an advantage over the previous

approaches by eliminating the blood vessel geometry dependence in estimating [dHb] in veins only (36-40). Here, we demonstrate the feasibility of $\mathrm{CMRO_2}$ mapping using QSM and cerebral perfusion measurements.

4.3 SUSCEPTIBILITY MODELING OF TISSUE AND BLOOD

According to mass conservation, we have,

$$\mathrm{CMRO_2} = 4\mathrm{CBF} \cdot ([\mathrm{dHb}]_\mathrm{v} - [\mathrm{dHb}]_\mathrm{a}) \qquad [4.1]$$

Here CBF is the volumetric cerebral blood flow rate, and $[\mathrm{dHb}]_\mathrm{v}$ and $[\mathrm{dHb}]_\mathrm{a}$ are [dHb] in the draining veins and supplying arteries respectively. The factor 4 accounts for the four oxygen molecules in one oHb, each bound to one of four hemes. CBF can be measured using a quantitative perfusion technique such as arterial spin labeling (ASL) (41). The arterial dHb concentration can be written as $[\mathrm{dHb}]_\mathrm{a} = (1 - \mathrm{SaO_2})[\mathrm{Hb}]$ with arterial oxygen saturation $\mathrm{SaO_2} = 0.97$ and hemoglobin concentration $[\mathrm{Hb}] = 2.48\mu\mathrm{mol/ml}$ for healthy subjects (see Appendix). $[\mathrm{dHb}]_\mathrm{v}$ can be derived using QSM in the following manner by carefully accounting for contributions from various components in blood and non-blood tissue weighted by the respective volume fractions, though the dominant contributions are from venous dHb and tissue ferritin.

The voxel susceptibility, χ, in QSM is linearly proportional to $[\mathrm{dHb}]_\mathrm{v}$,

$$\chi = \mathrm{CBV_v} \cdot \Psi_{\mathrm{Hb}}(\mathrm{X_{dHb}} - \mathrm{X_{oHb}}) \frac{[\mathrm{dHb}]_\mathrm{v}}{[\mathrm{Hb}]} + \chi_\mathrm{o}. \qquad [4.2]$$

Here $\mathrm{CBV_v} = 0.5\mathrm{CBV}$ is the venous blood volume fraction in a voxel assuming blood deoxygenates linearly (10). $\Psi_{\mathrm{Hb}} = 0.12$ is the volume fraction of Hb within blood (see Appendix). $\mathrm{X_{dHb}} = 10765\mathrm{ppb}$ and $\mathrm{X_{oHb}} = -813\mathrm{ppb}$ are the volume susceptibilities of pure dHb and oHb respectively (see Appendix). The first term in the right hand side of Eq. 4.2 reflects the susceptibility contribution from venous dHb relative to oxygenated blood. The second term χ_o in Eq. 4.2 reflects susceptibility contributions from non-blood tissue sources (such as ferritin) χ_t, pure oxygenated blood $\mathrm{X_{ba}}$, and arterial deoxyhemoglobin:

$$\chi_\mathrm{o} = (1 - \mathrm{CBV})\chi_\mathrm{t} + \mathrm{CBV} \cdot \mathrm{X_{ba}} + \mathrm{CBV_a} \cdot \Psi_{\mathrm{Hb}}(\mathrm{X_{dHb}} - \mathrm{X_{oHb}}) \frac{[\mathrm{dHb}]_\mathrm{a}}{[\mathrm{Hb}]}, \qquad [4.3]$$

with $\mathrm{CBV_a} = 1 - \mathrm{CBV_v} = 0.5\mathrm{CBV}$, and $\mathrm{X_{ba}} = \Psi_{\mathrm{Hb}} \cdot \mathrm{X_{oHb}} + (1 - \Psi_{\mathrm{Hb}})\mathrm{X_p} = -131\mathrm{ppb}$ is the volume susceptibility for pure oxygenated blood ($\mathrm{X_p} = -37.7\mathrm{ppb}$ is blood plasma volume susceptibility) (18,39,42).

With susceptibility (χ) and perfusion (CBV and CBF) measurements, Eqs.1&2 form an equation with two unknowns ($\mathrm{CMRO_2}$ and χ_o):

$$\mathrm{CMRO_2} = 4\mathrm{CBF} \cdot [\mathrm{Hb}] \left(\frac{\chi - \chi_\mathrm{o}}{\mathrm{CBV_v} \cdot \Psi_{\mathrm{Hb}}(\mathrm{X_{dHb}} - \mathrm{X_{oHb}})} - (1 - \mathrm{SaO_2}) \right). \qquad [4.4]$$

To determine $\mathrm{CMRO_2}$, it is necessary to correct for χ_t, which is independent of blood. This can be achieved using measurements at two different brain perfusion states that have the same $\mathrm{CMRO_2}$, such as before and after vasoconstriction in a caffeine challenge (43-45). It

is reasonable to assume the non-blood contribution $(1 - \mathrm{CBV})\chi_t$ to susceptibility in a voxel to be the same between the two states. Then Eq. 4.4 leads to

$$\mathrm{CMRO_2} = \frac{4[\mathrm{Hb}]}{\Delta(\mathrm{CBV_v}/\mathrm{CBF})}\left(\frac{\Delta\chi - \Delta\chi_0}{\Psi_{\mathrm{Hb}}(\mathrm{X_{dHb}} - \mathrm{X_{oHb}})} - \Delta\mathrm{CBV_v}(1 - \mathrm{SaO_2})\right) \quad [4.5]$$

where Δ denotes the difference between the two measurements (see Appendix for a detailed derivation of Eq. 4.5 from Eq. 4.4).

OEF is defined as the oxygen concentration difference between artery and vein scaled by the arterial oxygen concentration ($4 * \mathrm{SaO_2}[\mathrm{Hb}] = 4 * 0.97[\mathrm{Hb}]$) can then be determined as

$$\mathrm{OEF} = \frac{\mathrm{CMRO_2}}{4 \cdot \mathrm{SaO_2} \cdot [\mathrm{Hb}] \cdot \mathrm{CBF}} \quad [4.6]$$

4.4 EXPERIMENTS AND ANALYSIS

The study was approved by the local Institutional Review Board. Healthy volunteers were recruited (n=13, 13 males, mean age 35 ± 9.5 years) for brain MRI on a 3T scanner (HDxt, GE Healthcare, Waukesha, WI, USA) using an 8-channel receive head coil. All subjects were instructed to avoid caffeine or alcohol intake 24 hours prior to MRI.

4.4.1 Data Acquisition

Given its well-described ability to safely cause measurable reductions in CBF within 30 minutes upon administration (45), a bolus of caffeine (~200 mg caffeine in black coffee) was administered orally through a flexible plastic tube to minimize head motion. MRI was performed before and 25 min after the oral administration of the caffeine challenge, using a protocol consisting of an anatomical T2 weighted 2D fast spin echo (FSE) sequence, a 3D FSE ASL sequence to measure CBF, and a 3D spoiled GRE sequence to measure magnitude and phase, from which QSM maps were calculated using dipole inversion algorithm (19,21). The total scan time was approximately 60 min (consisting of 15 min scan before caffeine administration to 45 min after).

The T2 weighted axial 2D FSE parameters were: 82 ms TE, 4250 ms TR, 22 cm FOV, 0.46 x 0.46 mm^2 in-plane resolution, 3mm slice thickness, 46 slices, 23 echo train length (ETL), 2 signal averages, and 5 min scan time.

The 3D FSE ASL sequence parameters were: 1500 ms labeling period, 1525 ms post-label delay, spiral sampling of 8 interleaves with 512 readout points per leaf, 62.5 kHz readout bandwidth, 1 ETL, 3 mm isotropic resolution and identical volume coverage as the T2 weighted sequence, 10.5 ms TE, 4796 ms TR, 3 signal averages, and 6 min scan time. CBF maps (ml/100g/min) were generated from the ASL data using the FuncTool software package (GE Healthcare, Waukesha, WI, USA).

The 3D spoiled GRE sequence parameters included: 11 equally spaced echoes, 4.4 ms first TE, 4.9 ms echo spacing , 58.5 ms TR, 0.46 mm in-plane resolution, 3 mm slice thickness, and identical volume coverage as the T2 weighted sequence, 62.5 kHz readout bandwidth, 15^{o} flip angle, and 7 min scan time. The pulse sequence was flow-compensated in the readout (anterior-posterior) direction.

4.4.2 Image Processing

QSM maps were calculated from GRE magnitude and phase data. A Gauss-Newton nonlinear estimation of the field map was performed (33), followed by unwrapping (46) and background field removal using a projection onto dipole fields method (47) to obtain the local field map, from which tissue susceptibility was computed using the Morphology Enabled Dipole Inversion (MEDI) algorithm (20,33). R_2^* maps were generated from GRE magnitude data via voxel-by-voxel fitting using auto-regression on linear operations (ARLO) monoexponential fitting algorithm (48). Signal-to-noise ratio (SNR) of QSM and

R_2^* maps were estimated as the ratio of mean over standard deviation of values measured in the caudate nucleus.

Grey matter (GM) and white matter (WM) masks were created using the FSL FAST algorithm on pre-caffeine CBF images covering the supratentorial brain parenchyma from the vertex to the superior aspect of the cerebellum (49). These masks were visually confirmed by a board-certified attending neuroradiologist (A.G.) for anatomical accuracy. The cortical GM mask was further segmented by the same neuroradiologist into six vascular territories (VT, left and right anterior cerebral artery (ACA), middle cerebral artery (MCA) and posterior cerebral artery (PCA)) (Fig. 4.1). For this feasibility study, pre-caffeine CBV was estimated from CBF based on the linear regression equations derived from ^{15}O steady-state inhalation PET (50): $\mathrm{CBV} = (0.227\mathrm{CBF} - 7.27)/100$ within the GM mask, and $\mathrm{CBV} = (0.0316\mathrm{CBF} + 1.9447)/100$ within the WM mask. Post-caffeine CBV was estimated from pre-caffeine CBV using Grubb's exponent of $\alpha = 0.38$ (51) for both masks. $\mathrm{CMRO_2}$ maps of GM and WM were then calculated from pre- and post-caffeine QSM and $\mathrm{CBF/CBV}$ measurements by solving Eq. 4.4 using a conjugate gradient method. The resulting maps were combined to obtain the final $\mathrm{CMRO_2}$ maps of the whole brain. OEF maps were then calculated using Eq. 4.8. Gaussian smoothing (2.1 mm kernel) was used to reduce noise in the $\mathrm{CMRO_2}$ and OEF maps.

All images were co-registered and interpolated to the resolution of the CBF maps using the FSL FLIRT algorithm (52,53). QSM values were referenced to the susceptibility

of water (defined in this study as the mean susceptibility of cerebrospinal fluid (CSF) in the lateral ventricles).

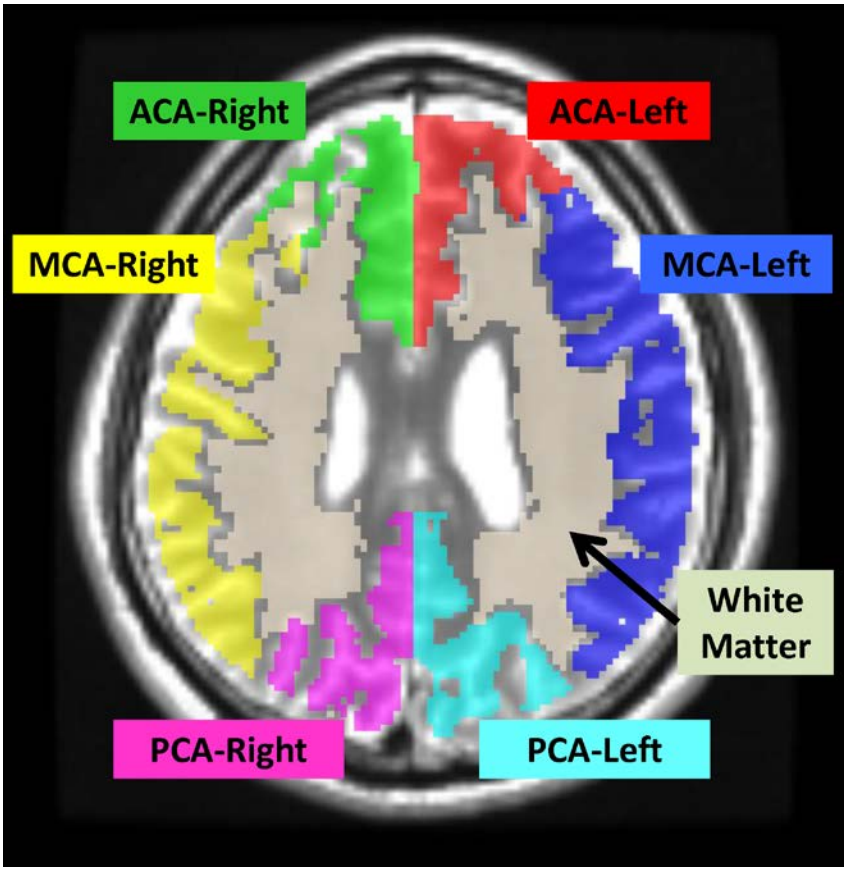

Figure 4.1. Example of GM and WM masks on a mid-brain slice. The GM mask is segmented into six regions corresponding to different vascular territories as shown. The masks cover the supratentorial brain parenchyma from the vertex to the superior aspect of the cerebellum.

$CMRO_2$ was also estimated using a calibrated fMRI approach based on R_2^* (13-15). The difference in R_2^* between pre- and post- caffeine challenge can be used to estimate the dHb component of R_2^* in a voxel during pre-caffeine state ($R_2^*|_{dHb,pre}$) according to the following equation with Grubb's $\alpha = 0.38$ and an empirical $\beta = 1.5$ (54).

$$R_{2,pre}^* - R_{2,post}^* = R_2^*|_{dHb,pre}\left(1 - \left(\frac{CBF_{post}}{CBF_{pre}}\right)^{\alpha-\beta}\right). \quad [7]$$

Then the relationship between $R_2^*|_{dHb,pre}$ and pre-caffeine venous dHb concentration $[dHb]_{v,pre}$ is given as follow (7,8,11,54,55):

$$R_2^*|_{dHb,pre} = A \cdot CBV_{pre}[dHb]_{v,pre}^{\beta} \quad [8]$$

Combining Eqs.7&8 with Eq. 4.1 and using $[dHb]_a \approx 0$ and $(\frac{CBF_{post}}{CBF_{pre}})^{\alpha} = \frac{CBV_{post}}{CBV_{pre}}$, we have

$$CMRO_2 = 4A^{-1/\beta} \cdot CBF_{pre}CBF_{post}\left(\frac{R_{2,post}^* - R_{2,pre}^*}{CBV_{post}CBF_{pre}^{\beta} - CBV_{pre}CBF_{post}^{\beta}}\right)^{1/\beta}. \quad [9]$$

This R_2^* based $CMRO_2$ method requires the scaling factor A to be measured separately with an additional measurement at a different brain state (13-15). For this feasibility study, the regional consistency of $CMRO_2$ maps within cortical GM ROIs (Fig. 4.1) derived from QSM and R_2^* based methods was compared under the assumption that their global averages or total $CMRO_2$ were the same for each subject, which allowed A to be determined from the QSM data without further experiment.

4.4.3 Statistical Analysis

For each ROI, the mean and standard deviation of QSM, CBF, OEF, and $CMRO_2$ values as well as the corresponding left/right (L/R) hemisphere ratio were measured for both the QSM based and R_2^* based method. Paired-sample t-tests were performed to assess the differences in QSM, R_2^*, CBF, and OEF in the GM ROIs before and after the caffeine challenge across the subjects. PET studies have shown that $CMRO_2$ and OEF maps are homogeneous in GM across the brain and exhibit left-right symmetry in healthy subjects (50,56). Paired-sample t-tests were performed to compare $CMRO_2$ in the VT ROIs between QSM based and R_2^* based method to analyze their consistency. To analyze the symmetry of the images, analysis of variance (ANOVA) was performed to assess the significance of differences in L/R hemisphere ratio of $CMRO_2$ and OEF among the VT ROIs. P values of less than 0.05 were considered to indicate statistical significance. All data were expressed as mean ± standard deviation.

4.5 RESULTS

All scans were completed successfully. The average GM volume for each vascular territory was 125.8 ± 17.7 mL (ACA, both left and right), 254.0 ± 25.4 mL (MCA), and 79.7 ± 14.2 mL (PCA) (n=13). Figure 4.2 shows an example of pre- and post-caffeine QSM and CBF maps and the calculated $CMRO_2$ and OEF maps. QSM and R_2^* maps have similar SNR (6.2 ± 1.9 vs. 7.2 ± 1.6, p>0.05). Figure 4.3 shows OEF and $CMRO_2$ maps across the brain volume, illustrating good GM and white matter contrast in reasonable agreement with T2 weighted images. Compared to the pre-caffeine values, a statistically significant increase in QSM (5.1 ± 1.1 ppb, p<0.01), R_2^* (1.5 ± 0.3 s^{-1}, p<0.01), and decrease in CBF (-23.6 ± 6.7 ml/100g/min, p<0.01) were measured in the global cortical GM ROI at 25 min post-caffeine. Consistent with the decrease in CBF after the caffeine challenge, OEF significantly increased from 33.9 ± 9.6% to 54.5 ± 13.2% (p<0.01) at 25 min post-caffeine. The mean $CMRO_2$ in the global cortical GM ROI calculated using QSM were 153.0 ± 26.4 μmol/100g/min. The mean $CMRO_2$, and pre- and post-caffeine OEF measured in the WM were 58.0 ± 26.6 μmol/100g/min, 26.3 ± 11.7% and 45.0 ± 18.7%, respectively.

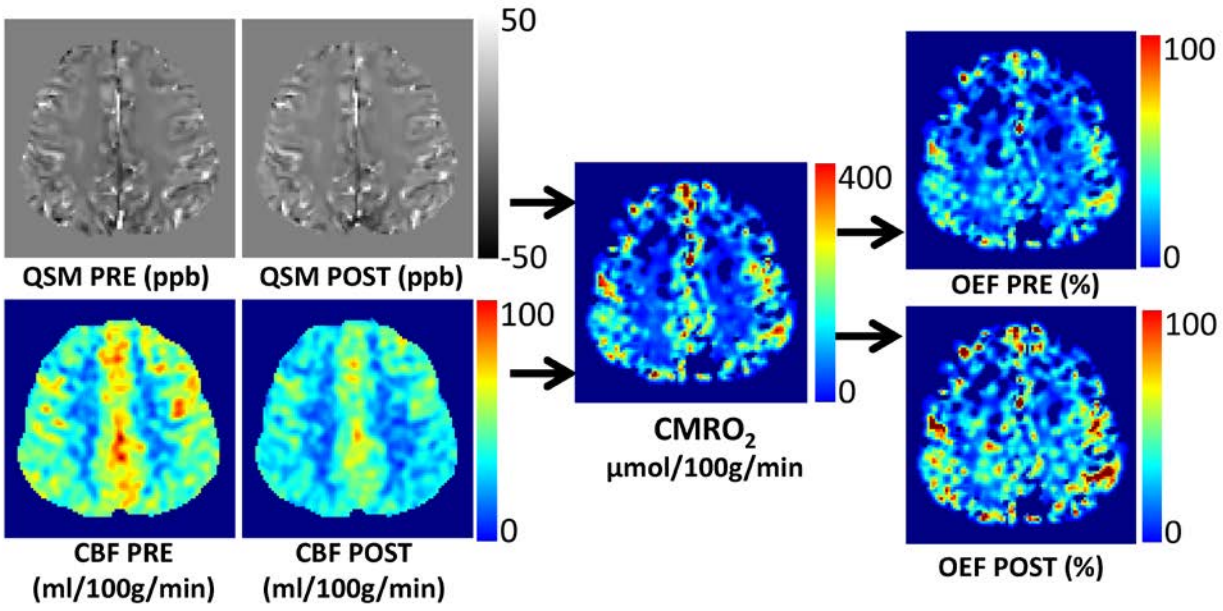

Figure 4.2. An example of QSM and CBF maps acquired pre- and post-caffeine and the derived $CMRO_2$ and OEF maps in a healthy subject (subject 12).

Figure 4.4 compares $CMRO_2$ maps obtained from two other subjects using QSM-based and R_2^*-based methods. The mean $R_2^*|_{dHb,pre}$ in the global cortical GM ROI was 1.9 ± 0.8 s^{-1}. Table 4.1 shows the $CMRO_2$ measured within VT ROIs of QSM based and R_2^* based methods, demonstrating good agreement within all vascular territories (all differences were statistically non-significant). Table 4.2 shows the L/R hemisphere ratio of $CMRO_2$ and OEF measured within the VT ROIs. Both the QSM and R_2^* method show statistically comparable L/R hemisphere ratio values among vascular territories ranging from 0.92 to 1.07, indicating good hemispheric symmetry. (ANOVA, $p > 0.05$).

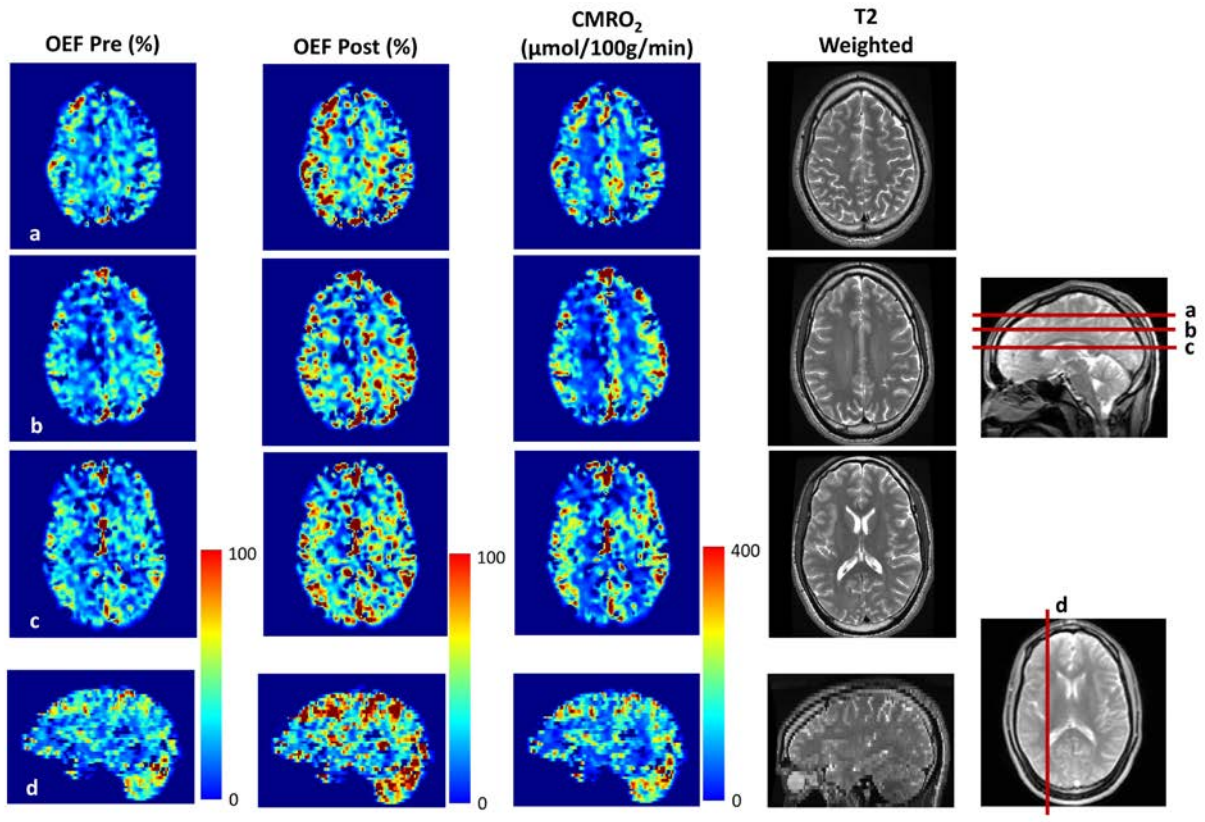

Figure 4.3. An example of volumetric pre- and post-caffeine OEF and $CMRO_2$ maps using the QSM-based method, and T_2 weighted images of a healthy subject (subject 7). The locations of the slices are marked on the scout images shown on the right.

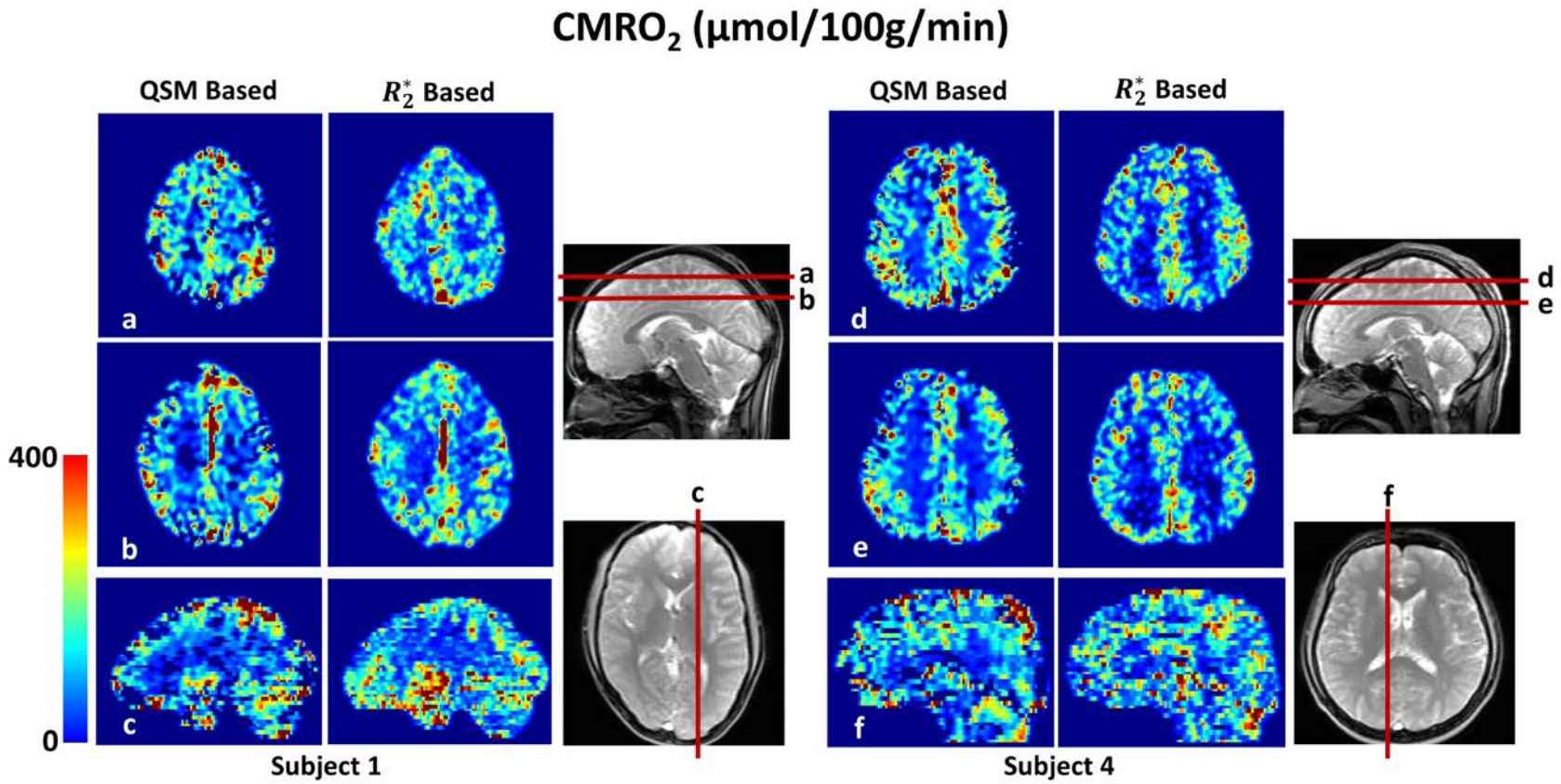

Figure 4.4. Examples of QSM- and R_2* -based $CMRO_2$ maps of two representative subjects (subject 1 and 4). The locations of the slices are marked on the scout images.

Table 4.1: QSM and R_2^* based $CMRO_2$ measurements within cortical GM regions associated with different vascular territories (μmol/100g/min, mean ± std). All differences between the two methods were statistically non-significant ($p>0.05$).

	QSM based	R_2^* based
ACA_Left	175.5 ± 33.4	166.2 ± 29.9
ACA_Right	174.1 ± 33.6	160.6 ± 29.5
MCA_Left	149.3 ± 27.1	153.2 ± 42.1
MCA_Right	154.8 ± 37.7	144.8 ± 33.6
PCA_Left	143.9 ± 38.0	159.1 ± 39.8
PCA_Right	140.8 ± 32.8	157.0 ± 38.3

Table 4.2: L/R hemisphere ratio of QSM and R_2^* based $CMRO_2$ and OEF values measured within cortical GM regions. No statistical significance has been found ($p>0.05$) among vascular territory within each method.

	OEF Pre-Caffeine		OEF Post-Caffeine		$CMRO_2$	
	QSM based	R_2* based	QSM based	R_2* based	QSM based	R_2* based
ACA	0.99 ± 0.12	1.00 ± 0.13	0.99 ± 0.13	1.02 ± 0.15	1.03 ± 0.21	1.04 ± 0.15
MCA	0.99 ± 0.25	0.99 ± 0.23	0.97 ± 0.24	0.97 ± 0.26	1.00 ± 0.22	1.07 ± 0.23
PCA	0.94 ± 0.13	0.96 ± 0.19	0.92 ± 0.13	0.92 ± 0.15	1.03 ± 0.15	1.03 ± 0.23

4.6 DISCUSSION

Our preliminary results demonstrate the in vivo feasibility of 3D $CMRO_2$ brain mapping using the recently developed QSM and quantitative perfusion. The QSM based $CMRO_2$ of 153.0 ± 26.4 μmol/100g/min in cortical GM agrees well with values reported in the MRI and PET literature (13-15,50,56). The QSM based $CMRO_2$ is consistent with the R_2^* based $CMRO_2$ (our mean $R_2^*|_{dHb,pre}$ of 1.9 ± 0.8 s^{-1} is in agreement with values in calibrated fMRI literature (13,57-60)). Using measurements at two different brain states (pre- and post- caffeine challenge here), the QSM based $CMRO_2$ method can provide absolute quantitation while the R_2^* based $CMRO_2$ method relies on the additional measurement of a scaling factor.

The R_2^* model for blood oxygenation level-dependent (BOLD) signal (Eqs.7&8) have been used extensively to study neural function and oxygen metabolism in calibrated fMRI (13-15,55,61). For quantitation of venous dHb concentration $[dHb]_v$ required for $CMRO_2$, the R_2^* model determines $[dHb]_v$ up to a constant A (Eqs.7&8), which is a disadvantage compared to the absolute quantitation of $[dHb]_v$ by the QSM based method (Eq. 4.2). This may be explained by the underlying physics for R_2^* and QSM. QSM solves the field to susceptibility source inverse problem based on Maxwell's equation (21) using the phase of the gradient echo data. Magnetic susceptibility has a well-defined quantitative relationship with $[dHb]_v$ (Eq. 4.2). On the other hand, R_2^* is the decay rate of gradient echo magnitude signal and may be approximated as the variance of the field in a voxel (6,34,62).

Its relationship with $[dHb]_v$ is empirical and depends on a scaling factor that requires additional information to be determined (8,11,55). The calculation of the field variance requires input of detailed field pattern in a voxel that is not known, which is the fundamental cause of this indeterminacy of the R_2^* model. Measurements at a third brain state can estimate this scaling factor, which is why 3 brain states (normoxic, hyperoxic and hypercapnia) have been used in R_2^* based $CMRO_2$ mapping (13-15). Additionally, the empirical parameter $\beta \sim 1.5$ may be spatially varying (63), as $\beta \sim 1$ for voxels containing larger vessels (6) and $\beta \sim 2$ for voxels containing capillaries (7,61). This may explain the greater difference between QSM and R_2^* based $CMRO_2$ measurements in regions with large vessels such as the posterior region near the large sagittal sinus (PCA in Table 4.1). Furthermore, Eqs.7&8 may not properly account for the ferritin (non-heme iron) contribution to R_2^*, possibly causing overestimation of $CMRO_2$ in the basal ganglia area with known high ferritin concentration (Fig. 4.4c). Besides requiring fewer drug challenges, QSM based $CMRO_2$ offer other potential benefits such as reduced blooming artifacts near the air-tissue interface and improved robustness against changes in scanning parameters (64).

The voxel size used in this work was chosen mainly based on scan time and SNR considerations. In general, SNR is dictated by scan time, which in this study was kept comparable to that used in routine MRI (6 min for 3D ASL (65) and 7 min for QSM (66)) with the aim to prevent head motion and also to keep the total experiment time under 1 hour. As a result, the achievable spatial resolution for the ASL scan was 3 mm isotropic, which is lower than that of the QSM scan (0.5x0.5x3 mm^3). The derived $CMRO_2$ and OEF

maps therefore also have a 3 mm isotropic resolution, although due to the very small change in the observable MR signal between the two brain states we found that reliable quantitative analysis can be performed only with region-based (instead of voxel-based) measurements. This is a limitation of the current work and solutions for SNR improvement require further investigation.

In this work, several physiological parameters such as arterial oxygenation saturation level (SaO_2) and total hemoglobin concentration ($\Psi_{Hb} = 0.12$) were assumed fixed for all subjects (see Appendix). In clinical practice, these parameters can be measured for each individual subject using highly automated devices: SaO_2 can be obtained through pulse oximetry (67), and Ψ_{Hb} can be measured directly using hemoximetry or estimated from hematocrit measurement. In healthy subjects, SaO_2 and Ψ_{Hb} can range from 0.95 to 0.99 and 0.096 to 0.14 (68). Within these ranges, error propagation analysis showed a worst-case deviation of 11% from $CMRO_2$ obtained in GM with fixed SaO_2 and Ψ_{Hb} values, which suggests that our method is fairly robust against changes in these physiological parameters.

While previous works have reported similar OEF over the whole brain (69,70), we found that OEFs were slightly lower in WM than in GM (26.3 ±11.7% vs. 33.9 ± 9.6% pre-caffeine, and 45.0 ± 18.7% vs. 54.5 ± 13.2% post-caffeine, $p<0.05$). The observed discrepancy between WM and GM regions may be attributed to the challenges associated with accurately mapping the relationship between CBF and CBV in each region, which was derived empirically from normative PET data (50). A separate measurement of CBV

may be performed using a dynamic susceptibility contrast, or a dynamic QSM method (71) and extracellular contrast agents that clear rapidly before the administration of caffeine, unless it is performed as the last scan.

In this work, CSF was used to provide the reference value for brain parenchymal susceptibility. To overcome the effect of CSF flow, our GRE pulse sequence was flow-compensated in the readout (anterior-posterior) direction. When compared to a fully compensated pulse sequence (72) in three of our subjects, we found that the difference in susceptibility of the CSF (measured in lateral ventricles) was relatively small (4.1 ± 3.7 ppb, $p>0.05$) . Further work is needed to study the effect of CSF flow on QSM and $CMRO_2$ accuracy.

Caffeine administration has been shown to have no significant change in $CMRO_2$ (45). Other $CMRO_2$-invariant brain challenges may include hypercapnia and hyperoxia, which may have risks and discomforts associated with the prolonged (>10min) continuous inhalation of high concentration CO_2 and O_2 necessary for the data acquisition. In addition, this feasibility study lacks the second challenge for estimating coefficient A in calibrated BOLD. Further work is warranted to compare the proposed QSM-based with the existing R_2^* based methods that include the additional hyperoxia or hypercapnia challenges.

4.7 CONCLUSION

Quantitative susceptibility mapping can be used in conjunction with cerebral perfusion measurements before and after a vasoconstricting caffeine challenge to map cerebral metabolic rate of oxygen consumption and oxygen extraction fraction.

4.8 APPENDIX

Here we provide detailed derivation of Eq. 4.5 from Eq. 4.4 and estimation of parameters related to blood.

Derivation of Eq. 4.5 from Eq. 4.4

Eq. 4.4 is

$$\mathrm{CMRO_2} = 4\mathrm{CBF}\cdot[\mathrm{Hb}]\left(\frac{\chi-\chi_o}{\mathrm{CBV_v}\cdot\Psi_{\mathrm{Hb}}(\mathrm{X_{dHb}}-\mathrm{X_{oHb}})}-(1-\mathrm{SaO_2})\right) \quad [4.4]$$

Moving $\chi-\chi_o$ to the left side, we have:

$$\chi-\chi_o = \Psi_{\mathrm{Hb}}(\mathrm{X_{dHb}}-\mathrm{X_{oHb}})\left(\frac{\mathrm{CMRO_2}}{4[\mathrm{Hb}]}\cdot\frac{\mathrm{CBV_v}}{\mathrm{CBF}}+\mathrm{CBV_v}(1-\mathrm{SaO_2})\right) \quad [4.4a]$$

Equation 4a applies to each of the two brain states (pre- and post-caffeine), the difference of which can be written as:

$$\Delta\chi-\Delta\chi_o = \Psi_{\mathrm{Hb}}(\mathrm{X_{dHb}}-\mathrm{X_{oHb}})\left(\frac{\mathrm{CMRO_2}}{4[\mathrm{Hb}]}\cdot\Delta\left(\frac{\mathrm{CBV_v}}{\mathrm{CBF}}\right)+\Delta\mathrm{CBV_v}(1-\mathrm{SaO_2})\right) \quad [4.4b]$$

By rearranging Eq. 4.4b, we arrive at Eq.4.5:

$$\mathrm{CMRO_2} = \frac{4[\mathrm{Hb}]}{\Delta(\mathrm{CBV_v}/\mathrm{CBF})}\left(\frac{\Delta\chi-\Delta\chi_0}{\Psi_{\mathrm{Hb}}(\mathrm{X_{dHb}}-\mathrm{X_{oHb}})}-\Delta\mathrm{CBV_v}(1-\mathrm{SaO_2})\right) \quad [4.5]$$

Calculation of hemoglobin molar concentration in blood [Hb]

The hemoglobin molar concentration in blood [Hb] = 2.48 μmol/ml, is estimated from the Hematrocrit $\mathrm{Hct} = 0.47$ (68), Hb mass concentration in a RBC (0.34 g/ml) , and the molar mass of dHb $\mathrm{M_{Hb}} = 64450\times10^{-6}$ g/μmol (73).

$$[\mathrm{Hb}] = \frac{\mathrm{Hct} \cdot 0.34\ \mathrm{g/ml}}{\mathrm{M_{Hb}}} = 2.48\ \mu\mathrm{mol/ml}$$

Calculation of hemoglobin volume fraction in blood in blood Ψ_{Hb}

The hemoglobin volume fraction in blood $\Psi_{\mathrm{Hb}} = 0.12$ is estimated from [Hb], $\mathrm{M_{Hb}}$, and Hb concentration in pure aggregate ($\rho_{\mathrm{Hb}} = 1.335\mathrm{g/ml}$) (74).

$$\Psi_{\mathrm{Hb}} = \frac{[\mathrm{Hb}] \cdot \mathrm{M_{Hb}}}{\rho_{\mathrm{Hb}}} = 0.12$$

Calculation of oxyhemoglobin $\mathrm{X_{oHb}}$ and deoxyHemoglobin $\mathrm{X_{dHb}}$ volume susceptibility

The volume susceptibility of oxyhemoglobins $\mathrm{X_{oHb}}$ relative to water is estimated from the reported mass susceptibility of globin relative to vacuum, -4π (0.587×10^{-6} mL/g) (4π for conversion from cgs to si) (74,75) as,

$$\mathrm{X_{oHb}} = (-4\pi(0.587 \times 10^{-6}\ \mathrm{ml/g})\rho_{\mathrm{Hb}}) - (-9035\ \mathrm{ppb}) = -813\ \mathrm{ppb}$$

where $-9035\,ppb$ is the volume susceptibility of water with respect to vacuum (76).

The volume susceptibility of oxyhemoglobins $\mathrm{X_{dHb}}$ relative to water is estimated by adding to $\mathrm{X_{oHb}}$ a paramagnetic term of 5.25 μ_{B} (Bohr magneton $\mu_{\mathrm{B}} = 9.274 \times 10^{-24}$ J/T) per heme (77,78) according to (18,34,79),

$$X_{dHb} = 4\frac{N_A \rho_{Hb} \mu_0 (5.25\mu_B)^2}{3M_{Hb} k_B T} + X_{oHb} = 10765 \text{ ppb}$$

where $N_A = 6.02 \times 10^{23}$ mol^{-1} is the Avogadro number, $\mu_0 = 4\pi \times 10^{-7}$ Tm/A is the magnetic permeability in vacuum, $k_B = 1.38 \times 10^{-23}$ J/K is the Boltzman constant, and $T = 310$ K is the human body temperature.

REFERENCES

1. Derdeyn CP, Videen TO, Yundt KD, Fritsch SM, Carpenter DA, Grubb RL, Powers WJ. Variability of cerebral blood volume and oxygen extraction: stages of cerebral haemodynamic impairment revisited. Brain : a journal of neurology 2002;125(Pt 3):595-607.

2. Gupta A, Chazen JL, Hartman M, Delgado D, Anumula N, Shao H, Mazumdar M, Segal AZ, Kamel H, Leifer D, Sanelli PC. Cerebrovascular reserve and stroke risk in patients with carotid stenosis or occlusion: a systematic review and meta-analysis. Stroke; a journal of cerebral circulation 2012;43(11):2884-2891.

3. Gupta A, Baradaran H, Schweitzer AD, Kamel H, Pandya A, Delgado D, Wright D, Hurtado-Rua S, Wang Y, Sanelli PC. Oxygen extraction fraction and stroke risk in patients with carotid stenosis or occlusion: a systematic review and meta-analysis. AJNR American journal of neuroradiology 2014;35(2):250-255.

4. Mintun MA, Raichle ME, Martin WR, Herscovitch P. Brain oxygen utilization measured with O-15 radiotracers and positron emission tomography. J Nucl Med 1984;25(2):177-187.

5. Pauling L, Coryell CD. The Magnetic Properties and Structure of Hemoglobin, Oxyhemoglobin and Carbonmonoxyhemoglobin. Proceedings of the National Academy of Sciences of the United States of America 1936;22(4):210-216.

6. Yablonskiy DA, Haacke EM. Theory of NMR signal behavior in magnetically inhomogeneous tissues: the static dephasing regime. Magnetic resonance in medicine : official journal of the Society of Magnetic Resonance in Medicine / Society of Magnetic Resonance in Medicine 1994;32(6):749-763.

7. Ogawa S, Menon RS, Tank DW, Kim SG, Merkle H, Ellermann JM, Ugurbil K. Functional brain mapping by blood oxygenation level-dependent contrast magnetic resonance imaging. A comparison of signal characteristics with a biophysical model. Biophys J 1993;64(3):803-812.

8. Boxerman JL, Bandettini PA, Kwong KK, Baker JR, Davis TL, Rosen BR, Weisskoff RM. The intravascular contribution to fMRI signal change: Monte Carlo modeling and diffusion-weighted studies in vivo. Magnetic resonance in medicine : official journal of the Society of Magnetic Resonance in Medicine / Society of Magnetic Resonance in Medicine 1995;34(1):4-10.

9. Lu H, Ge Y. Quantitative evaluation of oxygenation in venous vessels using T2-Relaxation-Under-Spin-Tagging MRI. Magnetic resonance in medicine : official journal of the Society of Magnetic Resonance in Medicine / Society of Magnetic Resonance in Medicine 2008;60(2):357-363.

10. van Zijl PC, Eleff SM, Ulatowski JA, Oja JM, Ulug AM, Traystman RJ, Kauppinen RA. Quantitative assessment of blood flow, blood volume and blood oxygenation effects in functional magnetic resonance imaging. Nat Med 1998;4(2):159-167.

11. Kennan RP, Zhong J, Gore JC. Intravascular susceptibility contrast mechanisms in tissues. Magnetic resonance in medicine : official journal of the Society of Magnetic Resonance in Medicine / Society of Magnetic Resonance in Medicine 1994;31(1):9-21.

12. Bandettini PA, Wong EC, Jesmanowicz A, Hinks RS, Hyde JS. Spin-echo and gradient-echo EPI of human brain activation using BOLD contrast: a comparative study at 1.5 T. NMR in biomedicine 1994;7(1-2):12-20.

13. Bulte DP, Kelly M, Germuska M, Xie J, Chappell MA, Okell TW, Bright MG, Jezzard P. Quantitative measurement of cerebral physiology using respiratory-calibrated MRI. NeuroImage 2012;60(1):582-591.

14. Gauthier CJ, Hoge RD. Magnetic resonance imaging of resting OEF and CMRO(2) using a generalized calibration model for hypercapnia and hyperoxia. NeuroImage 2012;60(2):1212-1225.

15. Wise RG, Harris AD, Stone AJ, Murphy K. Measurement of OEF and absolute CMRO2: MRI-based methods using interleaved and combined hypercapnia and hyperoxia. NeuroImage 2013;83:135-147.

16. Li J, Chang S, Liu T, Wang Q, Cui D, Chen X, Jin M, Wang B, Pei M, Wisnieff C, Spincemaille P, Zhang M, Wang Y. Reducing the object orientation dependence of susceptibility effects in gradient echo MRI through quantitative susceptibility mapping. Magnetic resonance in medicine : official journal of the Society of Magnetic Resonance in Medicine / Society of Magnetic Resonance in Medicine 2012;68(5):1563-1569.

17. Jain V, Abdulmalik O, Propert KJ, Wehrli FW. Investigating the magnetic susceptibility properties of fresh human blood for noninvasive oxygen saturation quantification. Magnetic resonance in medicine : official journal of the Society of Magnetic Resonance in Medicine / Society of Magnetic Resonance in Medicine 2012;68(3):863-867.

18. Spees WM, Yablonskiy DA, Oswood MC, Ackerman JJ. Water proton MR properties of human blood at 1.5 Tesla: magnetic susceptibility, T(1), T(2), T*(2), and non-Lorentzian signal behavior. Magnetic resonance in medicine : official journal of the Society of Magnetic Resonance in Medicine / Society of Magnetic Resonance in Medicine 2001;45(4):533-542.

19. Liu J, Liu T, de Rochefort L, Ledoux J, Khalidov I, Chen W, Tsiouris AJ, Wisnieff C, Spincemaille P, Prince MR, Wang Y. Morphology enabled dipole inversion for quantitative susceptibility mapping using structural consistency between the magnitude image and the susceptibility map. NeuroImage 2012;59(3):2560-2568.

20. Liu T, Liu J, de Rochefort L, Spincemaille P, Khalidov I, Ledoux JR, Wang Y. Morphology enabled dipole inversion (MEDI) from a single-angle acquisition: comparison with COSMOS in human brain imaging. Magnetic resonance in medicine : official journal of the Society of Magnetic Resonance in Medicine / Society of Magnetic Resonance in Medicine 2011;66(3):777-783.

21. de Rochefort L, Liu T, Kressler B, Liu J, Spincemaille P, Lebon V, Wu J, Wang Y. Quantitative susceptibility map reconstruction from MR phase data using bayesian regularization: validation and application to brain imaging. Magnetic resonance in medicine : official journal of the Society of Magnetic Resonance in Medicine / Society of Magnetic Resonance in Medicine 2010;63(1):194-206.

22. Li W, Wu B, Liu C. Quantitative susceptibility mapping of human brain reflects spatial variation in tissue composition. NeuroImage 2011;55(4):1645-1656.

23. Schweser F, Deistung A, Sommer K, Reichenbach JR. Toward online reconstruction of quantitative susceptibility maps: superfast dipole inversion. Magnetic resonance in medicine : official journal of the Society of Magnetic Resonance in Medicine / Society of Magnetic Resonance in Medicine 2013;69(6):1582-1594.

24. de Rochefort L, Brown R, Prince MR, Wang Y. Quantitative MR susceptibility mapping using piece-wise constant regularized inversion of the magnetic field. Magnetic resonance in medicine : official journal of the Society of Magnetic Resonance in Medicine / Society of Magnetic Resonance in Medicine 2008;60(4):1003-1009.

25. Kressler B, de Rochefort L, Liu T, Spincemaille P, Jiang Q, Wang Y. Nonlinear regularization for per voxel estimation of magnetic susceptibility distributions from MRI field maps. IEEE transactions on medical imaging 2010;29(2):273-281.

26. Wharton S, Bowtell R. Whole-brain susceptibility mapping at high field: a comparison of multiple- and single-orientation methods. NeuroImage 2010;53(2):515-525.

27. Wu B, Li W, Guidon A, Liu C. Whole brain susceptibility mapping using compressed sensing. Magnetic resonance in medicine : official journal of the Society of Magnetic Resonance in Medicine / Society of Magnetic Resonance in Medicine 2012;67(1):137-147.

28. Liu T, Spincemaille P, de Rochefort L, Kressler B, Wang Y. Calculation of susceptibility through multiple orientation sampling (COSMOS): a method for conditioning the inverse problem from measured magnetic field map to susceptibility source image in MRI. Magnetic resonance in medicine : official journal of the Society of Magnetic Resonance in Medicine / Society of Magnetic Resonance in Medicine 2009;61(1):196-204.

29. Bilgic B, Pfefferbaum A, Rohlfing T, Sullivan EV, Adalsteinsson E. MRI estimates of brain iron concentration in normal aging using quantitative susceptibility mapping. NeuroImage 2012;59(3):2625-2635.

30. Li L, Leigh JS. Quantifying arbitrary magnetic susceptibility distributions with MR. Magnetic resonance in medicine : official journal of the Society of Magnetic Resonance in Medicine / Society of Magnetic Resonance in Medicine 2004;51(5):1077-1082.

31. Haacke EM, Cheng NY, House MJ, Liu Q, Neelavalli J, Ogg RJ, Khan A, Ayaz M, Kirsch W, Obenaus A. Imaging iron stores in the brain using magnetic resonance imaging. Magnetic resonance imaging 2005;23(1):1-25.

32. Shmueli K, de Zwart JA, van Gelderen P, Li TQ, Dodd SJ, Duyn JH. Magnetic susceptibility mapping of brain tissue in vivo using MRI phase data. Magnetic resonance in medicine : official journal of the Society of Magnetic Resonance in Medicine / Society of Magnetic Resonance in Medicine 2009;62(6):1510-1522.

33. Liu T, Wisnieff C, Lou M, Chen W, Spincemaille P, Wang Y. Nonlinear formulation of the magnetic field to source relationship for robust quantitative susceptibility mapping. Magnetic resonance in medicine : official journal of the Society of Magnetic Resonance in Medicine / Society of Magnetic Resonance in Medicine 2013;69(2):467-476.

34. Wang Y. Principles of Magnetic Resonance Imaging: physics concepts, pulse sequences & biomedical applications: www.createspace.com/4001776; 2012 Oct 3.

35. Wang Y, Liu T. Quantitative susceptibility mapping (QSM): Decoding MRI data for a tissue magnetic biomarker. Magnetic resonance in medicine : official journal of the Society of Magnetic Resonance in Medicine / Society of Magnetic Resonance in Medicine 2014;doi. 10.1002/mrm.25358.

36. Haacke EM, Lai S, Reichenbach JR, Kuppusamy K, Hoogenraad FG, Takeichi H, Lin W. In vivo measurement of blood oxygen saturation using magnetic resonance imaging: a direct validation of the blood oxygen level-dependent concept in functional brain imaging. Human brain mapping 1997;5(5):341-346.

37. Fan AP, Benner T, Bolar DS, Rosen BR, Adalsteinsson E. Phase-based regional oxygen metabolism (PROM) using MRI. Magnetic resonance in medicine : official journal of the Society of Magnetic Resonance in Medicine / Society of Magnetic Resonance in Medicine 2012;67(3):669-678.

38. Li C, Langham MC, Epstein CL, Magland JF, Wu J, Gee J, Wehrli FW. Accuracy of the cylinder approximation for susceptometric measurement of intravascular oxygen saturation. Magnetic resonance in medicine : official journal of the Society of Magnetic Resonance in Medicine / Society of Magnetic Resonance in Medicine 2012;67(3):808-813.

39. Fan AP, Bilgic B, Gagnon L, Witzel T, Bhat H, Rosen BR, Adalsteinsson E. Quantitative oxygenation venography from MRI phase. Magnetic resonance in medicine : official journal of the Society of Magnetic Resonance in Medicine / Society of Magnetic Resonance in Medicine 2014;72(1):149-159.

40. Wehrli FW, Rodgers ZB, Jain V, Langham MC, Li C, Licht DJ, Magland J. Time-resolved MRI oximetry for quantifying CMRO(2) and vascular reactivity. Academic radiology 2014;21(2):207-214.

41. Detre JA, Leigh JS, Williams DS, Koretsky AP. Perfusion imaging. Magn Reson Med 1992;23(1):37-45.

42. Weisskoff RM, Kiihne S. MRI susceptometry: image-based measurement of absolute susceptibility of MR contrast agents and human blood. Magnetic resonance in medicine : official journal of the Society of Magnetic Resonance in Medicine / Society of Magnetic Resonance in Medicine 1992;24(2):375-383.

43. Lunt MJ, Ragab S, Birch AA, Schley D, Jenkinson DF. Comparison of caffeine-induced changes in cerebral blood flow and middle cerebral artery blood velocity shows that caffeine reduces middle cerebral artery diameter. Physiol Meas 2004;25(2):467-474.

44. Cameron OG, Modell JG, Hariharan M. Caffeine and human cerebral blood flow: a positron emission tomography study. Life sciences 1990;47(13):1141-1146.

45. Perthen JE, Lansing AE, Liau J, Liu TT, Buxton RB. Caffeine-induced uncoupling of cerebral blood flow and oxygen metabolism: a calibrated BOLD fMRI study. NeuroImage 2008;40(1):237-247.

46. Cusack R, Papadakis N. New robust 3-D phase unwrapping algorithms: application to magnetic field mapping and undistorting echoplanar images. NeuroImage 2002;16(3 Pt 1):754-764.

47. Liu T, Khalidov I, de Rochefort L, Spincemaille P, Liu J, Tsiouris AJ, Wang Y. A novel background field removal method for MRI using projection onto dipole fields (PDF). NMR in biomedicine 2011;24(9):1129-1136.

48. Pei M, Nguyen TD, Thimmappa ND, Salustri C, Dong F, Cooper MA, Li J, Prince MR, Wang Y. Algorithm for fast monoexponential fitting based on Auto-Regression on Linear Operations (ARLO) of data. Magnetic resonance in medicine : official journal of the Society of Magnetic Resonance in Medicine / Society of Magnetic Resonance in Medicine 2014;10.1002/mrm.25137.

49. Zhang Y, Brady M, Smith S. Segmentation of brain MR images through a hidden Markov random field model and the expectation-maximization algorithm. IEEE transactions on medical imaging 2001;20(1):45-57.

50. Leenders KL, Perani D, Lammertsma AA, Heather JD, Buckingham P, Healy MJ, Gibbs JM, Wise RJ, Hatazawa J, Herold S, et al. Cerebral blood flow, blood volume and oxygen utilization. Normal values and effect of age. Brain : a journal of neurology 1990;113 (Pt 1):27-47.

51. Grubb RL, Jr., Raichle ME, Eichling JO, Ter-Pogossian MM. The effects of changes in PaCO2 on cerebral blood volume, blood flow, and vascular mean transit time. Stroke; a journal of cerebral circulation 1974;5(5):630-639.

52. Jenkinson M, Bannister P, Brady M, Smith S. Improved optimization for the robust and accurate linear registration and motion correction of brain images. NeuroImage 2002;17(2):825-841.

53. Jenkinson M, Smith S. A global optimisation method for robust affine registration of brain images. Med Image Anal 2001;5(2):143-156.

54. Hoge RD, Atkinson J, Gill B, Crelier GR, Marrett S, Pike GB. Investigation of BOLD signal dependence on cerebral blood flow and oxygen consumption: the deoxyhemoglobin dilution model. Magnetic resonance in medicine : official journal of the Society of Magnetic Resonance in Medicine / Society of Magnetic Resonance in Medicine 1999;42(5):849-863.

55. Buxton RB, Uludag K, Dubowitz DJ, Liu TT. Modeling the hemodynamic response to brain activation. NeuroImage 2004;23 Suppl 1:S220-233.

56. Ito H, Kanno I, Kato C, Sasaki T, Ishii K, Ouchi Y, Iida A, Okazawa H, Hayashida K, Tsuyuguchi N, Ishii K, Kuwabara Y, Senda M. Database of normal human cerebral blood flow, cerebral blood volume, cerebral oxygen extraction fraction and cerebral metabolic rate of oxygen measured by positron emission tomography with 15O-labelled carbon dioxide or water, carbon monoxide and oxygen: a multicentre study in Japan. Eur J Nucl Med Mol Imaging 2004;31(5):635-643.

57. Ances BM, Leontiev O, Perthen JE, Liang C, Lansing AE, Buxton RB. Regional differences in the coupling of cerebral blood flow and oxygen metabolism changes in response to activation: implications for BOLD-fMRI. NeuroImage 2008;39(4):1510-1521.

58. Ances BM, Liang CL, Leontiev O, Perthen JE, Fleisher AS, Lansing AE, Buxton RB. Effects of aging on cerebral blood flow, oxygen metabolism, and blood oxygenation level dependent responses to visual stimulation. Human brain mapping 2009;30(4):1120-1132.

59. Bulte DP, Drescher K, Jezzard P. Comparison of hypercapnia-based calibration techniques for measurement of cerebral oxygen metabolism with MRI. Magnetic resonance in medicine : official journal of the Society of Magnetic Resonance in Medicine / Society of Magnetic Resonance in Medicine 2009;61(2):391-398.

60. Chen Y, Parrish TB. Caffeine dose effect on activation-induced BOLD and CBF responses. NeuroImage 2009;46(3):577-583.

61. Blockley NP, Griffeth VE, Simon AB, Buxton RB. A review of calibrated blood oxygenation level-dependent (BOLD) methods for the measurement of task-induced changes in brain oxygen metabolism. NMR in biomedicine 2013;26(8):987-1003.

62. Wang Y. Quantitative Susceptibility Mapping: Magnetic Resonance Imaging of Tissue Magnetism. www.createspace.com/4346993; June 2013.

63. Davis TL, Kwong KK, Weisskoff RM, Rosen BR. Calibrated functional MRI: mapping the dynamics of oxidative metabolism. Proceedings of the National Academy of Sciences of the United States of America 1998;95(4):1834-1839.

64. Liu T, Surapaneni K, Lou M, Cheng L, Spincemaille P, Wang Y. Cerebral microbleeds: burden assessment by using quantitative susceptibility mapping. Radiology 2012;262(1):269-278.

65. Wong AM, Yan FX, Liu HL. Comparison of three-dimensional pseudo-continuous arterial spin labeling perfusion imaging with gradient-echo and spin-echo dynamic susceptibility contrast MRI. Journal of magnetic resonance imaging : JMRI 2014;39(2):427-433.

66. Langkammer C, Liu T, Khalil M, Enzinger C, Jehna M, Fuchs S, Fazekas F, Wang Y, Ropele S. Quantitative susceptibility mapping in multiple sclerosis. Radiology 2013;267(2):551-559.

67. Gehring H, Duembgen L, Peterlein M, Hagelberg S, Dibbelt L. Hemoximetry as the "gold standard"? Error assessment based on differences among identical blood gas analyzer devices of five manufacturers. Anesthesia and analgesia 2007;105(6 Suppl):S24-30, tables of contents.

68. Hoffman R, Bussel JB, Cushing MM, Giardina PJ. Hematology : basic principles and practice. Philadelphia, PA: Churchill Livingstone/Elsevier; 2009. xxvii, 2523 p. p.

69. Gusnard DA, Raichle ME, Raichle ME. Searching for a baseline: functional imaging and the resting human brain. Nature reviews Neuroscience 2001;2(10):685-694.

70. He X, Zhu M, Yablonskiy DA. Validation of oxygen extraction fraction measurement by qBOLD technique. Magnetic resonance in medicine : official journal of the Society of Magnetic Resonance in Medicine / Society of Magnetic Resonance in Medicine 2008;60(4):882-888.

71. Xu B, Spincemaille P, Liu T, Prince MR, Dutruel S, Gupta A, Thimmappa ND, Wang Y. Quantification of cerebral perfusion using dynamic quantitative susceptibility mapping. Magnetic resonance in medicine : official journal of the Society of Magnetic Resonance in Medicine / Society of Magnetic Resonance in Medicine 2014;doi. 10.1002/mrm.25257.

72. Xu B, Liu T, Spincemaille P, Prince M, Wang Y. Flow compensated quantitative susceptibility mapping for venous oxygenation imaging. Magnetic resonance in medicine : official journal of the Society of Magnetic Resonance in Medicine / Society of Magnetic Resonance in Medicine 2014;72(2):438-445.

73. Dickerson RE, Geis I. Hemoglobin : structure, function, evolution, and pathology. Menlo Park, Calif.: Benjamin/Cummings Pub. Co.; 1983. 176 p. p.

74. Savicki JP, Lang G, Ikeda-Saito M. Magnetic susceptibility of oxy- and carbonmonoxyhemoglobins. Proc Natl Acad Sci U S A 1984;81(17):5417-5419.

75. Cerdonio M, Morante S, Torresani D, Vitale S, DeYoung A, Noble RW. Reexamination of the evidence for paramagnetism in oxy- and carbonmonoxyhemoglobins. Proceedings of the National Academy of Sciences of the United States of America 1985;82(1):102-103.

76. Chemical Rubber Company. CRC standard mathematical tables. Boca Raton, Fla.: CRC Press; 1987. p v.

77. Pauling L. General Chemistry: Dover Publications; 1988.

78. Pauling L, Coryell CD. The Magnetic Properties and Structure of Hemoglobin, Oxyhemoglobin and Carbonmonoxyhemoglobin. Proceedings of the National Academy of Sciences of the United States of America 1936;22(4):210-216.

79. McDermott A. Structure and dynamics of membrane proteins by magic angle spinning solid-state NMR. Annual review of biophysics 2009;38:385-403.

Chapter 5

Improving Signal-To-Noise Ratio (SNR) and Practicality of QSM-based $CMRO_2$ Mapping With Priors and Hyperventilation Challenge

5.1 ABSTRACT

Purpose

Our objective was to demonstrate the feasibility of using hyperventilation as an efficient vasoconstrictive challenge and prior knowledge as denoising constraints for cerebral metabolic rate of oxygen ($CMRO_2$) mapping based upon quantitative susceptibility mapping (QSM).

Methods

3D multi-echo gradient echo and arterial spin labeling imaging were performed to calculate QSM and perfusion maps before and after a hyperventilation challenge in 11 healthy subjects. For comparison, this was repeated using a caffeine challenge. Whole brain $CMRO_2$ and oxygen extraction fraction (OEF) maps were computed using constrained optimization. Hyperventilation scans were repeated to measure reproducibility. Regional agreement of $CMRO_2$ and OEF maps was analyzed within the cortical gray matter (CGM) using t-test and Bland-Altman plots.

Results

Hyperventilation challenge eliminates the 30 min waiting time needed for caffeine to exert its vaso-constrictive effects. Mean $CMRO_2$ (in μmol/100g/min) obtained in CGM using the caffeine and repeated hyperventilation scans were 149±16, 153±19, and 150±20 respectively. This corresponded to an OEF of 33.6±3.4%, 32.3±3.2%, and 34.1±3.8% at baseline state and 39.8±4.8%, 43.6±6.2% and to 42.8±6.8% at challenged state, respectively. Hyperventilation scans produced a good agreement of $CMRO_2$ and OEF values.

Conclusion

Hyperventilation is a feasible, reproducible and efficient vasoconstrictive challenge for QSM based quantitative $CMRO_2$ mapping.

5.2 INTRODUCTION

The quantitative mapping of cerebral metabolic rate of oxygen ($CMRO_2$) and oxygen extraction fraction (OEF) has long been sought after in both research and clinical settings as important indicators for neural viability and activity (1-3). As oxygen is released to brain tissue, the weakly diamagnetic oxyhemoglobin (oHb) turns into to the strongly paramagnetic deoxyhemoglobin (dHb) and induces magnetic field inhomogeneity detectable by MRI (4,5). $CMRO_2$ mapping techniques based on MRI include: 1) quantitative imaging of extraction of oxygen and tissue consumption (QUIXOTIC) (6) to map brain oxygen consumption from the transversal relaxation rates R2 of venous blood. QUIXOTIC uses venular-targeted velocity-selective spin labeling technique but has limitations including the difficulty in selecting cutoff velocity and outflow time for targeting venular blood flow, the imperfection of velocity selection profile and T1 nulling of arterial blood and the prolong scan time (~30 minutes). 2) calibrated fMRI approaches by modeling $R2^*$ in blood oxygen level dependent (BOLD) contrast and by combining with hyperoxia and hypercapnia (7-9). These techniques are challenging to implement because they require precise gas manipulation and data acquisitions in three brain states. 3) estimation of dHb concentration ([dHb]) by modeling R2' from asymmetric spin echo data (10,11) or by separating R2 and R2' contribution to R2* in 3D multi gradient echo data (12). However, accurate R2' fitting from gradient echo data requires dense sampling of the early signal decay curve and may be prone to noise propagation (13). In addition, $R2^*$ images are subject to blooming artifacts surrounding high susceptibility sources (such as

veins) and are highly dependent on imaging parameters including field strength, echo time, voxel size, and object orientation (14,15).

Unlike R2 and $R2^*$, [dH] is linearly related to blood magnetic susceptibility that is independent of imaging parameters (16,17). Quantitative susceptibility mapping (QSM) derived from the complex GRE signal (18-21) can be used to quantify blood oxygenation in veins (22-26) and brain tissues (27). $CMRO_2$ and OEF maps can be computed using QSM and arterial spin labeling (ASL) data acquired in two brain states, such as before and after an acetazolamide or caffeine challenge in healthy subjects (27). However, these challenges would add a substantial waiting time on top of the MRI acquisition time. For example, the coffee challenge requires an additional 30 minutes for the caffeine to exert its maximal vaso-constrictive effects. Similarly, acetazolamide challenge requires 15 minutes to exert its maximal vasodilatory effect and is limited by potential adverse effects of drug administration (28). Another issue with the previous reconstruction method (27) is that the generated $CMRO_2$ and OEF maps are quite noisy.

Hyperventilation is known to reduce partial pressure of carbon dioxide (CO_2) in arterial blood and can cause 40% decrease of cerebral blood flow within minutes without significantly changing $CMRO_2$ (29,30), therefore, even though hyperventilation might induce minor discomforts in subjects, it can be used with QSM to generate fast $CMRO_2$ mapping. Additionally, prior knowledge may be used to denoise $CMRO_2$ and OEF maps. Accordingly, the purpose of this study was to use hyperventilation as an efficient vasoconstrictive and constrained optimization for quantitative $CMRO_2$ mapping.

5.3 BAYESIAN APPROACHES FOR SNR IMPROVEMENT

$CMRO_2$ and OEF Reconstruction

According to mass conservation, $CMRO2$ can be expressed as

$$\mathrm{CMRO_2} = \mathrm{CBF} \cdot ([dH]_v - [dH]_a) \quad [5.1]$$

where $\mathrm{CMRO_2}$ is cerebral metabolic rate of oxygen ($\mu\mathrm{mol}/100\mathrm{g}/\mathrm{min}$), CBF is cerebral blood flow ($\mathrm{ml}/100\mathrm{g}/\mathrm{min}$) measured using ASL, $[dH]_v$ and $[dH]_a$ are deoxyheme molar concentration ($\mu\mathrm{mol}/\mathrm{ml}$) in venous and in arterial blood respectively.

OEF can be expressed as

$$\mathrm{OEF} = \frac{[dH]_v - [dH]_a}{[H] - [dH]_a} \quad [5.2]$$

Where $[H] = 7.53$ $\mu\mathrm{mol}/\mathrm{ml}$ is heme molar concentration in tissue blood assuming a tissue blood hematocrit (Hct) of $\mathrm{Hct}_{tissue} = 0.357$, which is estimated from an assumed hematocrit of $\mathrm{Hct}_{ss} = 0.47$ in the straight sinus and a Hct ratio of 0.759 between large vessel and brain tissue (31). (See appendix for detailed derivation of $[H]$). $[dH]_a = 0.02\,[H] = 0.15$ $\mu\mathrm{mol}/\mathrm{ml}$ assuming 98% arterial oxygenation.

$[dH]_v$ in Eq. 5.2 can be mapped using QSM (27). The voxel susceptibility, χ, in QSM can be expressed as a volume weighted sum of susceptibility contribution from arterial and venous blood, and non-blood tissue:

$$\chi = \mathrm{CBV_v} \cdot X_{dH,mol} \cdot [dH]_v + \chi_{\mathrm{nb}} + \chi_0. \quad [5.3]$$

The first term in the right side of Eq. 5.3 reflects the susceptibility contribution from venous dH. $\mathrm{CBV_v} = 0.77\mathrm{CBV}$ is the venous blood volume fraction in a voxel (32), CBV is the total

blood volume fraction in a voxel (see below), $\mathrm{X_{dH,mol}} = 151.054$ ppb $\frac{ml}{\mu mol}$ is the molar magnetic susceptibility of dH (16,17).

The second term χ_{nb} reflects susceptibility contributions from non-blood tissue sources (such as ferritin).

The third term χ_{o} in the right side of Eq. 5.3 reflects susceptibility contributions from pure oxygenated blood $\mathrm{X_{ba}}$, and arterial deoxyheme:

$$\chi_{\mathrm{o}} = \mathrm{CBV} \cdot \mathrm{X_{ba}} + \mathrm{CBV_a} \cdot X_{dH,mol} \cdot [dH]_a, \quad [5.4]$$

with $\mathrm{CBV_a} = \mathrm{CBV} - \mathrm{CBV_v} = 0.23\mathrm{CBV}$ is the arterial blood volume fraction in a voxel (32), and $\mathrm{X_{ba}}$ is is the volume susceptibility for pure oxygenated blood,

$$\mathrm{X_{ba}} = Hct_{tissue}\delta_{\mathrm{Hb}} \cdot \mathrm{X_{oHb}} + (1 - Hct_{tissue}\delta_{\mathrm{Hb}})\mathrm{X_p} = -108.3 \text{ ppb}$$

Where $\mathrm{X_{oHb}} = -813$ ppb and $\mathrm{X_p} = -37.7$ ppb are the oxyhemoglobin and blood plasma volume susceptibility (17,25,33), $\delta_{\mathrm{Hb}} = 0.255$ is the volume fraction of Hb in RBC. See Appendix for detailed derivation of $\mathrm{X_{oHb}}$ and δ_{Hb}.

Substituting Eq. 5.3 into Eq. 5.1, we obtained the following expressions for $\mathrm{CMRO_2}$ an OEF:

$$\mathrm{CMRO_2} = CBF\left(\frac{\chi - \chi_{\mathrm{nb}} - \chi_{\mathrm{o}}}{\mathrm{CBV_v} \cdot X_{dH,mol}} - [dH]_a\right) \quad [5.5]$$

In Eq. 5.5, there are two unknowns: $\mathrm{CMRO_2}$ and the non-blood susceptibility contribution χ_{nb}. With susceptibility and blood flow measurements of baseline and challenged brain states, $\mathrm{CMRO_2}$ and subsequently OEF can be calculated by solving Eq. 5.4 over two brain states.

In previous work (27), Eq. 5.5 was solved directly for $CMRO_2$ using a conjugate gradient method without constraints, which led to noisy $CMRO_2$ maps. Noise in the solution for a large linear system can be reduced by improving the condition number using constraints and preconditioning (34). We imposed a physiologically meaningful constraint on OEF ($0 \leq OEF \leq 1$) by searching for OEF instead of $CMRO_2$. The OEFs at baseline (OEF_{base}) and challenge (OEF_{chal}) and susceptibility from non-blood tissue sources (such as ferritin) χ_{nb} were organized into a vector of unknowns x in a linear system $Ax = b$ format:

$$A = \begin{bmatrix} CBV_{v,base} \cdot X_{dH,mol}([H] - [dH]_a) & 0 & 1 \\ 0 & CBV_{v,chal} \cdot X_{dH,mol}([H] - [dH]_a) & 1 \\ CBF_{base} & -\gamma CBF_{chal} & 0 \end{bmatrix}$$

$$b = \begin{bmatrix} \chi_{base} - CBV_{base} \cdot \left(\mathrm{X_{ba}} + X_{dH,mol} \cdot [dH]_a\right) \\ \chi_{chal} - CBV_{chal} \cdot \left(\mathrm{X_{ba}} + X_{dH,mol} \cdot [dH]_a\right) \\ 0 \end{bmatrix}$$

$$x = \begin{bmatrix} OEF_{base} \\ OEF_{chal} \\ \chi_{nb} \end{bmatrix} \quad [5.6]$$

Here γ is the ratio between global $CMRO_2$ estimated from the straight sinus and CBF maps before and after the challenge:

$$\gamma = \frac{CMRO_{2,base}^{global}}{CMRO_{2,chal}^{global}} = \frac{([H] - [dH]_a) OEF_{base}^{v} \overline{CBF_{base,\imath}}}{([H] - [dH]_a) OEF_{chal}^{v} \overline{CBF_{chal,\imath}}}$$

Here, global cerebral blood flow was estimated by averaging CBF over all brain voxels ($\overline{CBF_\imath}$), denoted by i and OEF_{base}^{v} and OEF_{chal}^{v} were estimated from the magnetic

susceptibility of venous blood in the straight sinus measured in ROIs drawn by a neuroradiologist with 10 years' experience (A.G.) using Eq. 5.3 with $CBV = CBV_{\mathrm{v}} = 100\%$ and $\chi_{nb} = 0$ as these voxels consisted of venous blood only, and replacing Hct_{tissue} with $Hct_{ss} = 0.47$. We further imposed a global physiological constraint based on the expectation that the global $CMRO_2$ calculated from the $CMRO_2$ map should be similar to that calculated from global OEF estimated from susceptibility of venous blood in straight sinus, and global CBF estimated from CBF maps by summing all voxels covering the whole brain according to mass conservation. Lastly, we applied a right preconditioning technique (34) to improve convergence speed and reduce error propagation in the solution by redefining the system of equations as $A^*x^* = b$, where $A^* = AP$ and $x^* = P^{-1}x$. $P = diag(1,1,\alpha)$ where α is a scaling factor chosen such that the elements of x^* have similar order of magnitude. Since the blood contribution to voxel susceptibility is relatively small due to small CBV (~5%), in this work we set $\alpha = \max\{|\chi_{base}|, 75ppb\}$. Accordingly, the constrained solution x^* was obtained by minimizing the following cost function using a limited-memory Broyden–Fletcher–Goldfarb–Shanno-Bound (L-BFGS-B) algorithm (35,36) with physiological bounds on OEF between 0 and 1:

$$x^* = \arg\min_{x^*} \left\{ \begin{array}{c} \|A^*x^* - b\|_2^2 + \\ \lambda\left(CMRO_{2,base}^{global} - \overline{CMRO_{2,base,\iota}}\right)^2 + \lambda\left(CMRO_{2,base}^{global} - \overline{CMRO_{2,chal,\iota}}\right)^2 \end{array} \right\} \quad [5.7]$$

The second and third terms impose the physiological constrain that the global $CMRO_2$ estimated from $CMRO_2$ maps to be similar to the global $CMRO_2$ estimated from draining veins in both baseline and challenged states. GM and WM data were fitted separately to

ensure proper convergence for each. λ is chosen based on an average value obtained by L-Curve analysis (37) on three randomly selected subjects. The iteration was terminated when the relative residual was less than 0.025%.

For this feasibility study, $\mathrm{CBV_{base}}$ was estimated from $\mathrm{CBF_{base}}$ based on a linear regression derived from CBF and CBV values in gray and white matter measured using ^{15}O steady-state inhalation PET in 34 healthy subjects: $\mathrm{CBV} = (0.0723\ \mathrm{CBF} + 1.144)/100$ (38). $\mathrm{CBV_{chal}}$ was estimated from $\mathrm{CBV_{base}}$ using Grubb's exponent of 0.38 (39). Venous blood volume was assumed to remain the same after challenges (40,41).

5.4 EXPERIMENTS AND ANALYSIS

The study was approved by the local Institutional Review Board and all subjects provided written consent prior to imaging. Healthy volunteers were recruited (n=11, 1 female, mean age 34 ± 12 years) for brain MRI on a 3T scanner (HDxt, GE Healthcare, Waukesha, WI, USA) using an 8-channel brain receive coil. All subjects were instructed to avoid caffeine or alcohol intake 24 hours prior to MRI. In this study, SI units are used and magnetic susceptibility is relative to water (CSF) unless otherwise stated.

5.4.1 Data Acquisition

5.4.1.1 Caffeine Experiment

MRI was performed before and 25 min after the oral administration of 200 mg caffeine using a protocol similar to that described in (27). Briefly, the protocol consists of an anatomical T1w BRAVO sequence, a 3D fast spin echo (FSE) arterial spin labeling (ASL) sequence to measure CBF, and a 3D multi-echo spoiled gradient echo (SPGR) sequence to measure the local fields, from which QSM maps were calculated using the MEDI algorithm (42,43).

The 3D FSE ASL sequence parameters were: 1500 ms labeling period, 1525 ms post-label delay, spiral sampling of 8 interleaves with 512 readout points per leaf, 62.5 kHz

readout bandwidth, 20 cm FOV, 3 mm isotropic resolution, 35 axial slices, 10.5 ms TE, 4796 ms TR, 3 signal averages, and 6 min scan time.

The 3D SPGR sequence parameters included: 7 equally spaced echoes, 4.3 ms first TE, 7.9 ms echo spacing , 56.6 ms TR, 0.52 mm in-plane resolution, 2 mm slice thickness, identical volume coverage as the 3D FSE ASL sequence, 62.5 kHz readout bandwidth, 15^{o} flip angle, and 7 min scan time. The pulse sequence was flow-compensated in all three directions (44).

T1 BRAVO sequence parameters were: 2.92 ms TE, 7.68 ms TR, 450 ms prep time, 1.2 mm isotropic resolution and identical volume coverage as the 3D FSE ASL sequence, ±19.5 kHz readout bandwidth, 15^{o} flip angle, and 2 min scan time.

5.4.1.2 Hyperventilation Experiment

Subjects from the caffeine experiment were asked to return within a week and coached to hyperventilate at a certain pace (1 inhale and exhale every 2~3 seconds) before the scans. MRI was performed before and during hyperventilation using a protocol consisting of a 3D FSE ASL sequence, and a 3D SPGR sequence. After the base line scan, the subjects were instructed to hyperventilate. The scans of challenged state started 30 seconds into the hyperventilation (HV1). The hyperventilation period lasts about 7 min. Proper restrictive padding inside the head coil was used to minimize head motion. Extensive monitoring of subject compliance was not performed during this study in healthy

subjects but may be advisable for patient studies. The compliance of a broader population will be studied in our future work.

The volume coverage and scanning parameters for 3D spoiled GRE and 3D FSE ASL acquisitions were similar to those used in the caffeine experiment except the voxel size were increased to 1.2 mm and 3.5 mm isotropic, respectively, to shorten the scan time to 3 min each and improve subject's comfort during hyperventilation.

After the scan, subjects were asked to exit the scanner, rest for 30 min, and return to the scanner for a repeat hyperventilation experiment (HV2).

5.4.1.3 Signal to Noise Ratio (SNR) Measurement

For quantification of SNR, two 3D FSE ASL and two 3D SPGR sequence were performed consecutively on two of the 11 subjects using the parameters from the caffeine protocol. The scans were repeated with parameters used in HV protocol.

5.4.2 Image Processing

5.4.2.1 CBF and QSM Reconstruction

CBF maps (ml/100g/min) were generated from the ASL data using the FuncTool software package (GE Healthcare, Waukesha, WI, USA). QSM maps were calculated from GRE magnitude and phase data. A voxel-based adaptive quadratic-fit of the phase was used to obtain robust total field estimation in the presence of bulk flow (21,44), followed by

spatial unwrapping (45) and background field removal using a projection onto dipole fields method (46) to obtain the local field map. QSM was computed from the local field map using the Morphology Enabled Dipole Inversion (MEDI) algorithm (18,20,21,47). Susceptibility values in QSMs were referenced to the susceptibility of water (defined in this study as the mean susceptibility of cerebrospinal fluid (CSF) measured in the CSF masks, see below). All images were co-registered and interpolated to the resolution of the QSM maps using the FSL FLIRT algorithm (48,49).

5.4.2.2 Numerical Simulation

GM and WM binary masks from one of the subjects were used for the simulation (See below). OEF_{base} and OEF_{chal} were set to 35 and 45% respectively for both GM and WM. χ_{base} and CBF_{base} are set to 20ppb and -10 ppb, 60 and 30 ml/100g/min for GM and WM respectively. χ_{chal} and CBF_{chal} were then calculated through Eq. 5.6. Gaussian noise calculated using SNR of 10 and GM values were added to the entire χ and CBF maps. $CMRO_2$ maps were solved with/without constraints. λ is chosen based on an average value obtained by L-Curve analysis (37). The simulation was repeated for 10 times. SNR of the simulation was calculated by dividing the mean over the standard deviation of over the GM Mask.

5.4.2.3 SNR Measurement

SNR was calculated using the following equation (50):

$$SNR = \sqrt{2}\frac{S}{\sigma}$$

Where S is mean pixel intensity value in a ROI on one of the original images; σ is the standard deviation of pixel intensity in a ROI on the subtracted images. SNR was calculated in putamen on ASL control images, GRE first echo magnitude images, and in HV $CMRO_2$ maps reconstructed with /without constraints.

5.4.3 Statistical Analysis

Cortical grey matter (CGM), white matter (WM), and CSF masks were created using the FSL FAST algorithm (51) on T1 BRAVO images covering the supratentorial brain parenchyma from the vertex to the superior aspect of the cerebellum. These masks were visually confirmed by a neuroradiologist (A.G.) for anatomical accuracy. The CGM masks with average volume of 246.4 ± 15.9 cm^3 were further segmented by the same neuroradiologist into the bilateral anterior (ACA), middle (MCA) and posterior cerebral artery (PCA) vascular territories (VT) .

For each ROI, the mean and standard deviation of QSM, CBF, OEF, and $CMRO_2$ values were measured for both the caffeine and hyperventilation method. Paired-sample t-tests were performed to assess the differences in QSM, CBF, and OEF in the CGM before and after the caffeine and hyperventilation challenge across the subjects.

Bland-Altman plots and paired sample t-tests were performed to compare regional $CMRO_2$ and OEF obtained in the VTs using caffeine and hyperventilation challenge, as well as those obtained with repeated hyperventilation experiments.

P values of less than 0.05 were considered to indicate statistical significance. All data were expressed as mean ± standard deviation.

5.5 RESULTS

All MRI data were acquired successfully. No obvious motion artifacts were observed in the QSM and CBF maps. The protocol time were 67 ± 19 (including a 30 minute waiting time), 15 ± 1.5, and 15 ± 1.6 minutes for caffeine, HV1 and HV2 scans, respectively. In numerical simulation, the proposed constraint method improved SNR from 1.90 ± 0.04 to 8.60 ± 0.83 in GM (Fig. 5.1). SNR acquired using the caffeine and HV protocols were 143.9 ± 75.6 and 140.5 ± 33.2 respectively for ASL control images, 28.4 ± 0.47 and 34.7 ± 0.74 for GRE. In subjects, the constrained reconstruction improved SNR in the HV $CMRO_2$ maps from 2.16 ± 1.23 to 5.78 ± 1.36 ($p<0.01$).

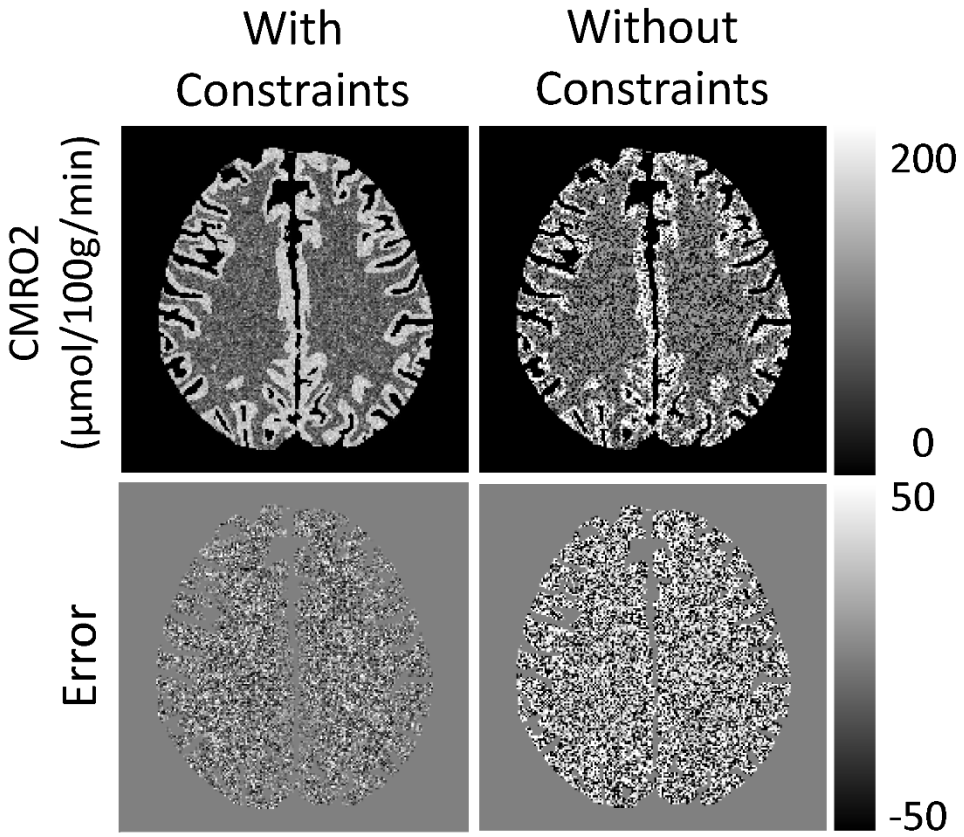

Figure 5.1. Numerical simulation results reconstructed with and without constraints (SNR=10). The proposed constrained method improves SNR of the $CMRO_2$ images.

For the reconstruction, λ (Eq. 5.7) was chosen to be 2.5×10^4. Figure 5.2 shows histograms of OEF and $CMRO_2$ maps of a healthy subject reconstructed with and without constraints. Figure 5.1 and 5.2 demonstrated that the use of physiological constraints and pre-conditioning achieved substantial reduction of noise and extreme values in $CMRO_2$ and OEF maps compared to previous unconstrained methods (27).

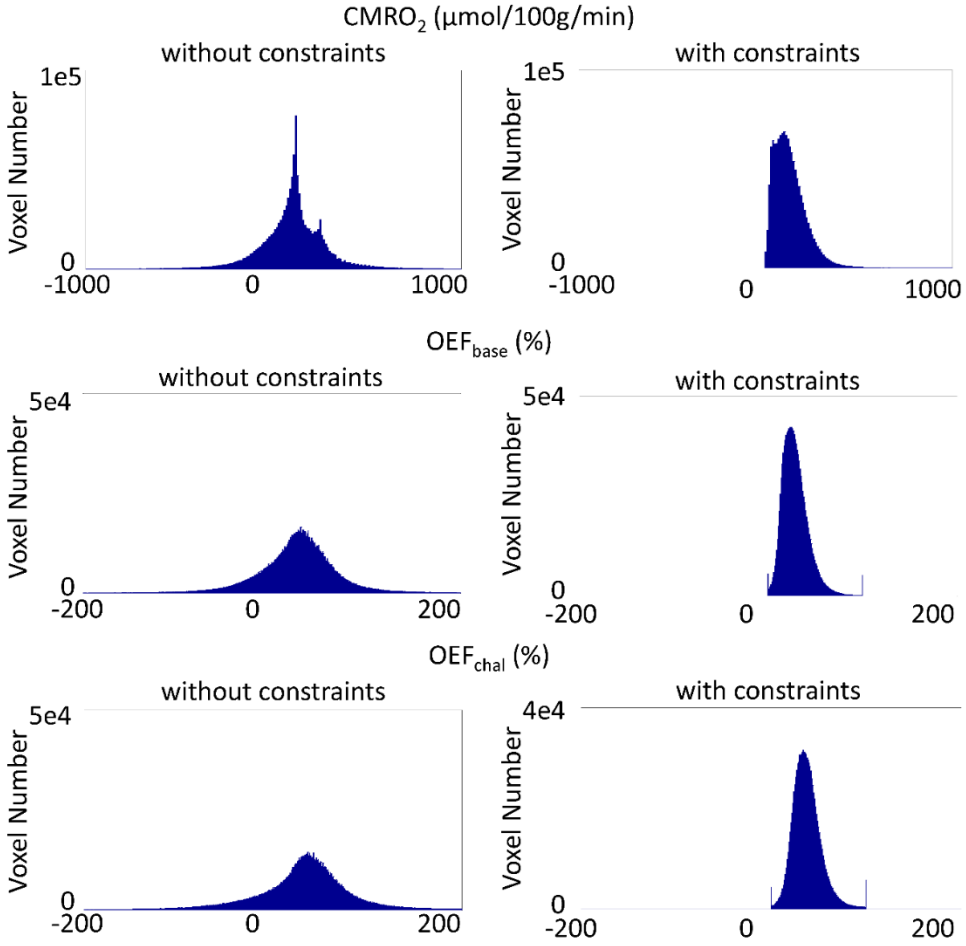

Figure 5.2. Histograms of OEF and $CMRO_2$ maps of a healthy subject reconstructed with and without constraints. Physiologically improbable OEF values (>1 or <0) were eliminated.

Compared to baseline, CGM susceptibility increased by 3.8 ± 1.11 ppb ($p<0.01$), 4.38 ± 1.71 ppb ($p<0.01$), 4.96 ± 1.25 ppb ($p<0.01$), and CBF decreased by 16.3 ± 7.0 ml/100g/min ($p<0.01$), 18.8 ± 5.3 ml/100g/min ($p<0.01$), and 18.5 ± 4.4 ml/100g/min ($p<0.01$), for caffeine, first and second hyperventilation experiments, respectively. This corresponded to a baseline $CMRO_2$ of 149 ± 16 µmol/100g/min, 153 ± 19 µmol/100g/min,

and 150 ± 20 μmol/100g/min with an OEF increase from 33.6 ± 3.4% to 39.9 ± 4.8% ($p<0.01$), 32.3 ± 3.3% to 43.6 ± 6.2% ($p<0.01$), and 34.1 ± 3.8% to 42.8 ± 6.8% ($p<0.01$) in CGM. VT and WM ROI measurements of $CMRO_2$ and OEF are listed in Table 5.1.

Figure 5.3 shows $CMRO_2$ maps in one healthy volunteer across the brain obtained from caffeine, HV1 and HV2 experiments, as well as its corresponding T1 BRAVO images. The $CMRO_2$ maps show good consistency across different scans and good gray-white matter contrast in reasonable agreement with anatomical images.

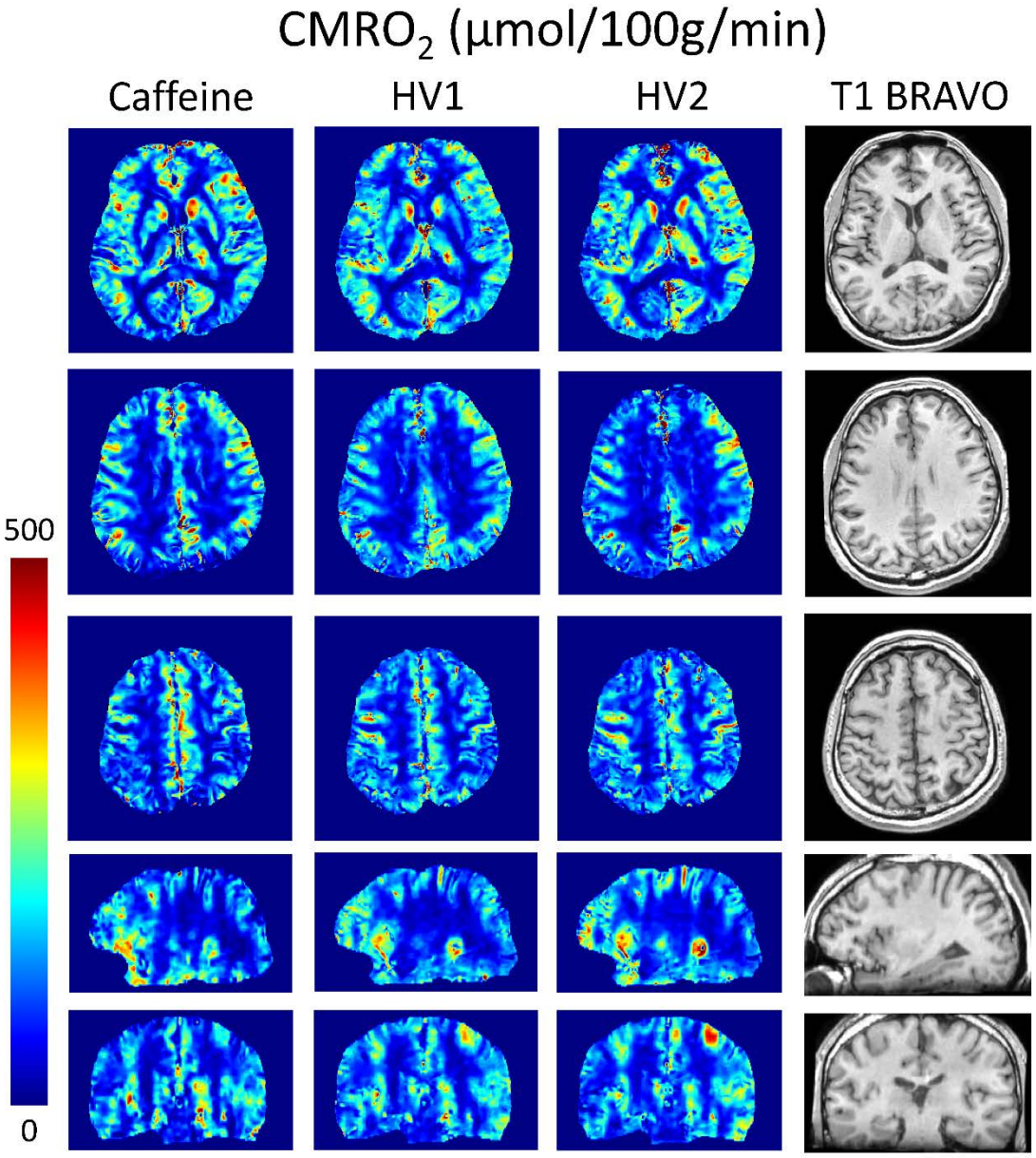

Figure 5.3. An example of volumetric $CMRO_2$ maps of a healthy subject generated from the caffeine and HV1 and HV2 scans using the proposed method with constraints. The corresponding T1 BRAVO images are shown on the right. The $CMRO_2$ maps show good consistency across scans and have a similar degree of good gray-white matter contrast as the anatomical T1 BRAVO images.

Figure 5.4 shows baseline and challenged OEF, $CMRO_2$, χ_{nb} maps and T1 BRAVO images from the 3 different experiments. OEF maps also demonstrate good consistency among experiments. Global increase in OEF after vaso-constrictive challenge can be appreciated. In contrast to $CMRO_2$ maps, OEF maps lose some of the gray-white matter contrast and have smoother appearance.

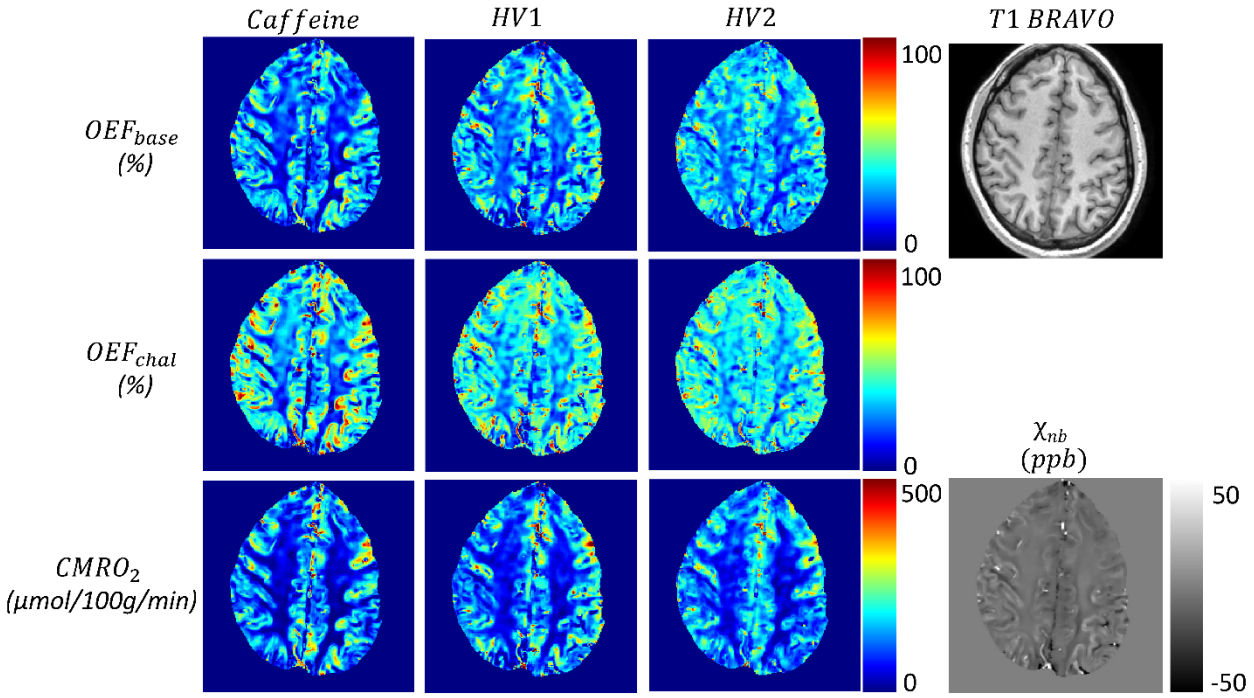

Figure 5.4. An example of OEF, $CMRO_2$, and χ_{nb} maps in a second subject. The corresponding T1 BRAVO images are shown on the right.

Figure 5.5 showed Bland-Altman plots comparing VT ROI measurements of $CMRO_2$ and OEF maps between different experiments. All six comparisons show good agreements. OEF_{chal} between caffeine and HV1 experiments show a difference of 3.4%

(p<0.05). Small bias (<4% of the average of the two measurements) are detected in other comparisons without statistical significance (p>0.05).

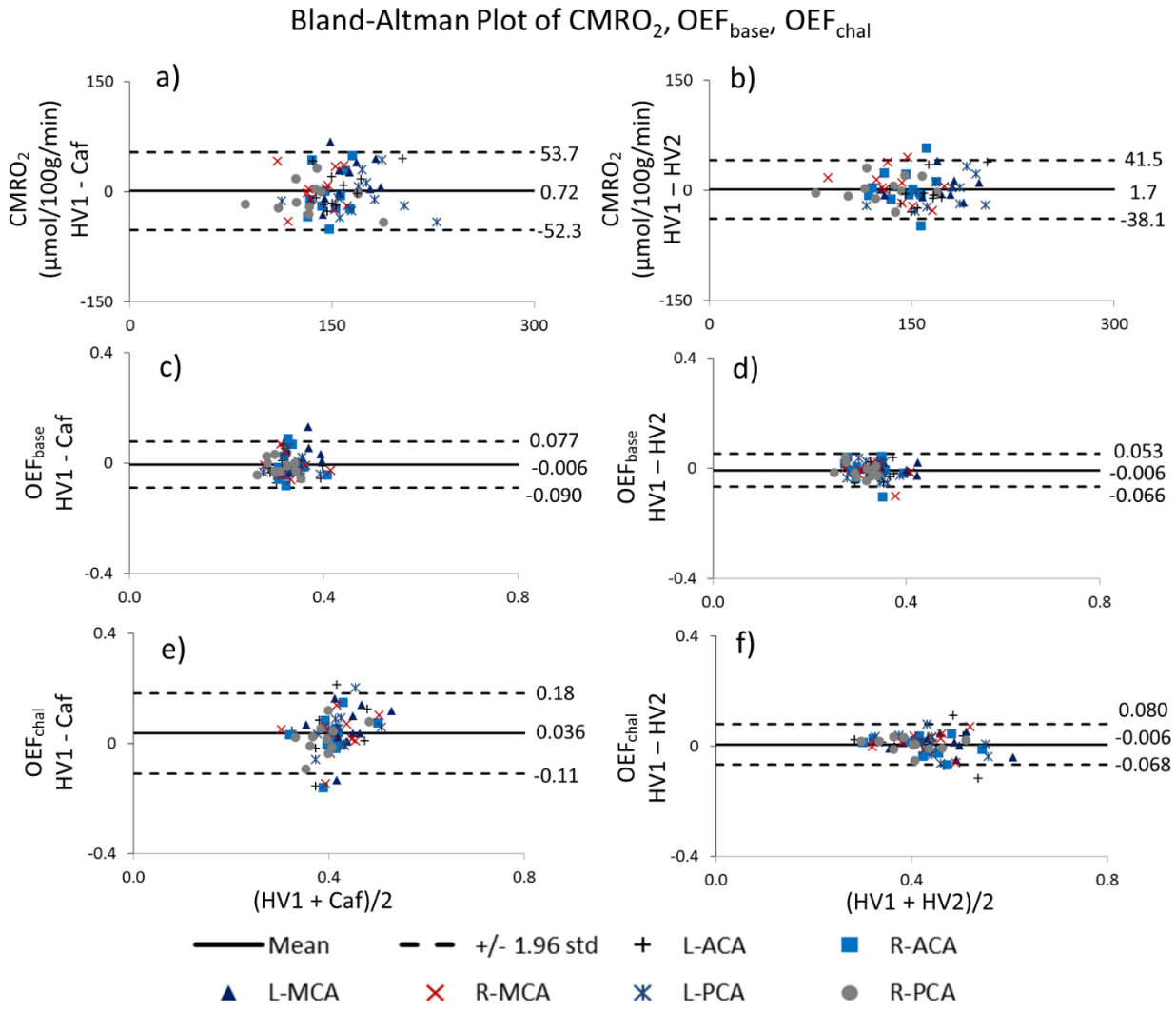

Figure 5.5. Bland-Altman plots comparing $CMRO_2$ and OEF maps between HV1 and caffeine scans, and between HV1 and HV2 scans. Plot e show 3.4% bias in OEF (P<0.05). Other plots shows small bias (<4% of the average of the two measurements) with no statistical significance (P>0.05).

Table 5.1. $CMRO_2$ (μmol/100g/min) and OEF (%) measurements within VT and WM ROIs reconstructed with/without constraint across subjects (mean ± std).

	OEF_{base}						OEF_{chal}						$CMRO_2$					
	Caffeine		HV 1		HV 2		Caffeine		HV 1		HV 2		Caffeine		HV 1		HV 2	
	w/o C	C	w/o C	C	w/o C	C	w/o C	C	w/o C	C	w/o C	C	w/o C	C	w/o C	C	w/o C	C
ACA	38.8 ± 9.9	33.1 ± 4.2	35.3 ± 7.6	31.9 ± 3.8	38.0 ± 9.6	32.8 ± 4.8	48.3 ± 12.0	39.1 ± 5.1	44.6 ± 10.8	42.4 ± 6.4	49.6 ± 12.7	42.5 ± 8.2	160 ± 33	151 ± 17	152 ± 33	151 ± 24	158 ± 32	152 ± 22
MCA	37.2 ± 9.0	34.0 ± 3.8	35.0 ± 6.8	34.5 ± 4.2	37.2 ± 10.7	34.6 ± 4.5	47.4 ± 11.1	40.4 ± 5.4	44.7 ± 9.2	44.8 ± 6.9	47.3 ± 12.7	43.4 ± 6.9	146 ± 32	146 ± 20	142 ± 23	155 ± 27	143 ± 36	150 ± 30
PCA	33.0 ± 11.3	33.1 ± 3.6	31.0 ± 8.5	31.6 ± 3.1	30.9 ± 10.3	32.6 ± 4.1	41.3 ± 12.2	38.9 ± 3.8	40.7 ± 10.6	41.9 ± 5.9	40.2 ± 13.1	41.5 ± 7.2	143 ± 47	158 ± 39	139 ± 30	150 ± 34	136 ± 28	150 ± 32
WM	35.4 ± 5.2	30.5 ± 3.4	29.6 ± 4.8	31.1 ± 2.8	29.4 ± 5.1	32.3 ± 3.3	42.9 ± 9.0	36.0 ± 5.2	37.2 ± 7.0	41.0 ± 6.3	35.8 ± 6.6	41.0 ± 7.2	100 ± 13	107 ± 17	90 ± 12	114 ± 11	87 ± 14	113 ± 9

w/o C: without constrained

C: constrained

ACA: Anterior Cerebral Artery

MCA: Middle Cerebral Artery

PCA: Posterior Cerebral Artery

WM: White Matter

Table 5.2. $CMRO_2$ measurements in gray matter reported in previous studies.

$CMRO_2$ (μmol/100g/min)	**Reference**
155 ± 39	Bulte et. al., NeuroImage 2012 (7)
145 ± 30	Gauthier et. al., NeuroImage 2012 (8)
184 ± 45	Wise et. al., NeuroImage 2013 (9)

5.6 DISCUSSION

Our preliminary results in young healthy subjects demonstrate the feasibility of fast QSM-based $CMRO_2$ mapping using hyperventilation. Advantages of hyperventilation over other vascular challenges such as caffeine (52), acetazolamide, or hyperoxia (7-9) include simple setup, rapid vascular response, and an excellent safety profile, although it might require subject coaching prior to scanning and can induce minor discomfort. Compared to caffeine challenge, hyperventilation shortened the total time of the $CMRO_2$ mapping protocol from an average of 67 min (including a 30 minute waiting time) to 15 min and provided images that are visually comparable, although no direct quantitative comparison was performed in this study. Hyperventilation demonstrated good reproducibility in combination with ease of implementation, suggesting that $CMRO_2$ mapping based on QSM and hyperventilation may be an effective tool in the study and management of cerebrovascular diseases such as acute ischemic stroke or chronic hypoperfusion.

In this study, we used hyperventilation to induce vasoconstriction. Voluntary hyperventilation in our healthy subjects was found to produce an average of 31% reduction in CBF on average in CGM, which was slightly more effective than caffeine (27% reduction) and similar to previously reported values (29,30). For sick patients with difficulty to perform voluntary hyperventilation, the widely available ventilator can be used. While hyperventilation induced vasoconstriction varies with patients, such variation does not affect $CMRO_2$ mapping as long as sufficient vasoconstriction is induced. The $CMRO_2$ values measured in CGM using hyperventilation in this study were found to agree well

with those obtained in prior studies using caffeine challenge (27). These values were also similar to those reported in the existing MRI literature (7-9) (Table 5.2).

The QSM-based $CMRO_2$ technique described here may provide several unique advantages over previous $CMRO_2$ mapping approaches. One of the major challenges in "calibrated fMRI" is the calibration procedure and modeling, which was required in the R2* modeling for [dHb] (53,54). QSM solves the field-to-susceptibility source inverse problem based on Maxwell's equation using the phase of the GRE data. Magnetic susceptibility measured on QSM is a physical quantity that is independent of imaging parameters and has a well-defined quantitative linear relationship with blood oxygenation (16,17,27). Therefore, calibration between relaxation rates (R2 and R2*) and blood oxygenation (53) is not needed for the well-defined quantitative relationship between susceptibility and blood oxygenation. Gas manipulation equipment to resolve multiple empirical parameters in calibrated fMRI approaches is not needed for QSM based approach. By separating susceptibility contribution of blood and tissue, QSM-based $CMRO_2$ technique also produces χ_{nb} maps (Fig. 5.4), which may be used for measuring the susceptibility in tissues (e.g. iron or myelin) when the blood contribution cannot be neglected. Additionally, QSM reduces blooming artifacts inherent in R2* and R2' by deconvolving the field. Finally, there are additional practical advantages to the hyperventilation challenge. Hypercapnia/hyperoxia gas manipulation is not as easily implemented as hyperventilation. Though acetazolamide vascular challenge is generally well-tolerated, it is contraindicated in certain groups of patients and may produce adverse side effects.

In $CMRO_2$ and OEF mapping, noise in MRI data leads to spatially fluctuating errors and extreme values because of the poor condition of the system matrix (Eq. 5.6 and Fig. 5.1). Oxygen consumption induced MRI signal changes in brain tissue are invariably small. Accordingly, it is important to use prior knowledge to improve the system matrix condition, or more precisely to find a maximum a posteriori estimate in the Bayesian statistical framework (Eq. 5.7). In this work, we used the prior knowledge that 1) OEF should be within [0,1], 2) the global $CMRO_2$ estimated from the map should equal that estimated from the draining veins, and 3) the search for the maximal posterior probability (Eq. 5.7) should start reasonably (precondition). Compared to our prior result, this constrained preconditioned search has resulted in much improved SNR in $CMRO_2$ and OEF (Fig. 5.1).

In this study, global OEFs were estimated from the straight sinus and global CBFs were estimated by taking the sum of all voxels in CBF maps covering the whole brain. Our measurements, $OEF_{base}^{v} = 26.5 \pm 3.1\%$ and $CBF_{mean\_base} = 51.6 \pm 5.8 ml/100g/min$ agree well with global OEF and global CBF estimated from GRE phase and phase contrast in the superior sagittal sinus reported in previous studies (55,56). Recent studies showed that blood flow challenges such as hyper-, hypoxia, and hyper-, hypocapnia, can change global $CMRO_2$ by 5 to 20% (57-61). Here we observed a small change of -4.31 ± 11.4%, -3.43 ± 11.0%, and -3.69 ± 11.73% following caffeine, HV1 and HV2 challenges, respectively, in global $CMRO_2$ as measured in the straight sinus ($p>0.05$). These values were not statistically different in our cohort. Nevertheless, we assumed that the local $CMRO_2$ in each brain voxel changes by the same relative amount as the global $CMRO_2$ in the reconstruction. The spatial and temporal variation of $CMRO_2$ during hyperventilation

can be a source of error and warrants further investigation. In the cases of acute infarction or active bleeding, blood might leave the vasculature and pool inside tissue. This phenomenon might need to be considered in the mass conservation for accurate estimation of global $CMRO_2$ from large draining veins. In future studies, an additional phase contrast acquisition can be used for a more direct measurement of blood flow in the straight sinus to obtain global CBF (55,56).

One of the limitations in our study is the relatively short (30 seconds) HV time before the HV ASL scan. In order to estimate the onset of the CBF steady state, we performed additional scans in two volunteers from this study. With our 3D ASL sequence we were able to obtain a low-resolution whole brain CBF map every 50 seconds. After baseline scans, the subjects were asked to start hyperventilating as in the study while ASL scans acquired simultaneously for a total of 250 seconds. The data showed that steady state was reached by the second scan and remained there until the end of scanning/hyperventilation, with the first scan showing a CBF that was approximately 35% higher than the steady-state value. The 3D ASL sequence used in this study is a stack-of-spirals acquisition that repeatedly returns to the center of k-space throughout the acquisition. Considering the scan time of 3 minutes as used in this study, approximately 85% of HV CBF data was acquired during the steady state, while QSM was acquired well after the steady state was reached. Hence the assumption of a steady state brain condition is valid.

The lack of Hct measurements is another limitation of this preliminary feasibility study. We assumed $\mathrm{Hct}_{ss} = 0.47$ and calculated Hct_{tissue} as $0.759\mathrm{Hct}_{ss}$ as measured in

(31). We have quantified the maximum $CMRO_2$ estimation error caused by inter-subject variability of Hct_{ss} by repeating the calculations for both the lower (0.38) and upper bound (0.52) of the expected human Hct_{ss} range. For the cortical GM, the maximum difference between the $CMRO_2$ value for Hct=0.47 and the two $CMRO_2$ values obtained in this manner was 2.4 ± 1.1% (n=11). The ratio between Hct_{ss} and Hct_{tissue} may vary spatially and among subjects. The potential error due to such variation warrants further investigation.

In this work HV scans had lower resolution compared to caffeine scans. The tradeoffs in $CMRO_2$ and OEF maps due to the reduced spatial resolution are partial volume error in CBF and QSM maps which can propagate into $CMRO_2$ and OEF images. However, in this study we did not perform an explicit direct comparison between different spatial resolutions in the same subject. Further studies are warranted to investigate the partial volume error in the proposed method.

Our OEF was slightly lower (2.5%) in WM than in CGM in all three experiments. This observed discrepancy may be attributed to the lower CBF changes detected in WM than the changes in CGM after caffeine and HV challenges (-6.0±4.3ml/100g/min vs -17.9±5.53ml/100g/min, $p<0.01$). The small absolute CBF change and the known challenges of accurately quantifying CBF in WM with ASL MRI perfusion make OEFs in these regions more difficult to resolve. Our protocol was based on a routine clinical protocol used at our institution. By modifying the protocol according to the recent white paper by Alsop et al (62), SNR could potentially be improved at a cost of scan time increase. This discrepancy may also be attributed to the challenges associated with accurately mapping CBV in white matter. For this feasibility study, CBV was estimated from CBF

using an empirical relationship derived from normative PET data and the Grubb's exponent of 0.38, which can be a source of error. This limitation may be addressed by direct measurements of CBV using technique such as dynamic study with contrast agent (63,64), or by non-contrast MRI with detailed vascular signal modeling such as Vascular Space Occupancy (VASO)(65-67), fMRI with multiple inversion times (68), or quantitative BOLD (69,70). CBVv / CBV_{total} was assumed to be 77% at baseline (32). We also processed the data with a CBVv / CBV_{total} of 50% as assumed in a previous study (27) and found a relatively small difference of 1.0 ± 1.4% in $CMRO_2$ for cortical GM across subjects.

5.7 CONCLUSION

Hyperventilation is a feasible, reproducible and efficient vasoconstrictive challenge for QSM based quantitative $CMRO_2$ mapping in healthy subjects with good reproducibility and offers 4-fold protocol time reduction compared to using caffeine as a challenge. Constrained optimization within physical range of OEF provides substantial reduction of noise errors in $CMRO_2$ and OEF maps. The applicability of this protocol for a general patient population remains to be investigated.

5.8 APPENDIX

Calculation of heme ($[H]$) in tissue blood micro-vasculature.

$$[H] = 4Hct_{tissue}\,\frac{\rho_{RBC,Hb}}{M_{Hb}} = 7.53\ \mu\text{mol/ml}$$

where $Hct_{tissue} = 0.357$, $\rho_{RBC,Hb} = 0.34 g/ml$ is mass concentration of Hb in a red blood cell (71), $M_{Hb} = 64450 \times 10^{-6}\ g/\mu mol$ is the the molar mass of dHb (72), 4 account of 4 heme per Hb molecule.

Calculation of Volume Fraction of Hb in RBC δ_{Hb}

δ_{Hb} is estimated from Hb mass concentration in a red blood cell ($\rho_{RBC,Hb} = 0.34 g/ml$)(71), and Hb density in pure aggregate ($\rho_{Hb} = 1.335\ g/ml$)(73)

$$\delta_{\mathrm{Hb}} = \frac{\rho_{RBC,Hb}}{\rho_{Hb}} = 0.255$$

Calculation of Volume Susceptibility of Oxyhemoglobin $\mathrm{X_{oHb}}$ and DeoxyHemoglobin $\mathrm{X_{dHb}}$

The volume susceptibility of Oxyhemoglobin $\mathrm{X_{oHb}}$ relative to water is estimated from the reported mass susceptibility of globin relative to vacuum ($-0.587 \times 10^{-6}\ ml/g$) (CGS unit) (73,74), and Hb density in pure aggregate ($\rho_{Hb} = 1.335\ g/ml$) (73).

$$\mathrm{X_{oHb}} = -4\pi\rho_{Hb}(0.587 \times 10^{-6}\ ml/g) - (-9035\ ppb) = -813 ppb$$

where 4π is for unit conversion from cgs to si, $-9035\ ppb$ is water volume susceptibility relative to vacuum (75).

REFERENCES

1. Derdeyn CP, Videen TO, Yundt KD, Fritsch SM, Carpenter DA, Grubb RL, Powers WJ. Variability of cerebral blood volume and oxygen extraction: stages of cerebral haemodynamic impairment revisited. Brain : a journal of neurology 2002;125(Pt 3):595-607.

2. Gupta A, Chazen JL, Hartman M, Delgado D, Anumula N, Shao H, Mazumdar M, Segal AZ, Kamel H, Leifer D, Sanelli PC. Cerebrovascular reserve and stroke risk in patients with carotid stenosis or occlusion: a systematic review and meta-analysis. Stroke; a journal of cerebral circulation 2012;43(11):2884-2891.

3. Gupta A, Baradaran H, Schweitzer AD, Kamel H, Pandya A, Delgado D, Wright D, Hurtado-Rua S, Wang Y, Sanelli PC. Oxygen extraction fraction and stroke risk in patients with carotid stenosis or occlusion: a systematic review and meta-analysis. AJNR American journal of neuroradiology 2014;35(2):250-255.

4. Pauling L, Coryell CD. The Magnetic Properties and Structure of Hemoglobin, Oxyhemoglobin and Carbonmonoxyhemoglobin. Proceedings of the National Academy of Sciences of the United States of America 1936;22(4):210-216.

5. Ogawa S, Lee TM, Kay AR, Tank DW. Brain magnetic resonance imaging with contrast dependent on blood oxygenation. Proceedings of the National Academy of Sciences of the United States of America 1990;87(24):9868-9872.

6. Bolar DS, Rosen BR, Sorensen AG, Adalsteinsson E. QUantitative Imaging of eXtraction of oxygen and TIssue consumption (QUIXOTIC) using venular-targeted velocity-selective spin labeling. Magnetic resonance in medicine : official journal of the Society of Magnetic Resonance in Medicine / Society of Magnetic Resonance in Medicine 2011;66(6):1550-1562.

7. Bulte DP, Kelly M, Germuska M, Xie J, Chappell MA, Okell TW, Bright MG, Jezzard P. Quantitative measurement of cerebral physiology using respiratory-calibrated MRI. NeuroImage 2012;60(1):582-591.

8. Gauthier CJ, Hoge RD. Magnetic resonance imaging of resting OEF and CMRO(2) using a generalized calibration model for hypercapnia and hyperoxia. NeuroImage 2012;60(2):1212-1225.

9. Wise RG, Harris AD, Stone AJ, Murphy K. Measurement of OEF and absolute CMRO2: MRI-based methods using interleaved and combined hypercapnia and hyperoxia. NeuroImage 2013;83:135-147.

10. An H, Ford AL, Chen Y, Zhu H, Ponisio R, Kumar G, Shanechi AM, Khoury N, Vo KD, Williams J, Derdeyn CP, Diringer MN, Panagos P, Powers WJ, Lee JM, Lin W. Defining the ischemic penumbra using magnetic resonance oxygen metabolic index. Stroke; a journal of cerebral circulation 2015;46(4):982-988.

11. An H, Lin W. Impact of intravascular signal on quantitative measures of cerebral oxygen extraction and blood volume under normo- and hypercapnic conditions using an asymmetric spin echo approach. Magnetic resonance in medicine : official journal of the Society of Magnetic Resonance in Medicine / Society of Magnetic Resonance in Medicine 2003;50(4):708-716.

12. Ulrich X, Yablonskiy DA. Separation of cellular and BOLD contributions to T2* signal relaxation. Magnetic resonance in medicine : official journal of the Society of Magnetic Resonance in Medicine / Society of Magnetic Resonance in Medicine 2015:doi: 10.1002/mrm.25610.

13. Wang X, Sukstanskii AL, Yablonskiy DA. Optimization strategies for evaluation of brain hemodynamic parameters with qBOLD technique. Magnetic resonance in medicine : official journal of the Society of Magnetic Resonance in Medicine / Society of Magnetic Resonance in Medicine 2013;69(4):1034-1043.

14. Yablonskiy DA, Haacke EM. Theory of NMR signal behavior in magnetically inhomogeneous tissues: the static dephasing regime. Magnetic resonance in medicine : official journal of the Society of Magnetic Resonance in Medicine / Society of Magnetic Resonance in Medicine 1994;32(6):749-763.

15. Li J, Chang S, Liu T, Wang Q, Cui D, Chen X, Jin M, Wang B, Pei M, Wisnieff C, Spincemaille P, Zhang M, Wang Y. Reducing the object orientation dependence of

susceptibility effects in gradient echo MRI through quantitative susceptibility mapping. Magnetic resonance in medicine : official journal of the Society of Magnetic Resonance in Medicine / Society of Magnetic Resonance in Medicine 2012;68(5):1563-1569.

16. Jain V, Abdulmalik O, Propert KJ, Wehrli FW. Investigating the magnetic susceptibility properties of fresh human blood for noninvasive oxygen saturation quantification. Magnetic resonance in medicine : official journal of the Society of Magnetic Resonance in Medicine / Society of Magnetic Resonance in Medicine 2012;68(3):863-867.

17. Spees WM, Yablonskiy DA, Oswood MC, Ackerman JJ. Water proton MR properties of human blood at 1.5 Tesla: magnetic susceptibility, T(1), T(2), T*(2), and non-Lorentzian signal behavior. Magnetic resonance in medicine : official journal of the Society of Magnetic Resonance in Medicine / Society of Magnetic Resonance in Medicine 2001;45(4):533-542.

18. de Rochefort L, Liu T, Kressler B, Liu J, Spincemaille P, Lebon V, Wu J, Wang Y. Quantitative susceptibility map reconstruction from MR phase data using bayesian regularization: validation and application to brain imaging. Magnetic resonance in medicine : official journal of the Society of Magnetic Resonance in Medicine / Society of Magnetic Resonance in Medicine 2010;63(1):194-206.

19. Kressler B, de Rochefort L, Liu T, Spincemaille P, Jiang Q, Wang Y. Nonlinear regularization for per voxel estimation of magnetic susceptibility distributions from MRI field maps. IEEE transactions on medical imaging 2010;29(2):273-281.

20. Liu J, Liu T, de Rochefort L, Ledoux J, Khalidov I, Chen W, Tsiouris AJ, Wisnieff C, Spincemaille P, Prince MR, Wang Y. Morphology enabled dipole inversion for quantitative susceptibility mapping using structural consistency between the magnitude image and the susceptibility map. NeuroImage 2012;59(3):2560-2568.

21. Liu T, Wisnieff C, Lou M, Chen W, Spincemaille P, Wang Y. Nonlinear formulation of the magnetic field to source relationship for robust quantitative susceptibility mapping. Magnetic resonance in medicine : official journal of the Society of Magnetic Resonance in Medicine / Society of Magnetic Resonance in Medicine 2013;69(2):467-476.

22. Haacke EM, Lai S, Reichenbach JR, Kuppusamy K, Hoogenraad FG, Takeichi H, Lin W. In vivo measurement of blood oxygen saturation using magnetic resonance imaging: a direct validation of the blood oxygen level-dependent concept in functional brain imaging. Hum Brain Mapp 1997;5(5):341-346.

23. Fan AP, Benner T, Bolar DS, Rosen BR, Adalsteinsson E. Phase-based regional oxygen metabolism (PROM) using MRI. Magnetic resonance in medicine : official journal of the Society of Magnetic Resonance in Medicine / Society of Magnetic Resonance in Medicine 2012;67(3):669-678.

24. Li C, Langham MC, Epstein CL, Magland JF, Wu J, Gee J, Wehrli FW. Accuracy of the cylinder approximation for susceptometric measurement of intravascular oxygen saturation. Magnetic resonance in medicine : official journal of the Society of Magnetic Resonance in Medicine / Society of Magnetic Resonance in Medicine 2012;67(3):808-813.

25. Fan AP, Bilgic B, Gagnon L, Witzel T, Bhat H, Rosen BR, Adalsteinsson E. Quantitative oxygenation venography from MRI phase. Magnetic resonance in medicine : official journal of the Society of Magnetic Resonance in Medicine / Society of Magnetic Resonance in Medicine 2014;72(1):149-159.

26. Wehrli FW, Rodgers ZB, Jain V, Langham MC, Li C, Licht DJ, Magland J. Time-resolved MRI oximetry for quantifying CMRO(2) and vascular reactivity. Academic radiology 2014;21(2):207-214.

27. Zhang J, Liu T, Gupta A, Spincemaille P, Nguyen TD, Wang Y. Quantitative mapping of cerebral metabolic rate of oxygen (CMRO) using quantitative susceptibility mapping (QSM). Magnetic resonance in medicine : official journal of the Society of Magnetic Resonance in Medicine / Society of Magnetic Resonance in Medicine 2014.

28. Vagal AS, Leach JL, Fernandez-Ulloa M, Zuccarello M. The acetazolamide challenge: techniques and applications in the evaluation of chronic cerebral ischemia. AJNR American journal of neuroradiology 2009;30(5):876-884.

29. Diringer MN, Videen TO, Yundt K, Zazulia AR, Aiyagari V, Dacey RG, Jr., Grubb RL, Powers WJ. Regional cerebrovascular and metabolic effects of hyperventilation after severe traumatic brain injury. Journal of neurosurgery 2002;96(1):103-108.

30. Kety SS, Schmidt CF. The Effects of Active and Passive Hyperventilation on Cerebral Blood Flow, Cerebral Oxygen Consumption, Cardiac Output, and Blood Pressure of Normal Young Men. The Journal of clinical investigation 1946;25(1):107-119.

31. Sakai F, Nakazawa K, Tazaki Y, Ishii K, Hino H, Igarashi H, Kanda T. Regional cerebral blood volume and hematocrit measured in normal human volunteers by single-photon emission computed tomography. Journal of cerebral blood flow and metabolism : official journal of the International Society of Cerebral Blood Flow and Metabolism 1985;5(2):207-213.

32. An H, Lin W. Cerebral venous and arterial blood volumes can be estimated separately in humans using magnetic resonance imaging. Magnetic resonance in medicine : official journal of the Society of Magnetic Resonance in Medicine / Society of Magnetic Resonance in Medicine 2002;48(4):583-588.

33. Weisskoff RM, Kiihne S. MRI susceptometry: image-based measurement of absolute susceptibility of MR contrast agents and human blood. Magnetic resonance in medicine : official journal of the Society of Magnetic Resonance in Medicine / Society of Magnetic Resonance in Medicine 1992;24(2):375-383.

34. Benzi M. Preconditioning techniques for large linear systems: A survey. J Comput Phys 2002;182(2):418-477.

35. Byrd RH, Lu PH, Nocedal J, Zhu CY. A Limited Memory Algorithm for Bound Constrained Optimization. Siam J Sci Comput 1995;16(5):1190-1208.

36. Liu DC, Nocedal J. On the Limited Memory Bfgs Method for Large-Scale Optimization. Math Program 1989;45(3):503-528.

37. Hansen PC. Analysis of Discrete Ill-Posed Problems by Means of the L-Curve. Siam Rev 1992;34(4):561-580.

38. Leenders KL, Perani D, Lammertsma AA, Heather JD, Buckingham P, Healy MJ, Gibbs JM, Wise RJ, Hatazawa J, Herold S, et al. Cerebral blood flow, blood volume and oxygen utilization. Normal values and effect of age. Brain : a journal of neurology 1990;113 (Pt 1):27-47.

39. Grubb RL, Jr., Raichle ME, Eichling JO, Ter-Pogossian MM. The effects of changes in PaCO2 on cerebral blood volume, blood flow, and vascular mean transit time. Stroke; a journal of cerebral circulation 1974;5(5):630-639.

40. Ito H, Ibaraki M, Kanno I, Fukuda H, Miura S. Changes in the arterial fraction of human cerebral blood volume during hypercapnia and hypocapnia measured by positron emission tomography. Journal of cerebral blood flow and metabolism : official journal of the International Society of Cerebral Blood Flow and Metabolism 2005;25(7):852-857.

41. Lee SP, Duong TQ, Yang G, Iadecola C, Kim SG. Relative changes of cerebral arterial and venous blood volumes during increased cerebral blood flow: implications for BOLD fMRI. Magnetic resonance in medicine : official journal of the Society of Magnetic Resonance in Medicine / Society of Magnetic Resonance in Medicine 2001;45(5):791-800.

42. Wang Y. Quantitative Susceptibility Mapping: Magnetic Resonance Imaging of Tissue Magnetism. www.createspace.com/4346993June 2013.

43. Wang Y, Liu T. Quantitative susceptibility mapping (QSM): Decoding MRI data for a tissue magnetic biomarker. Magnetic resonance in medicine : official journal of the Society of Magnetic Resonance in Medicine / Society of Magnetic Resonance in Medicine 2014.

44. Xu B, Liu T, Spincemaille P, Prince M, Wang Y. Flow compensated quantitative susceptibility mapping for venous oxygenation imaging. Magnetic resonance in medicine : official journal of the Society of Magnetic Resonance in Medicine / Society of Magnetic Resonance in Medicine 2014;72(2):438-445.

45. Cusack R, Papadakis N. New robust 3-D phase unwrapping algorithms: application to magnetic field mapping and undistorting echoplanar images. NeuroImage 2002;16(3 Pt 1):754-764.

46. Liu T, Khalidov I, de Rochefort L, Spincemaille P, Liu J, Tsiouris AJ, Wang Y. A novel background field removal method for MRI using projection onto dipole fields (PDF). NMR in biomedicine 2011;24(9):1129-1136.

47. Liu T, Liu J, de Rochefort L, Spincemaille P, Khalidov I, Ledoux JR, Wang Y. Morphology enabled dipole inversion (MEDI) from a single-angle acquisition: comparison with COSMOS in human brain imaging. Magnetic resonance in medicine : official journal of the Society of Magnetic Resonance in Medicine / Society of Magnetic Resonance in Medicine 2011;66(3):777-783.

48. Jenkinson M, Bannister P, Brady M, Smith S. Improved optimization for the robust and accurate linear registration and motion correction of brain images. NeuroImage 2002;17(2):825-841.

49. Jenkinson M, Smith S. A global optimisation method for robust affine registration of brain images. Med Image Anal 2001;5(2):143-156.

50. Murphy BW, Carson PL, Ellis JH, Zhang YT, Hyde RJ, Chenevert TL. Signal-to-noise measures for magnetic resonance imagers. Magnetic resonance imaging 1993;11(3):425-428.

51. Zhang Y, Brady M, Smith S. Segmentation of brain MR images through a hidden Markov random field model and the expectation-maximization algorithm. IEEE transactions on medical imaging 2001;20(1):45-57.

52. Perthen JE, Lansing AE, Liau J, Liu TT, Buxton RB. Caffeine-induced uncoupling of cerebral blood flow and oxygen metabolism: a calibrated BOLD fMRI study. NeuroImage 2008;40(1):237-247.

53. Hoge RD. Calibrated FMRI. NeuroImage 2012;62(2):930-937.

54. Shu CY, Herman P, Coman D, Sanganahalli BG, Wang H, Juchem C, Rothman DL, de Graaf RA, Hyder F. Brain region and activity-dependent properties of M for calibrated fMRI. NeuroImage 2016;125:848-856.

55. Jain V, Langham MC, Wehrli FW. MRI estimation of global brain oxygen consumption rate. Journal of cerebral blood flow and metabolism : official journal of the International Society of Cerebral Blood Flow and Metabolism 2010;30(9):1598-1607.

56. Barhoum S, Rodgers ZB, Langham M, Magland JF, Li C, Wehrli FW. Comparison of MRI methods for measuring whole-brain venous oxygen saturation. Magnetic resonance in medicine : official journal of the Society of Magnetic Resonance in Medicine / Society of Magnetic Resonance in Medicine 2015;73(6):2122-2128.

57. Xu F, Liu P, Pascual JM, Xiao G, Lu H. Effect of hypoxia and hyperoxia on cerebral blood flow, blood oxygenation, and oxidative metabolism. Journal of cerebral blood flow and metabolism : official journal of the International Society of Cerebral Blood Flow and Metabolism 2012;32(10):1909-1918.

58. Chen JJ, Pike GB. Global cerebral oxidative metabolism during hypercapnia and hypocapnia in humans: implications for BOLD fMRI. Journal of cerebral blood flow and metabolism : official journal of the International Society of Cerebral Blood Flow and Metabolism 2010;30(6):1094-1099.

59. Rodgers ZB, Jain V, Englund EK, Langham MC, Wehrli FW. High temporal resolution MRI quantification of global cerebral metabolic rate of oxygen consumption in response to apneic challenge. Journal of cerebral blood flow and metabolism : official journal of the International Society of Cerebral Blood Flow and Metabolism 2013;33(10):1514-1522.

60. Barhoum S, Langham MC, Magland JF, Rodgers ZB, Li C, Rajapakse CS, Wehrli FW. Method for rapid MRI quantification of global cerebral metabolic rate of oxygen. Journal of cerebral blood flow and metabolism : official journal of the International Society of Cerebral Blood Flow and Metabolism 2015.

61. Xu F, Uh J, Brier MR, Hart J, Jr., Yezhuvath US, Gu H, Yang Y, Lu H. The influence of carbon dioxide on brain activity and metabolism in conscious humans. Journal of cerebral blood flow and metabolism : official journal of the International Society of Cerebral Blood Flow and Metabolism 2011;31(1):58-67.

62. Alsop DC, Detre JA, Golay X, Gunther M, Hendrikse J, Hernandez-Garcia L, Lu H, MacIntosh BJ, Parkes LM, Smits M, van Osch MJ, Wang DJ, Wong EC, Zaharchuk G. Recommended implementation of arterial spin-labeled perfusion MRI for clinical applications: A consensus of the ISMRM perfusion study group and the European consortium for ASL in dementia. Magnetic resonance in medicine : official journal of the Society of Magnetic Resonance in Medicine / Society of Magnetic Resonance in Medicine 2015;73(1):spcone.

63. Barker JJ. Year Book of Medicine 2013. Elsevier; 2013.

64. Larsson HB, Courivaud F, Rostrup E, Hansen AE. Measurement of brain perfusion, blood volume, and blood-brain barrier permeability, using dynamic contrast-enhanced T(1)-weighted MRI at 3 tesla. Magnetic resonance in medicine : official journal of the Society of Magnetic Resonance in Medicine / Society of Magnetic Resonance in Medicine 2009;62(5):1270-1281.

65. Lu H, Golay X, Pekar JJ, Van Zijl PC. Functional magnetic resonance imaging based on changes in vascular space occupancy. Magnetic resonance in medicine : official journal of the Society of Magnetic Resonance in Medicine / Society of Magnetic Resonance in Medicine 2003;50(2):263-274.

66. Lu H, Hua J, van Zijl PC. Noninvasive functional imaging of cerebral blood volume with vascular-space-occupancy (VASO) MRI. NMR in biomedicine 2013;26(8):932-948.

67. Miao X, Gu H, Yan L, Lu H, Wang DJ, Zhou XJ, Zhuo Y, Yang Y. Detecting resting-state brain activity by spontaneous cerebral blood volume fluctuations using whole brain vascular space occupancy imaging. NeuroImage 2014;84:575-584.

68. Gu H, Lu H, Ye FQ, Stein EA, Yang Y. Noninvasive quantification of cerebral blood volume in humans during functional activation. NeuroImage 2006;30(2):377-387.

69. He X, Yablonskiy DA. Quantitative BOLD: mapping of human cerebral deoxygenated blood volume and oxygen extraction fraction: default state. Magnetic resonance in medicine : official journal of the Society of Magnetic Resonance in Medicine / Society of Magnetic Resonance in Medicine 2007;57(1):115-126.

70. Pike GB. Quantitative functional MRI: concepts, issues and future challenges. NeuroImage 2012;62(2):1234-1240.

71. Hoffman R, Jr. EJB, Silberstein LE, Heslop H, Weitz J, Anastasi J. Hematology: Basic Principles and Practice 3rd ed. Churchill Livingstone 2000:2520-2521.

72. Dickerson RE, Geis I. Hemoglobin : structure, function, evolution, and pathology. Menlo Park, Calif.: Benjamin/Cummings Pub. Co.; 1983.

73. Savicki JP, Lang G, Ikeda-Saito M. Magnetic susceptibility of oxy- and carbonmonoxyhemoglobins. Proceedings of the National Academy of Sciences of the United States of America 1984;81(17):5417-5419.

74. Cerdonio M, Morante S, Torresani D, Vitale S, DeYoung A, Noble RW. Reexamination of the evidence for paramagnetism in oxy- and carbonmonoxyhemoglobins. Proceedings of the National Academy of Sciences of the United States of America 1985;82(1):102-103.

75. Arrighin.Gp, Maestro M, Moccia R. Magnetic Properties of Polyatomic Molecules .I. Magnetic Susceptibility of H2o,Nh3, Ch4, H2o2. J Chem Phys 1968;49(2):882-&.

Chapter 6

QSM-based $CMRO_2$ Mapping Without Vaso-Challenge: a Minimal Local Variance (MLV) Approach

6.1 ABSTRACT

Purpose

The objective of this study was to demonstrate the feasibility of a cerebral metabolic rate of oxygen ($CMRO_2$) mapping method based on its Minimum Local Variance (MLV) without vascular challenge using quantitative susceptibility mapping (QSM) and cerebral blood flow (CBF).

Methods

3D multi-echo gradient echo imaging and arterial spin labeling (ASL) were performed in 11 healthy subjects to calculate QSM and CBF. MLV was used to compute whole brain $CMRO_2$ map from QSM and CBF. The MLV method was compared with a reference method using caffeine challenge. Their agreement within the cortical gray matter (CGM) was assessed on CMRO2, and also on oxygen extraction fraction (OEF) maps at both baseline and challenge states.

Results

Mean $CMRO_2$ (in μmol/100g/min) obtained in CGM using caffeine challenge and MLV were 142 ± 16.5, and 139 ± 14.8 μmol/100g/min respectively; corresponding baseline OEF were 33.0 ± 4.0%, and 31.8 ± 3.2%, respectively. MLV and caffeine challenge methods showed no statistically significant differences across subjects with small (<4%) biases in $CMRO_2$ and OEF values.

Conclusion

MLV-based $CMRO_2$ mapping without vascular challenge using QSM and ASL is feasible in healthy subjects.

6.2 INTRODUCTION

Oxygen is critical for aerobic energy metabolism in cerebral tissue to sustain normal neural function. Non-invasively and quantitatively mapping cerebral metabolic rate of oxygen ($CMRO_2$) can provide valuable information on tissue viability and activity in both research and clinical settings (1). $CMRO_2$ is the product of cerebral blood flow (CBF) and oxygen extraction fraction (OEF). CBF can be mapped using arterial spin labeling (ASL), but OEF requires determination of deoxyheme (dH) in the draining veins/venules for each voxel of tissue. Several MRI techniques have been proposed to map dH: 1) Quantitative imaging of extraction of oxygen and tissue consumption (QUIXOTIC), which uses a velocity-selective spin labeling to selectively map venous blood T2 and oxygenation (2). 2) Calibrated fMRI, which models the magnitude $R2^*$ decay of the blood oxygen level dependent (BOLD) signal as a complex function of dH concentration ([dH]), typically estimating [dH] from signal measurements at two vascular challenges such as hyperoxia and hypercapnia to obtain $CMRO_2$ (3-5). 3) quantitative BOLD, which uses a specific venous geometry of randomly oriented tubes to model [dH] dependence of signal generated in asymmetric spin echo (6,7) or 3D multi-echo gradient echo data (8). One limitation of these approaches is that only the signal magnitude is utilized for estimating [dH].

Signal phase can be utilized through quantitative susceptibility mapping (QSM) processing to generate tissue magnetic susceptibility (9,10). Unlike R2 and R2*, the relationship between [dH] and tissue susceptibility is linear in its concentration and independent of imaging parameters (11-13). Hence, QSM can be used to quantify

oxygenation in large veins (14-18) and in tissue (19,20). [dH] in tissue can be determined from QSM by compensating for contribution from non-heme iron such as those stored in ferritin. A single vascular challenge to modify blood flow, either vasoconstrictive or vasodilative, has been used to separate the susceptibility contribution from blood and non-blood tissue (19,20). However, even the requirement of a single challenge may limit its practical utility.

In this study, a new algorithm called the minimal local variance (MLV) is proposed to obtain $CMRO_2$ maps without blood flow challenge. MLV assumes the constant $CMRO_2$ and non-blood tissue susceptibility (χ_{nb}) within each tissue type (gray and white matter) across small regions of the brain. This allows overcoming the ill-posedness of the optimization problem. The results in healthy subjects are compared to those obtained using a caffeine-challenge.

6.3 OVERCOMING ILL-POSED INVERSION USING MLV

6.3.1 $CMRO_2$ and OEF Reconstruction

According to mass conservation of oxygen molecules, the cerebral metabolic rate of oxygen $CMRO_2$ ($\mu mol/100g/min$) can be expressed as

$$\mathrm{CMRO_2} = \mathrm{CBF} \cdot ([\mathrm{dH}]_\mathrm{v} - [\mathrm{dH}]_\mathrm{a}) \quad [6.1]$$

where CBF is the cerebral blood flow ($ml/100g/min$) and $[\mathrm{dH}]_\mathrm{v}$ and $[\mathrm{dH}]_\mathrm{a}$ are the deoxyheme molar concentration ($\mu mol/ml$) in venous and arterial blood, respectively.

Oxygen Extraction Fraction (OEF) is the percentage of oxygen extracted from arterial blood and can be expressed as

$$\mathrm{OEF} = \frac{[\mathrm{dH}]_\mathrm{v} - [\mathrm{dH}]_\mathrm{a}}{[\mathrm{H}] - [\mathrm{dH}]_\mathrm{a}} \quad [6.2]$$

where $[\mathrm{H}] = 7.53\ \mu mol/ml$ is the heme molar concentration in tissue blood assuming a tissue blood hematocrit of $\mathrm{Hct_{tissue}} = 0.357$, which is estimated from an assumed hematocrit of $\mathrm{Hct}_{ss} = 0.47$ in the straight sinus and a Hct ratio of 0.759 between large vessel and brain tissue (21). $[\mathrm{dH}]_\mathrm{a} = 0.15\ \mu mol/ml$ assuming 98% arterial oxygenation (see Appendix).

$[dH]_v$ in Eq. 6.1 and 6.2, and subsequently $CMRO_2$ can be mapped using QSM (19,20).

$$\mathrm{CMRO_2} = \mathrm{CBF}\left(\frac{\chi - \chi_{nb} - \chi_0}{\mathrm{CBV_v} \cdot \mathrm{X_{dH,mol}}} - [\mathrm{dH}]_a\right) \quad [6.3]$$

Here, χ is the magnetic susceptibility mapped using QSM. χ_0 reflects the susceptibility contributions from pure oxygenated blood and arterial deoxyhemoglobin (see Appendix). $\mathrm{CBV_v}$ is the venous blood volume fraction, estimated as 77% of total CBV (22). $\mathrm{X_{dH,mol}} = 151.054$ ppb $ml/\mu mol$ is the molar magnetic susceptibility of dH (11,12).

In Eq. 6.3, $\mathrm{CMRO_2}$ and χ_{nb} are the two unknowns. In previous studies, susceptibility and blood flow of baseline and challenged brain states were mapped (19,20). Hence, $\mathrm{CMRO_2}$, χ_{nb} , and subsequently OEF can be solved. However, CBF challenges such as caffeine administration are time-consuming, presenting difficulties when performing in patients.

To solve this limitation, the QSM and CBF maps were segmented into small blocks and each block was further segmented into two tissue types (gray and white matter) using T1 weighted images. Within each block and each tissue type, χ_{nb} and $\mathrm{CMRO_2}$ are assumed to be constant. This assumes that, within a small local region, the same tissue type has similar biological and chemical makeup. Hence, $\mathrm{CMRO_2}$ and χ_{nb} of each block and tissue type can be organized into into a vector of unknowns x in a linear system format:

$$\underbrace{\begin{bmatrix} \psi_1 & 1 \\ \psi_2 & 1 \\ \vdots & \vdots \\ \psi_N & 1 \end{bmatrix}}_{A} \underbrace{\begin{bmatrix} \mathrm{CMRO_2} \\ \chi_{nb} \end{bmatrix}}_{x} = \underbrace{\begin{bmatrix} \phi_1 \\ \phi_2 \\ \vdots \\ \phi_N \end{bmatrix}}_{b}$$

Here $\psi_i = CBV_{v,i} \cdot X_{dH,mol}/CBF_i$ and $\phi_i = \chi_i - CBV_i \cdot \left(X_{ba} + X_{dH,mol} \cdot [dH]_a\right)$. The index $i = 1, \ldots, N$ denotes the i^{th} voxel of a given tissue type with a block with *N* the total number of such voxels in that block. $X_{ba} = -108.3$ ppb is the susceptibility of fully oxygenated blood (See Appendix).

In the following, this algorithm will be referred to as minimum local variance (MLV). To reduce error propagation and improve convergence speed, a right preconditioning technique is applied (23). The new system is defined as $A_P x_P = b$, where $A_P = AP$ and $x_P = P^{-1}x$. P is the preconditioner defined as $P = \mathrm{diag}\left(CMRO_{2,ub}, \mathrm{avg}(\chi)\right)$ which is designed to allow the elements of x_P to have similar order of magnitude. $CMRO_{2,ub}$ is the upper bound of $CMRO_2$ calculated within each block using Eqs.1&2 using OEF = 1. $\mathrm{avg}(\chi)$ denotes the average of susceptibility of voxels within a block that are of the same tissue type.

The solution for a given tissue type (grey or white matter) was obtained by minimizing the following cost function over the whole brain using a limited-memory Broyden–Fletcher–Goldfarb–Shanno-Bound (L-BFGS-B) algorithm (24,25) with physiological bounds on $CMRO_2$:

$$\mathbf{x} = \underset{\mathbf{x}}{\mathrm{argmin}} \left\{ \|\mathbf{Ax} - \mathbf{b}\|_2^2 + \lambda \left(CMRO_2^{\mathrm{global}} - \overline{\mathbf{CMRO_2}} \right)^2 \right\}$$

$$\text{with } \mathbf{0} \leq \mathbf{CMRO_2} \leq \mathbf{CMRO_{2,ub}} \qquad [6.4]$$

A is $\mathrm{diag}(A_P)$, a block-wise diagonal matrix with the matrix A_P for the given tissue type and for each block along the diagonal, and **x**, **b,** and $\mathbf{CMRO_2}$ are the concatenated column vectors of x_P, b, and $CMRO_2$ for that same tissue type and for each block, respectively. In the second term, $\overline{\mathbf{CMRO_2}}$ is the average $CMRO_2$ across all blocks for the given tissue type. This term imposes a global physiological constraint based on mass conservation: the global $CMRO_2$ estimated from the $CMRO_2$ map should be similar to that estimated from straight sinus. Here, $CMRO_2^{global}$ is estimated from Eq. 6.3. Global cerebral blood flow was estimated by averaging CBF over all brain voxels. The magnetic susceptibility of venous blood in the straight sinus (SS) was measured in ROIs drawn by a neuroradiologist with 10 years' experience (A.G.) and taking $CBV = CBV_v = 100\%$, $\chi_{nb} = 0$ and $Hct_{ss} = 0.47$ since only venous blood was present in these ROIs. λ is the regularization weighting parameter on the global constraint, chosen based on the average value obtained by L-curve analysis in three randomly selected subjects (26).

Whole brain grey matter (GM), white matter (WM), and CSF masks were created using the FSL FAST algorithm (27) on the inversion prepared SPGR T1w images. These masks were further divided into 6 x 6 x 6 mm^3 isotropic blocks. This block based computation was performed for the GM and WM separately, selecting within each block only those pixels that belong to the corresponding tissue type. This allowed a proper convergence when solving Eq. 6.5.To minimize potential bias due to specific block grids, blocks were shifted in (3D) diagonal directions 4 times with a step size of 1.5 mm. The data were reprocessed and the results were averaged to obtain the final images.

$CMRO_2$, OEF, and χ_{nb} were also solved using the method described in Zhang et. al., 2016 (20). Briefly, assuming χ_{nb} remained the same before and after challenge, susceptibility and CBF measurements of each voxel in baseline and challenged states were paired to solve OEF and χ_{nb} for every voxels using LBFGS-B solver with identical OEF/$CMRO_2$ bounds and global $CMRO_2$ constraint as the proposed method. The percentage change of $CMRO_2$ between the two states were estimated in the straight sinus and incorporated into the minimization.

For this feasibility study, CBV was estimated from CBF based on a linear regression derived from CBF and CBV measurements in gray and white matter using ^{15}O Positron Emission Tomography (PET) in healthy subjects (n=34) (28): $\mathrm{CBV} = (0.0723\,\mathrm{CBF} + 1.144)/100$. Post caffeine CBV was estimated from baseline CBV using the Grubb's exponent of 0.38 (29) because the empirical CBF and CBV relationship derived from PET data was from healthy subjects without vaso-challenges and may not be suitable for estimating post caffeine CBV. CBV changes after challenge were assumed to be on arterial side as suggested in the literature (30).

6.4 EXPERIMENTS AND ANALYSIS

6.4.1 Data Acquisition

The study was approved by the local Institutional Review Board. Healthy volunteers were recruited (n=11, 1 female, mean age 34 ± 12 years) for brain MRI on a 3T scanner (HDxt, GE Healthcare) using an 8-channel brain receive coil. All subjects were instructed to avoid caffeine or alcohol intake 24 hours prior to MRI.

MRI was performed before and 25 min after the oral administration of 200 mg caffeine. The protocol consisted of a 3D fast spin echo (FSE) arterial spin labeling (ASL) sequence, a 3D multi-echo spoiled gradient echo (SPGR) sequence, and an inversion prepared T1w SPGR sequence (BRAVO).

The 3D FSE ASL sequence parameters were: 20 cm FOV, 3 mm isotropic resolution, 1500 ms labeling period, 1525 ms post-label delay, 62.5 kHz readout bandwidth, spiral sampling of 8 interleaves with 512 readout points per leaf, 35 axial slices, 10.5 ms TE, 4796 ms TR, 3 signal averages, and 6 min scan time.

The 3D SPGR sequence parameters included: 0.52 mm in-plane resolution, 2 mm slice thickness, identical volume coverage as the 3D FSE ASL sequence, 7 equally spaced echoes, TE1 = 4.3 ms, echo spacing 7.9 ms, TR 56.6 ms, 62.5 kHz readout bandwidth, 15^{o} flip angle, and 7 min scan time. The pulse sequence was flow-compensated in all three directions (18).

The inversion prepared SPGR T1w sequence parameters were: 1.2 mm isotropic resolution, identical volume coverage as the 3D FSE ASL sequence, TE 2.92 ms, TR 7.68 ms, prep time 450 ms, ±19.5 kHz readout bandwidth, 15^{o} flip angle, and 2 min scan time.

6.4.2 CBF and QSM Reconstruction

CBF maps (ml/100g/min) were generated from the ASL data using the FuncTool software package (GE Healthcare, Waukesha, WI, USA). For QSM reconstruction, an adaptive quadratic-fit of the GRE phase (18) followed by a projection onto dipole fields (31) was used to obtain the local field map. Susceptibility was computed from the local field map using the Morphology Enabled Dipole Inversion (MEDI) algorithm (32-34). Susceptibility values were referenced to the susceptibility of water, as estimated in the cerebrospinal fluid (CSF) masks (see below). All images were co-registered and interpolated to the resolution of the QSM maps using the FSL FLIRT algorithm (35,36).

6.4.3 Statistical Analysis

Cortical grey matter (CGM) was segmented into the bilateral anterior (ACA), middle (MCA) and posterior cerebral artery (PCA) vascular territories (VT) by the same neuroradiologist (A.G.). For each ROI, the mean and standard deviation of $CMRO_2$ and OEF values were measured. Bland-Altman plots and paired sample t-tests were performed

to compare $CMRO_2$ and OEF values in the VTs using previous and proposed methods. P values lower than 0.05 were considered to indicate statistical significance. All data were expressed as mean ± standard deviation.

6.4.4 Numerical Simulation

Numerical simulation was performed to investigate $CMRO_2$ estimation error caused by 1) CBF error, 2) partial volume effect, and 3) QSM error. One block with matrix size of 8×8×5, the same block size in this study, was constructed. The upper and lower half was set to be white (WM) and gray matter (GM), respectively. Inputs were $CMRO_2$, χ_{nb}, and CBF (ground truth): $CMRO_2$ of GM: 181, $CMRO_2$ of WM: 138 (μmol/100g/min), χ_{nb} of GM: 0.02, χ_{nb} of WM: 0.45 WM (ppb). CBF values are given voxel-wise with normally randomized values, 49.5 ± 4.3 for WM and 64.8 ± 3.6 for GM (ml/100g/min). These values were the average values in a subject and, for the CBF standard deviation, the whole GM and WM standard deviation was calculated and divided by five to obtain a reasonable estimation for the same tissue type in small brain region. The QSM was subsequently estimated voxel-wise with the given $CMRO_2$, χ_{nb}, and CBF values. 1) To investigate the CBF error propagation in $CMRO_2$ map, we considered two cases; 1-1) low SNR CBF and 1-2) biased CBF. For low SNR case, noise was added to CBF (SNR: 4.5), and MLV was performed subsequently. This was repeated 100 times to obtain average and standard deviation. CBF SNR was estimated the ratio of mean over standard deviation in the caudate nucleus, 4.5±1.7 (n=5). 2) To investigate the partial volume effect within individual voxels,

the QSM and CBF value at the GM boundary layer was averaged with an immediate neighboring WM QSM and CBF value, respectively. This means that GM boundary voxel actually consisted of half GM and the other half WM, but was treated as GM. 3) To estimate QSM error propagation into $CMRO_2$ estimation, noise was added to QSM (SNR 3.1, estimated in the same way as CBF SNR). This was repeated 100 to obtain average and standard deviation. For all cases, global $CMRO_2$ constraint weighting (λ) was set to be 500 as used in this study.

6.5 RESULTS

Figure 6.1 shows the averaged L-curves of the three randomly selected subjects using MLV method. λ (Eq. 6.4) was chosen to be 500. In CGM, CBF decreased by 16.3 ± 7.0 ml/100g/min ($p<0.01$) after the caffeine challenge. $CMRO_2$ in CGM was 142 ± 16.5, and 139 ± 14.8 μmol/100g/min for the caffeine challenge based method and the MLV based method, respectively. These corresponded to OEF_{base} of 33.0 ± 4.0%, and 31.8 ± 3.2%, and to OEF_{chal} of 39.0 ± 4.9%, and 39.3 ± 4.1%, respectively. VT and WM ROI measurements of $CMRO_2$ and OEF are listed in Table 6.1.

Figure 6.2 shows $CMRO_2$ maps reconstructed using the caffeine challenge based and the MLV based methods across the brain in one healthy volunteer, next to the corresponding inversion prepared SPGR T1w images for anatomical reference. $CMRO_2$ maps show good consistency and the gray-white matter contrasts are in reasonable agreement with anatomical images.

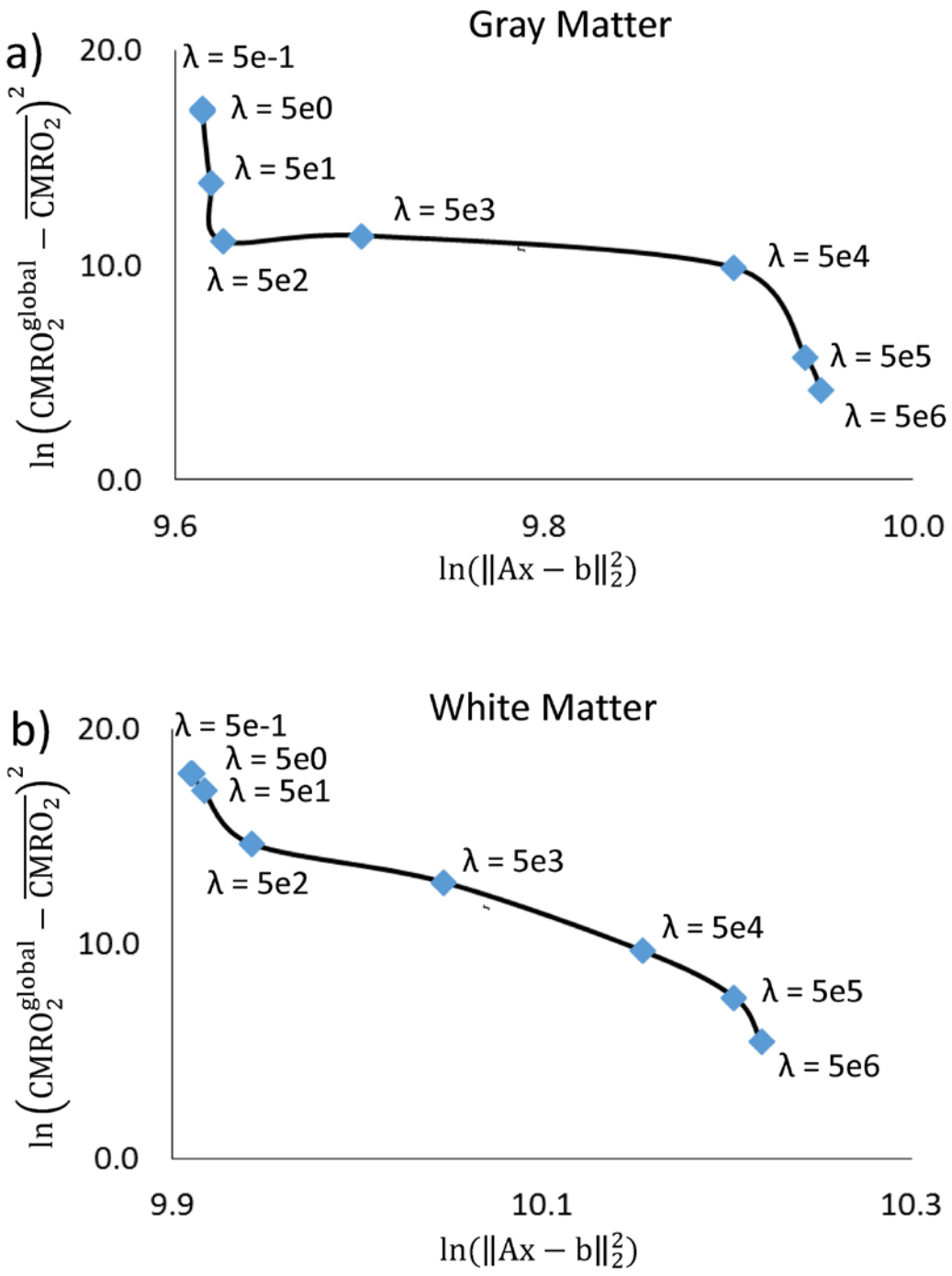

Figure 6.1. The figure shows the averaged L-curves of the three randomly selected subjects using MLV method. λ (Eq. 6.4) was chosen to be 500.

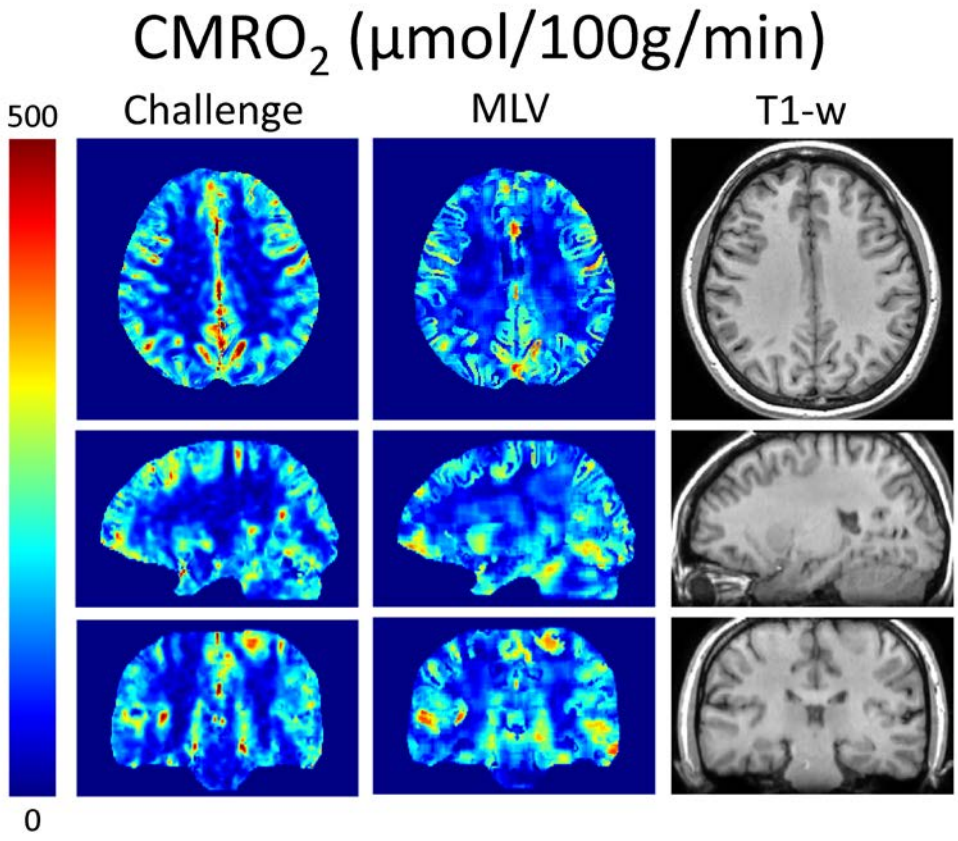

Figure 6.2. An example of 3D $CMRO_2$ map in axial, sagittal and coronal section from a healthy subject using caffeine challenge and MLV methods. The corresponding inversion prepared SPGR T1w images are shown on the right. $CMRO_2$ maps of both methods show good consistency and have good gray-white matter contrast in agreement with the inversion prepared SPGR T1w images.

Figure 6.3 shows OEF_{base}, OEF_{chal}, and baseline $CMRO_2$ maps of a second subject reconstructed with the caffeine challenge and MLV methods. OEF maps also demonstrate good consistency between the different reconstruction methods. A global increase in OEF coinciding with the caffeine-induced global CBF decrease can be readily appreciated.

Figure 6.4 shows the Bland-Altman plots comparing $CMRO_2$ and OEF values in VT between the caffeine challenge based and the MLV based method. These comparisons show <4% difference of the average of the two measurements without statistical significance ($p>0.05$).

Numerical simulation showed that $CMRO_2$ estimation error was affected by low SNR CBF and by biased CBF. In the case of low SNR CBF (SNR 4.5), $CMRO_2$ error was 6.0% for GM and 4.4% for WM. In the case of biased CBF (10% underestimation), relative $CMRO_2$ error for both GM and WM was 10%. In terms of the partial volume effect at the GM boundary, the relative $CMRO_2$ difference was 3.0 % for GM and 2.2×10^{-5} % for WM. In case of the QSM noise propagation into $CMRO_2$ (SNR 3.1), the resultant $CMRO_2$ error was 0.1 % for WM 1.5 % for GM.

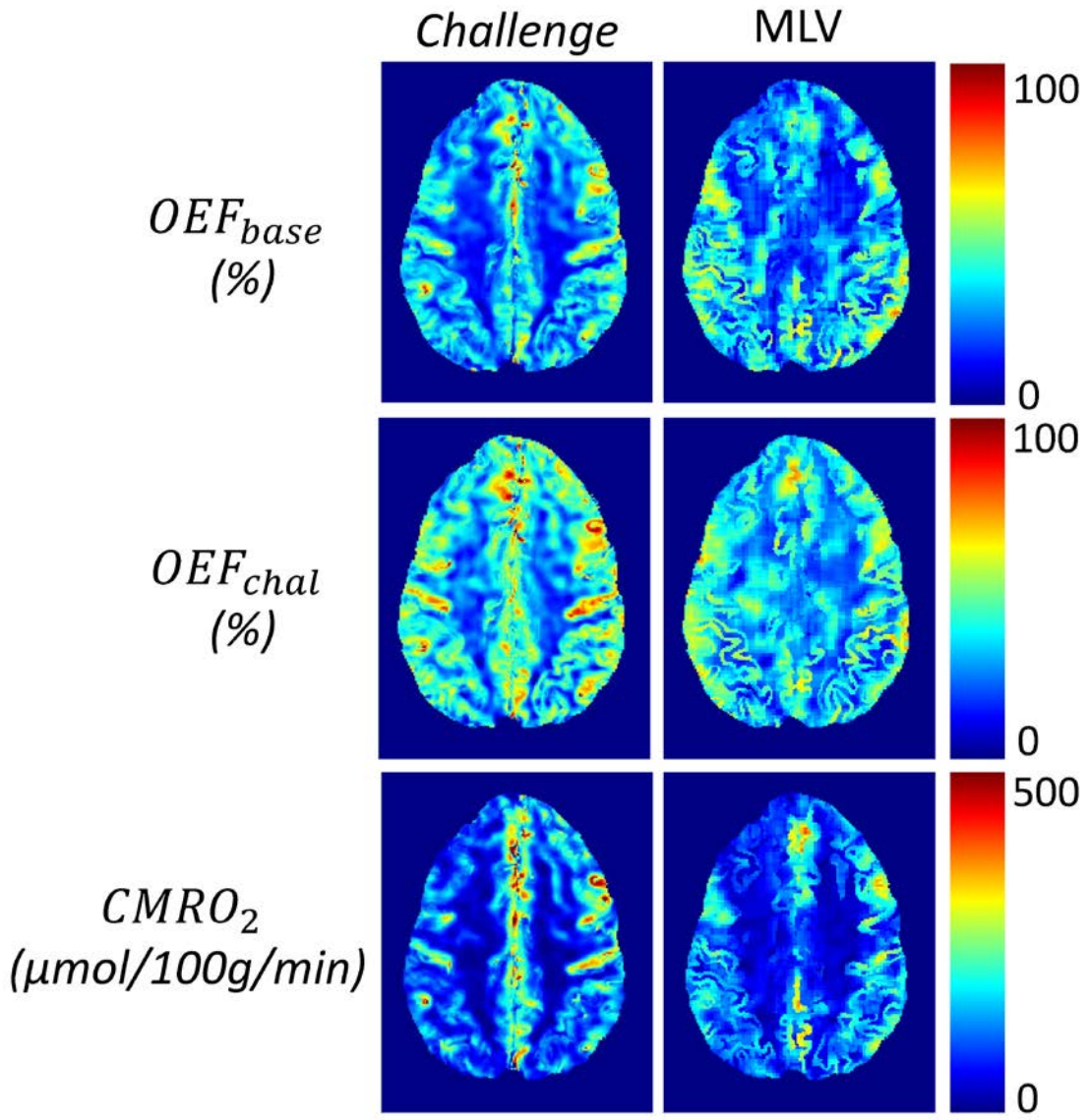

Figure 6.3. An example of OEF and $CMRO_2$ maps in a second subject reconstructed using the challenge based (left) and MLV based (right) method.

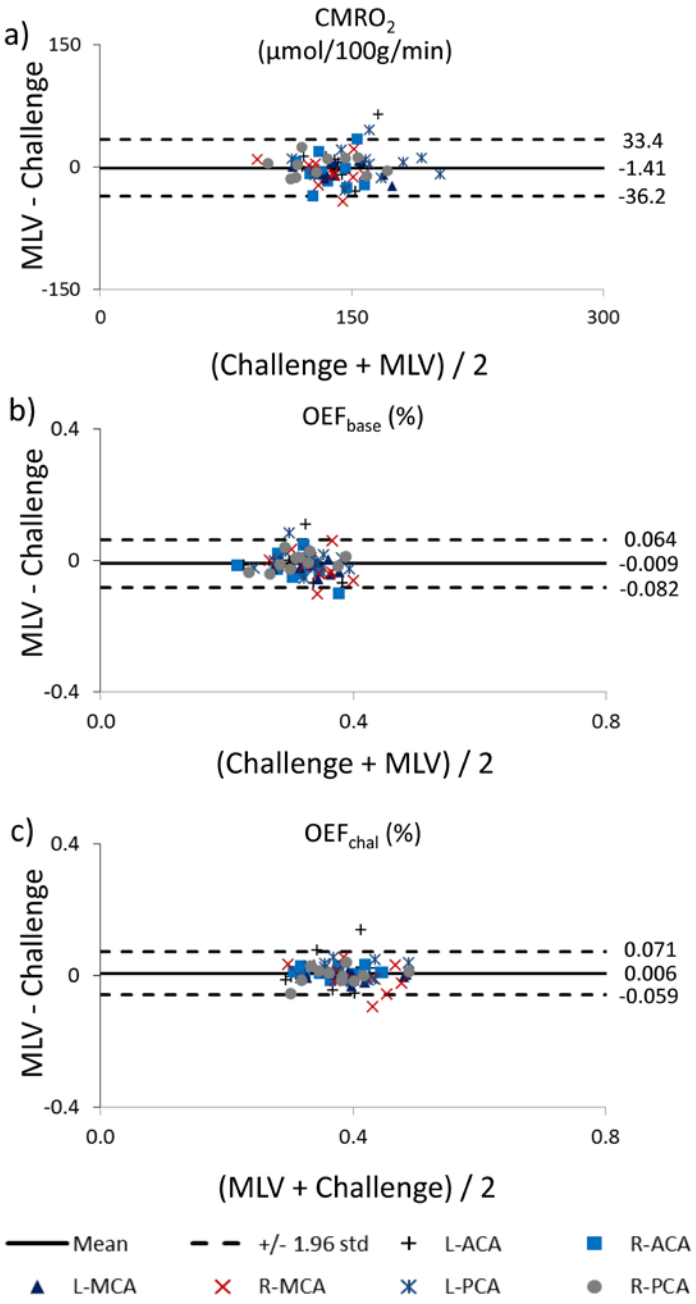

Figure 6.4. Bland-Altman plots comparing $CMRO_2$ and OEF maps reconstructed using the challenge based and the MLV based method. Small bias (<4% of the average of the two measurements) are detected in all comparisons without statistical significance ($p>0.05$).

Table 6.1. $CMRO_2$ (μmol/100g/min) and OEF (%) pre and post challenge measurements within VT and WM ROIs reconstructed using challenge and MLV methods across subjects (mean ± std).

	$CMRO_2$		OEF_{base}		OEF_{chal}	
	Challenge	MLV	Challenge	MLV	Challenge	MLV
ACA	138.7 ± 15.4	137.1 ± 18.7	31.4 ± 5.0	30.3 ± 4.1	36.5 ± 4.9	37.8 ± 5.5
MCA	142.5 ± 20.4	136.9 ± 17.3	34.1 ± 4.4	32.4 ± 3.4	40.7 ± 5.7	40.2 ± 4.6
PCA	144.7 ± 28.3	147.5 ± 28.7	31.6 ± 4.5	31.8 ± 4.8	37.4 ± 5.0	38.5 ± 5.6
WM	107.3 ± 16.5	106.2 ± 13.5	31.3 ± 4.1	31.6 ± 3.8	36.5 ± 5.6	35.0 ± 4.2

6.6 DISCUSSION

Our preliminary results demonstrate the feasibility of a noninvasive $CMRO_2$ mapping without a vascular challenge based on QSM and CBF using MLV. The $CMRO_2$ measurements agrees well between the challenge and MLV methods in healthy subjects. The elimination of the vascular challenge greatly reduces the complexity of the scanning protocol, the overall exam time and the potential risks associated with the administration of agents that modify blood flow.

Previously reported R_2*-based $CMRO_2$ mapping (3-5) methods are limited by R2* modeling for [dH]. Calibration of the model parameter is required, which may vary with scanning parameters such as field strength. Consequently, measurements at three brain states (normoxia, hypercapnia, and hyperoxia) are needed for quantitative $CMRO_2$ mapping. However, it is very cumbersome to administer stimulants to the brain to generate three distinct states. Magnetic susceptibility has a completely defined linear relation with [dH], eliminating the R2* model parameter calibration and reducing the number of required brain states for $CMRO_2$ mapping to two. The two brain states are needed to separate the susceptibility contribution from blood and non-blood tissue and can be achieved using vascular challenges, such as by administering caffeine (19) or using hyperventilation (20). However, even administering a single challenge can be cumbersome in practice. Using MLV quantitative $CMRO_2$ map can be obtained without such a challenge, making $CMRO_2$ more feasible to perform in practice.

The MLV implemented in this study used an isotropic block size of 6x6x6mm^3 such that multiple CBF voxels, acquired at a 3x3x3mm^3 isotropic resolution, were available within each block. In 1909, Brodmann divided the human cerebral cortex into 44 areas according to its cytoarchitecture (37), which were later shown to be related to various neural functions (38,39). In this study, the cerebral cortex was divided into more than 4000 regions. Hence, the assumptions of constant $CMRO_2$ and χ_{nb} within the same block and tissue type may be considered as reasonable. This MLV implementation then resulted in multiple data points to uniquely estimate the two unknowns $CMRO_2$ and χ_{nb} within each block. There is substantial amount of noise propagation from the CBF and QSM input to the $CMRO_2$ output, which can be further reduced using a global $CMRO_2$ constraint as the regularization in Eq. 6.4.

There are several limitations in this study. In MLV, χ_{nb} and $CMRO_2$ are assumed to be constant within each block and each tissue type. Therefore, MLV derived $CMRO_2$ values are block-wise constant and depend on accurate tissue segmentations. MLV may be further improved by considering physiologically relevant brain parcellations. The rationale for choosing 6×6×6 mm^3 isotropic blocks was that, for this data set, each block contained exactly 2×2×2 CBF and 12×12×3 QSM, both deemed large enough to avoid ill-posedness but not too large to avoid violating the homogeneous tissue assumptions. The block size was chosen to balance between these competing demands. To investigate the effect of block size, we applied different block-sizes (2×2×2 mm^{3}and 9×9×9 mm^3) for one subject. $CMRO_2$ values for cortical GM were 119.0±107.5, 123.5±83.2, and 124.8±64.2

μmol/100g/min for 2mm, 6mm, and 9mm block size respectively. As the block size increases, the standard deviation of $CMRO_2$ decreases. Averaging over several sub-block shifts, as done in this work, suppresses the resulting piecewise constant appearance. Nevertheless, sharp transitions remain between different tissue zones (Fig. 6.2), since computations are performed for each tissue type separately. Tissue segmentation can be challenging in patients, which might cause error. Further investigation regarding the other potential complexities in patients, e.g. difficulties in capturing regional variation within a lesion, also needs to be investigated. Another MLV limitation is the possibility that highly deoxygenated vein contribution might be smoothed out with using block based method. If some voxels in the same tissue type have strong contribution from highly deoxygenated vein, it's possible that this effect is smoothed out by the other voxels with low vein contribution. One possible way to avoid this issue would be to remove the highly deoxygenated large veins from gray and white matter mask in the implementation of MLV. The lack of Hct measurement is another limitation. We assumed $Hct_{ss} = 0.47$. We have quantified the maximum $CMRO_2$ estimation error caused by inter-subject variability by repeating calculations for both the lower (0.38) and upper bound (0.52) of the expected human Hct range. For the cortical GM, the maximum $CMRO_2$ difference between Hct = 0.47 and the two bound cases was 2.45±0.89 (n=11). Another limitation is that QSM-based $CMRO_2$ does require CBV measurements as in R2* based methods. Our MLV feasibility study here used CBV estimated from CBF assuming an empirical relationship derived from normative PET data (28) and assumed a 0.77 ratio between venous and total CBV, as in previous R2* and QSM studies (19,20). While both these assumptions are consistent with

the literature on healthy subjects (22,30), they may be invalid in some patients. Also, the accuracy of CBF measurement by ASL might suffer from low SNR in WM or with large veins and long arterial transit times. Our simulation showed that $CMRO_2$ estimation would be affected by low SNR CBF (4.4% error in WM with SNR 4.5) and biased CBF values (10% error in both WM and GM with 10% underestimation). This may be addressed by a direct measurement of CBV using dynamic contrast enhancement (DCE) (40) or a non-contrast MRI technique such as Vascular Space Occupancy (VASO) (41-43), multiphase ASL based CBVa (44) or quantitative BOLD (45). Another limitation of study is the use of straight sinus OEF for global $CMRO_2$ constraint. Jugular veins would more ideal to estimate the global $CMRO_2$ but are more complicated to images within the same field of view and/or coil. Moreover, QSM outside the brain remains challenging due motion and the need for additional phase preprocessing such as water-fat separation. Therefore, measurements in straight sinus are used under the assumption that straight sinus and jugular veins have similar oxygenations, given that OEF has been shown uniform in healthy subjects across the brain using ^{15}O PET. Because of the use of flow compensation during acquisition and the adaptive quadratic fitting of the field (18) flow effects on QSM are minimized. Finally, the subject in this study were young and healthy, and the validation and applicability of this technique in a general patient population remains to be investigated.

6.7 CONCLUSION

Our study demonstrated the feasibility of a noninvasive $CMRO_2$ mapping without vascular challenge based on QSM and CBF using MLV. In vivo imaging in heathy subjects demonstrates that the $CMRO_2$ and OEF maps obtained with the proposed MLV method agree well with those obtained using a blood flow challenge based method.

6.8 APPENDIX

Calculation of heme concentration ($[H]$) in tissue blood

$$[\mathrm{H}] = 4\mathrm{Hct}_{\mathrm{tissue}}\,\frac{\rho_{\mathrm{RBC,Hb}}}{\mathrm{M}_{\mathrm{Hb}}} = 7.53\ \mu\mathrm{mol/ml}$$

Where 4 account of 4 heme per Hb, $\mathrm{Hct}_{\mathrm{tissue}} = 0.357$, $\rho_{\mathrm{RBC,Hb}} = 0.34\mathrm{g/ml}$ is mass concentration of Hb in a red blood cell (46), $\mathrm{M}_{\mathrm{Hb}} = 64450 \times 10^{-6}\ \mathrm{g/\mu mol}$ is the the molar mass of dHb (47).

Calculation of χ_o

$$\chi_{\mathrm{o}} = \mathrm{CBV} \cdot \mathrm{X}_{\mathrm{ba}} + \mathrm{CBV}_{\mathrm{a}} \cdot \mathrm{X}_{\mathrm{dH,mol}} \cdot [\mathrm{dH}]_{\mathrm{a}}$$

Here $\mathrm{CBV}_{\mathrm{a}} = \mathrm{CBV} - \mathrm{CBV}_{\mathrm{v}} = 0.23\mathrm{CBV}$ is the arterial blood volume fraction. $[\mathrm{dH}]_{\mathrm{a}} = 0.15\ \mu\mathrm{mol/ml}$ is $[dH]$ in arterial blood assuming 98% oxygenation. X_{ba} is susceptibility of 100% oxygenated blood.

$$\mathrm{X}_{\mathrm{ba}} = \mathrm{Hct}_{\mathrm{tissue}}\delta_{\mathrm{Hb}} \cdot \mathrm{X}_{\mathrm{oHb}} + (1 - \mathrm{Hct}_{\mathrm{tissue}}\delta_{\mathrm{Hb}})\mathrm{X}_{\mathrm{p}} = -108.3\ \mathrm{ppb}$$

Where δ_{Hb} is volume fraction of Hb in RBC.

$$\delta_{\mathrm{Hb}} = \frac{\rho_{\mathrm{RBC,Hb}}}{\rho_{\mathrm{Hb}}} = 0.255$$

Here $\rho_{\mathrm{RBC,Hb}} = 0.34\mathrm{g/ml}$ is Hb mass concentration in a red blood cell (46). $\rho_{\mathrm{Hb}} = 1.335\ \mathrm{g/ml}$ is Hb density in pure aggregate (48).

$\mathrm{X}_{\mathrm{oHb}}$ is volume susceptibility of oxyhemoglobin (OHb).

$$X_{oHb} = -4\pi\rho_{Hb}(0.587 \times 10^{-6}\ \mathrm{ml/g}) - (-9035\ \mathrm{ppb}) = -813\mathrm{ppb}$$

Here 0.587×10^{-6} ml/g is mass susceptibility of globin relative to vacuum in CGS unit (48,49). 4π is for unit conversion from cgs to si units. -9035 ppb is water volume susceptibility relative to vacuum (50).

$X_p = -37.7$ ppb are the oxyhemoglobin and blood plasma volume susceptibility (12).

REFERENCES

1. Gupta A, Baradaran H, Schweitzer AD, Kamel H, Pandya A, Delgado D, Wright D, Hurtado-Rua S, Wang Y, Sanelli PC. Oxygen extraction fraction and stroke risk in patients with carotid stenosis or occlusion: a systematic review and meta-analysis. AJNR American journal of neuroradiology 2014;35(2):250-255.

2. Bolar DS, Rosen BR, Sorensen AG, Adalsteinsson E. QUantitative Imaging of eXtraction of oxygen and TIssue consumption (QUIXOTIC) using venular-targeted velocity-selective spin labeling. Magnetic resonance in medicine : official journal of the Society of Magnetic Resonance in Medicine / Society of Magnetic Resonance in Medicine 2011;66(6):1550-1562.

3. Bulte DP, Kelly M, Germuska M, Xie J, Chappell MA, Okell TW, Bright MG, Jezzard P. Quantitative measurement of cerebral physiology using respiratory-calibrated MRI. NeuroImage 2012;60(1):582-591.

4. Gauthier CJ, Hoge RD. Magnetic resonance imaging of resting OEF and CMRO(2) using a generalized calibration model for hypercapnia and hyperoxia. NeuroImage 2012;60(2):1212-1225.

5. Wise RG, Harris AD, Stone AJ, Murphy K. Measurement of OEF and absolute CMRO2: MRI-based methods using interleaved and combined hypercapnia and hyperoxia. NeuroImage 2013;83:135-147.

6. An H, Lin W. Impact of intravascular signal on quantitative measures of cerebral oxygen extraction and blood volume under normo- and hypercapnic conditions using an asymmetric spin echo approach. Magnetic resonance in medicine : official journal of the Society of Magnetic Resonance in Medicine / Society of Magnetic Resonance in Medicine 2003;50(4):708-716.

7. An H, Ford AL, Chen Y, Zhu H, Ponisio R, Kumar G, Shanechi AM, Khoury N, Vo KD, Williams J, Derdeyn CP, Diringer MN, Panagos P, Powers WJ, Lee JM, Lin W. Defining the ischemic penumbra using magnetic resonance oxygen metabolic index. Stroke; a journal of cerebral circulation 2015;46(4):982-988.

8. Ulrich X, Yablonskiy DA. Separation of cellular and BOLD contributions to T2* signal relaxation. Magnetic resonance in medicine 2015:doi: 10.1002/mrm.25610.

9. de Rochefort L, Liu T, Kressler B, Liu J, Spincemaille P, Lebon V, Wu J, Wang Y. Quantitative susceptibility map reconstruction from MR phase data using bayesian regularization: validation and application to brain imaging. Magnetic resonance in medicine : official journal of the Society of Magnetic Resonance in Medicine / Society of Magnetic Resonance in Medicine 2010;63(1):194-206.

10. Wang Y, Liu T. Quantitative susceptibility mapping (QSM) Decoding MRI data for a tissue magnetic biomarker, Magnetic Resonance in Medicine Volume 73, Issue 1. Magn Reson Med 2015;73(1):82-101.

11. Jain V, Abdulmalik O, Propert KJ, Wehrli FW. Investigating the magnetic susceptibility properties of fresh human blood for noninvasive oxygen saturation quantification. Magnetic resonance in medicine 2012;68(3):863-867.

12. Spees WM, Yablonskiy DA, Oswood MC, Ackerman JJ. Water proton MR properties of human blood at 1.5 Tesla: magnetic susceptibility, T(1), T(2), T*(2), and non-Lorentzian signal behavior. Magnetic resonance in medicine : official journal of the Society of Magnetic Resonance in Medicine / Society of Magnetic Resonance in Medicine 2001;45(4):533-542.

13. Li J, Chang S, Liu T, Wang Q, Cui D, Chen X, Jin M, Wang B, Pei M, Wisnieff C, Spincemaille P, Zhang M, Wang Y. Reducing the object orientation dependence of susceptibility effects in gradient echo MRI through quantitative susceptibility mapping. Magnetic resonance in medicine : official journal of the Society of Magnetic Resonance in Medicine / Society of Magnetic Resonance in Medicine 2012;68(5):1563-1569.

14. Haacke EM, Lai S, Reichenbach JR, Kuppusamy K, Hoogenraad FG, Takeichi H, Lin W. In vivo measurement of blood oxygen saturation using magnetic resonance imaging: a direct validation of the blood oxygen level-dependent concept in functional brain imaging. Hum Brain Mapp 1997;5(5):341-346.

15. Fan AP, Bilgic B, Gagnon L, Witzel T, Bhat H, Rosen BR, Adalsteinsson E. Quantitative oxygenation venography from MRI phase. Magnetic resonance in medicine : official journal of the Society of Magnetic Resonance in Medicine / Society of Magnetic Resonance in Medicine 2014;72(1):149-159.

16. Li C, Langham MC, Epstein CL, Magland JF, Wu J, Gee J, Wehrli FW. Accuracy of the cylinder approximation for susceptometric measurement of intravascular oxygen saturation. Magnetic resonance in medicine : official journal of the Society of Magnetic Resonance in Medicine / Society of Magnetic Resonance in Medicine 2012;67(3):808-813.

17. Wehrli FW, Rodgers ZB, Jain V, Langham MC, Li C, Licht DJ, Magland J. Time-resolved MRI oximetry for quantifying CMRO(2) and vascular reactivity. Academic radiology 2014;21(2):207-214.

18. Xu B, Liu T, Spincemaille P, Prince M, Wang Y. Flow compensated quantitative susceptibility mapping for venous oxygenation imaging. Magnetic resonance in medicine : official journal of the Society of Magnetic Resonance in Medicine / Society of Magnetic Resonance in Medicine 2014;72(2):438-445.

19. Zhang J, Liu T, Gupta A, Spincemaille P, Nguyen TD, Wang Y. Quantitative mapping of cerebral metabolic rate of oxygen (CMRO2) using quantitative susceptibility mapping (QSM). Magnetic resonance in medicine 2015;74(4):945-952.

20. Zhang J, Zhou D, Nguyen TD, Spincemaille P, Gupta A, Wang Y. Cerebral metabolic rate of oxygen (CMRO) mapping with hyperventilation challenge using quantitative susceptibility mapping (QSM). Magnetic resonance in medicine : official journal of the Society of Magnetic Resonance in Medicine / Society of Magnetic Resonance in Medicine 2016;10.1002/mrm.26253.

21. Sakai F, Nakazawa K, Tazaki Y, Ishii K, Hino H, Igarashi H, Kanda T. Regional cerebral blood volume and hematocrit measured in normal human volunteers by single-photon emission computed tomography. Journal of cerebral blood flow and metabolism : official journal of the International Society of Cerebral Blood Flow and Metabolism 1985;5(2):207-213.

22. An H, Lin W. Cerebral venous and arterial blood volumes can be estimated separately in humans using magnetic resonance imaging. Magnetic resonance in medicine : official journal of the Society of Magnetic Resonance in Medicine / Society of Magnetic Resonance in Medicine 2002;48(4):583-588.

23. Benzi M. Preconditioning techniques for large linear systems: A survey. J Comput Phys 2002;182(2):418-477.

24. Byrd RH, Lu PH, Nocedal J, Zhu CY. A Limited Memory Algorithm for Bound Constrained Optimization. Siam J Sci Comput 1995;16(5):1190-1208.

25. Liu DC, Nocedal J. On the Limited Memory Bfgs Method for Large-Scale Optimization. Math Program 1989;45(3):503-528.

26. Hansen PC. Analysis of Discrete Ill-Posed Problems by Means of the L-Curve. Siam Rev 1992;34(4):561-580.

27. Zhang Y, Brady M, Smith S. Segmentation of brain MR images through a hidden Markov random field model and the expectation-maximization algorithm. IEEE transactions on medical imaging 2001;20(1):45-57.

28. Leenders KL, Perani D, Lammertsma AA, Heather JD, Buckingham P, Healy MJ, Gibbs JM, Wise RJ, Hatazawa J, Herold S, et al. Cerebral blood flow, blood volume and oxygen utilization. Normal values and effect of age. Brain : a journal of neurology 1990;113 (Pt 1):27-47.

29. Grubb RL, Jr., Raichle ME, Eichling JO, Ter-Pogossian MM. The effects of changes in PaCO2 on cerebral blood volume, blood flow, and vascular mean transit time. Stroke; a journal of cerebral circulation 1974;5(5):630-639.

30. Ito H, Ibaraki M, Kanno I, Fukuda H, Miura S. Changes in the arterial fraction of human cerebral blood volume during hypercapnia and hypocapnia measured by positron emission tomography. Journal of cerebral blood flow and metabolism : official journal of the International Society of Cerebral Blood Flow and Metabolism 2005;25(7):852-857.

31. Liu T, Khalidov I, de Rochefort L, Spincemaille P, Liu J, Tsiouris AJ, Wang Y. A novel background field removal method for MRI using projection onto dipole fields (PDF). NMR in biomedicine 2011;24(9):1129-1136.

32. Liu J, Liu T, de Rochefort L, Ledoux J, Khalidov I, Chen W, Tsiouris AJ, Wisnieff C, Spincemaille P, Prince MR, Wang Y. Morphology enabled dipole inversion for quantitative susceptibility mapping using structural consistency between the magnitude image and the susceptibility map. NeuroImage 2012;59(3):2560-2568.

33. Liu T, Liu J, de Rochefort L, Spincemaille P, Khalidov I, Ledoux JR, Wang Y. Morphology enabled dipole inversion (MEDI) from a single-angle acquisition: comparison with COSMOS in human brain imaging. Magnetic resonance in medicine 2011;66(3):777-783.

34. Liu T, Xu W, Spincemaille P, Avestimehr AS, Wang Y. Accuracy of the morphology enabled dipole inversion (MEDI) algorithm for quantitative susceptibility mapping in MRI. IEEE transactions on medical imaging 2012;31(3):816-824.

35. Jenkinson M, Smith S. A global optimisation method for robust affine registration of brain images. Med Image Anal 2001;5(2):143-156.

36. Jenkinson M, Bannister P, Brady M, Smith S. Improved optimization for the robust and accurate linear registration and motion correction of brain images. NeuroImage 2002;17(2):825-841.

37. Brodmann K. Vergleichende Lokalisationslehre der Grosshirnrinde in ihren Prinzipien dargestellt auf Grund des Zellenbaues. Barth JA, Leipzig 1909.

38. Roland PE, Zilles K. Structural divisions and functional fields in the human cerebral cortex. Brain research Brain research reviews 1998;26(2-3):87-105.

39. Karl Zilles, Katrin Amunts. Chapter 23, The Human Nervous System (Third Edition). Mai JK, Paxinos G, editors. MA, USA: Academic Press, Elsevier; 2012.

40. Larsson HB, Courivaud F, Rostrup E, Hansen AE. Measurement of brain perfusion, blood volume, and blood-brain barrier permeability, using dynamic contrast-enhanced T(1)-weighted MRI at 3 tesla. Magnetic resonance in medicine : official journal of the Society of Magnetic Resonance in Medicine / Society of Magnetic Resonance in Medicine 2009;62(5):1270-1281.

41. Lu H, Golay X, Pekar JJ, Van Zijl PC. Functional magnetic resonance imaging based on changes in vascular space occupancy. Magnetic resonance in medicine : official journal of the Society of Magnetic Resonance in Medicine / Society of Magnetic Resonance in Medicine 2003;50(2):263-274.

42. Miao X, Gu H, Yan L, Lu H, Wang DJ, Zhou XJ, Zhuo Y, Yang Y. Detecting resting-state brain activity by spontaneous cerebral blood volume fluctuations using whole brain vascular space occupancy imaging. NeuroImage 2014;84:575-584.

43. Lu H, Hua J, van Zijl PC. Noninvasive functional imaging of cerebral blood volume with vascular-space-occupancy (VASO) MRI. NMR in biomedicine 2013;26(8):932-948.

44. Yan L, Li C, Kilroy E, Wehrli FW, Wang DJ. Quantification of arterial cerebral blood volume using multiphase-balanced SSFP-based ASL. Magnetic resonance in medicine : official journal of the Society of Magnetic Resonance in Medicine / Society of Magnetic Resonance in Medicine 2012;68(1):130-139.

45. He X, Yablonskiy DA. Quantitative BOLD: mapping of human cerebral deoxygenated blood volume and oxygen extraction fraction: default state. Magnetic resonance in medicine : official journal of the Society of Magnetic Resonance in Medicine / Society of Magnetic Resonance in Medicine 2007;57(1):115-126.

46. Hoffman R, Jr. EJB, Silberstein LE, Heslop H, Weitz J, Anastasi J. Hematology: Basic Principles and Practice 3rd ed. Churchill Livingstone 2000:2520-2521.

47. Dickerson RE, Geis I. Hemoglobin : structure, function, evolution, and pathology. Menlo Park, Calif.: Benjamin/Cummings Pub. Co.; 1983.

48. Savicki JP, Lang G, Ikeda-Saito M. Magnetic susceptibility of oxy- and carbonmonoxyhemoglobins. Proceedings of the National Academy of Sciences of the United States of America 1984;81(17):5417-5419.

49. Cerdonio M, Morante S, Torresani D, Vitale S, DeYoung A, Noble RW. Reexamination of the evidence for paramagnetism in oxy- and carbonmonoxyhemoglobins. Proceedings of the National Academy of Sciences of the United States of America 1985;82(1):102-103.

50. Arrighin.Gp, Maestro M, Moccia R. Magnetic Properties of Polyatomic Molecules .I. Magnetic Susceptibility of H2o,Nh3, Ch4, H2o2. J Chem Phys 1968;49(2):882-&.

Chapter 7

Conclusions and Recommendations

7.1 FUTURE WORK

7.1.1 Investigation of Blood Degradation in Hemorrhagic Patients Using QSM

The study suggests 1) The susceptibility of hematomas are consistently positive relative to CSF even during the hyperacute stage, challenging the traditional model that hyperacute hematomas contain mostly oxygenated arterial blood which has slightly negative susceptibility (1,2); 2) The susceptibilities of hematomas decrease substantially from the acute to subacute stage, thus furthering the MRI literature (1,13) about the late subacute stage with new insight for a quantitative model to explain the hemoglobin degradation process.

One major improvement is to perform more sophisticated in vitro blood phantom experiment. While the phantom experiment demonstrated the course of susceptibility changes of degrading blood sample in test tubes, it lacks several important physiological processes that might affect the time course and compositions of the hematoma including inflammation and hemosiderin formation. Histology and protein analysis should also be performed to correlate the susceptibility changes to blood degradation products.

Another major improvement is to address the uneven sampling density over various stages of ICH, especially for the hyperacute stage where only 4 patients were scanned. Larger hyperacute ICH patient data are warrant despite the difficulty in execution.

The third limitation of this study is its cross-sectional design. Longitudinally serial imaging is highly recommended to remove variability among different patients.

Lastly, histological evidences are recommended to correlate molecular compositions to susceptibility changes. This issue can be addressed through follow up studies of hematoma susceptibility in animal models or autopsy after patients deceased.

7.1.2 QSM-based $CMRO_2$ Mapping

In chapter 4, a new signal model based on magnetic susceptibility of blood and non-blood tissue is proposed to overcome some of the limitations of current R2 and R2* based approaches. However, the model and algorithm have several limitations, including low SNR, physiologically impossible values, and impracticality resulted from the requirement of blood flow challenges.

Chapter 5 and 6 attempted to address these limitations with some success. In chapter 5, a new algorithm is proposed to denoise QSM based $CMRO_2$ and OEF maps by incorporating prior knowledge (Bayesian approach) during image reconstruction. The prior knowledge include a right-handed preconditioner, a $CMRO_2$ global constraint derived from straight sinus, and a physiological lower and upper bounds of 0 to 100 % on OEF maps. Caffeine administration is also replaced by hyperventilation as the vaso-restrictive challenge which reduced the protocol time by 4 folds. In chapter 6, a new algorithm named minimal local variance (MLV) is proposed to remove the requirement of vaso challenges in the QSM-based $CMRO_2$ technique to further improve its clinical practicality.

One major limitation is the low SNR of $CMRO_2$ and OEF maps. With current scanning parameters and reconstruction methods, $CMRO_2$ map has a SNR of 5.78 ± 1.36, which is not ideal. To improve SNR there are several suggestions: 1) Use more advance hardware such as 7T scanner and 32 channel head coils; 2) More sophisticated algorithm with structural prior as constraints.

Another limitation is that global OEFs were estimated from the straight sinus and global CBFs were estimated by taking the sum of all voxels in CBF maps covering the whole brain. However, straight sinus mainly drains medial brain tissues and deep gray matter, not cortical tissue / whole brain. Jugular vein or superior straight sinus (SSS) are more ideal places to measure both global OEF and global CBF as suggested by Wehrli (3). To obtain more accurate global $CMRO_2$ measurement it is recommended to perform phase contrast scan on jugular vein or SSS.

Third limitation is that OEF was slightly lower (2.5%) in WM than in CGM in QSM based OEF maps. This observed discrepancy may be attributed to the lower CBF changes detected in WM than the changes in CGM after caffeine and HV challenges (-6.0±4.3ml/100g/min vs -17.9±5.53ml/100g/min, $p<0.01$). The small absolute CBF change and the known challenges of accurately quantifying CBF in WM with ASL MRI perfusion make OEFs in these regions more difficult to resolve. Our protocol was based on a routine clinical protocol used at our institution. By modifying the protocol according to the recent white paper by Alsop et al (4), SNR could potentially be improved at a cost of scan time increase.

Forth limitation is the requirement of quantitative CBV measurements. For this feasibility study, CBV was estimated from CBF using an empirical relationship derived from normative PET data and the Grubb's exponent of 0.38, which can be a source of error. This limitation may be addressed by direct measurements of CBV using technique such as dynamic study with contrast agent (5,6), or by non-contrast MRI with detailed vascular signal modeling such as Vascular Space Occupancy (VASO)(7-9), fMRI with multiple inversion times (10), or quantitative BOLD (11,12).

Fifth limitation is the lack of Hct measurements. We assumed $\mathrm{Hct}_{ss} = 0.47$ and calculated Hct_{tissue} as $0.759\mathrm{Hct}_{ss}$ as measured in (13). In hyperventilation study, we have quantified the maximum $CMRO_2$ estimation error caused by inter-subject variability of Hct_{ss} by repeating the calculations for both the lower (0.38) and upper bound (0.52) of the expected human Hct_{ss} range. For the cortical GM, the maximum difference between the $CMRO_2$ value for Hct=0.47 and the two $CMRO_2$ values obtained in this manner was 2.4 ± 1.1% (n=11). Hct can be measured through blood test with ease. Yet the ratio between Hct_{ss} and Hct_{tissue} may vary spatially and among subjects. The potential error due to such variation warrants further investigation.

There are several additional limitations in MLV approach. Firstly, the selection of block size requires further investigation. The MLV implemented in this study used an isotropic block size of $6x6x6mm^3$ such that multiple CBF voxels, acquired at a $3x3x3mm^3$ isotropic resolution, were available within each block. This MLV implementation then resulted in multiple data points to uniquely estimate the two unknowns $CMRO_2$ and χ_{nb}

within each block. This block size deemed to be large enough to avoid ill-posedness but not too large to avoid violating the homogeneous tissue assumptions. The optimal block size under different scanning resolutions and SNR need to be systematically studied.

Secondly, in MLV χ_{nb} and $CMRO_2$ are assumed to be constant within each block and each tissue type. Therefore, MLV derived $CMRO_2$ values are block-wise constant and depend on accurate tissue segmentations. MLV may be further improved by considering physiologically relevant brain parcellations. In addition, robust tissue segmentation in patients need to be used to avoid violation of these assumptions.

Thirdly, $CMRO_2$ and OEF maps reconstructed using MLV are susceptible to piece-wise appearance and partial volume effects. Averaging over several sub-block shifts, as done in this work, suppresses the resulting piecewise constant appearance. Highly deoxygenated vein contribution might be smoothed out with using block based method. If some voxels in the same tissue type have strong contribution from highly deoxygenated vein, it's possible that this effect is smoothed out by the other voxels with low vein contribution. This limitation can be mitigated by acquiring higher resolution data and reduce block sizes. Trade off with SNR however needs to be considered.

Lastly, clinical study and comparison against golden standard ^{15}O positron emission tomography is warrant to study the effectiveness of the technique.

7.2 CONCLUSION

In this dissertation, a clinical study on ICH using QSM was performed and a QSM/ ASL based technique was developed to quantitatively map $CMRO_2$ and OEFs. The clinical study is the one of the first to quantitatively characterize hematoma susceptibilities at various stages using QSM. QSM reveals positive susceptibility relative to CSF in hyperacute hematomas, indicating the existence of deoxyhemoglobin even in the hyperacute stage. QSM also reveals a significant reduction of susceptibility from acute to late subacute ICH, suggesting a decrease in methemoglobin concentration in the late subacute stage. Future studies are warrant to verify the finds with larger sample size and histological evidence.

The developed QSM-based $CMRO_2$ mapping technique overcome some of the fundamental limitations of R2 and R2* based MRI technique such as dependence on imaging parameters, and the requirement of blood flow challenges. Future studies are warrant to improve SNR, eliminate bias in WM in OEF maps, improve robustness, and validate against ^{15}O PET in larger healthy and patient populations.

REFERENCES

1. Jain V, Abdulmalik O, Propert KJ, Wehrli FW. Investigating the magnetic susceptibility properties of fresh human blood for noninvasive oxygen saturation quantification. Magn Reson Med 2012;68(3):863-867.

2. Zhang J, Liu T, Gupta A, Spincemaille P, Nguyen TD, Wang Y. Quantitative mapping of cerebral metabolic rate of oxygen (CMRO) using quantitative susceptibility mapping (QSM). Magnetic resonance in medicine : official journal of the Society of Magnetic Resonance in Medicine / Society of Magnetic Resonance in Medicine 2014.

3. Jain V, Langham MC, Wehrli FW. MRI estimation of global brain oxygen consumption rate. Journal of cerebral blood flow and metabolism : official journal of the International Society of Cerebral Blood Flow and Metabolism 2010;30(9):1598-1607.

4. Alsop DC, Detre JA, Golay X, Gunther M, Hendrikse J, Hernandez-Garcia L, Lu H, MacIntosh BJ, Parkes LM, Smits M, van Osch MJ, Wang DJ, Wong EC, Zaharchuk G. Recommended implementation of arterial spin-labeled perfusion MRI for clinical applications: A consensus of the ISMRM perfusion study group and the European consortium for ASL in dementia. Magnetic resonance in medicine : official journal of the Society of Magnetic Resonance in Medicine / Society of Magnetic Resonance in Medicine 2015;73(1):spcone.

5. Barker JJ. Year Book of Medicine 2013. Elsevier; 2013.

6. Larsson HB, Courivaud F, Rostrup E, Hansen AE. Measurement of brain perfusion, blood volume, and blood-brain barrier permeability, using dynamic contrast-enhanced T(1)-weighted MRI at 3 tesla. Magnetic resonance in medicine : official journal of the Society of Magnetic Resonance in Medicine / Society of Magnetic Resonance in Medicine 2009;62(5):1270-1281.

7. Lu H, Golay X, Pekar JJ, Van Zijl PC. Functional magnetic resonance imaging based on changes in vascular space occupancy. Magnetic resonance in medicine : official journal of the Society of Magnetic Resonance in Medicine / Society of Magnetic Resonance in Medicine 2003;50(2):263-274.

8. Lu H, Hua J, van Zijl PC. Noninvasive functional imaging of cerebral blood volume with vascular-space-occupancy (VASO) MRI. NMR in biomedicine 2013;26(8):932-948.

9. Miao X, Gu H, Yan L, Lu H, Wang DJ, Zhou XJ, Zhuo Y, Yang Y. Detecting resting-state brain activity by spontaneous cerebral blood volume fluctuations using whole brain vascular space occupancy imaging. NeuroImage 2014;84:575-584.

10. Gu H, Lu H, Ye FQ, Stein EA, Yang Y. Noninvasive quantification of cerebral blood volume in humans during functional activation. NeuroImage 2006;30(2):377-387.

11. He X, Yablonskiy DA. Quantitative BOLD: mapping of human cerebral deoxygenated blood volume and oxygen extraction fraction: default state. Magnetic resonance in medicine : official journal of the Society of Magnetic Resonance in Medicine / Society of Magnetic Resonance in Medicine 2007;57(1):115-126.

12. Pike GB. Quantitative functional MRI: concepts, issues and future challenges. NeuroImage 2012;62(2):1234-1240.

13. Sakai F, Nakazawa K, Tazaki Y, Ishii K, Hino H, Igarashi H, Kanda T. Regional cerebral blood volume and hematocrit measured in normal human volunteers by single-photon emission computed tomography. Journal of cerebral blood flow and metabolism : official journal of the International Society of Cerebral Blood Flow and Metabolism 1985;5(2):207-213.